FINITE-ELEMENT SIMULATION STUDIES FOR CONSEQUENCES OF ROCK LAYERS AND WEAK INTERFACES IN UNCONVENTIONAL RESERVOIRS

A Dissertation

by

SEOUNG HYUN RHO

Submitted to the Office of Graduate and Professional Studies of
Texas A&M University
in partial fulfillment of the requirements for the degree of

DOCTOR OF PHILOSOPHY

Chair of Committee,	Samuel Noynaert
Committee Members,	Jerome Schubert
	Kan Wu
	James Boyd
Head of Department,	Jeff A. Spath

August 2018

Major Subject: Petroleum Engineering

ABSTRACT

Unconventional reservoir systems are heterogeneous, thinly layered, and often exhibit strongly contrasting properties between layers. In addition, the interfaces between layers vary in strength (friction and cohesion) and, when weak, they provide preferential directions to rock failure and fluid flow. Traditional rock mechanics modeling for hydraulic fracturing, wellbore stability, stress prediction, and other petroleum-related applications assume homogeneous rocks and welded interfaces. This assumption is hard to reconcile with the strongly layered texture and varied layer composition observed in unconventional rocks.

Using the finite element method (FEM), we investigated the consequences of the presence of rock layers and weak interfaces on three different subjects: 1) formation shear stress development, shear slip at interfaces, and wellbore stability; 2) hydraulic fracture height growth; and 3) casing shear impairment.

For the first scenario in this work, three different layered rock models were simulated and compared: laterally-homogeneous, laterally-heterogeneous, and strongly laterally-heterogeneous. Results show that localized shear stresses develop along interfaces between layers with contrasting properties and along the wellbore walls. It was also seen that rock shear and slip, along interfaces between layers, may occur when the planes of weakness are pressurized (e.g., during hydraulic fracturing).

In the second scenario, we used a range of tensile strength and fluid flow properties at the interfaces between layers, to investigate their impact on vertical propagation of hydraulic fracture. The results show a systematic decrease in fracture height and fracturing fluid efficiency with increasing interface hydraulic conductivity and/or decreasing interface strength. We also propose that fluid viscosity has a strong influence on fluid efficiency as well as fracture height growth.

In the third scenario, finite-element simulations were also conducted in a casing-cement-formation system to evaluate casing curvature and plastic deformation caused by formation shear movement occurring with slippage along the weak interface between two distinct rock layers. The results indicate that the abrupt curvature change and the plastic deformation along the casing are generated near the slip surface. We also observe that casing shear at the peak temperature during a single thermal cycle of cyclic steam stimulation induces higher casing plastic deformations.

DEDICATION

This dissertation is dedicated first to God for providing this amazing opportunity. I believe God has done everything to lead me to accomplish this doctorate. During this long journey, I have faced many difficulties and been frustrated by an invisible future. After asking for God’s help in prayer, he has placed great people and opportunities along my path and gave me great wisdom to get through the difficulties. I love and thank God for being with me and my family.

I also dedicate this to my lovely wife, Minyoung Lee, for her patience, love, and unstinted support. Without her, I could not have started and completed this doctorate here at Texas A&M University. She has always encouraged me even when she had complaints against me. Minyoung, I really thank you for accepting to have this adventure together and making sacrifices for your family through this tough time. I cannot leave out my son, Philip Rho. Since he was born in the first semester of this Ph.D. program, he has been the reason for my smile and happiness even on bad days. I love them, Minyoung and Philip, and thank God for sending them to me.

ACKNOWLEDGEMENTS

First and foremost, I would like to express my sincere appreciation to my advisor, Dr. Samuel Noynaert. When I transitioned to petroleum engineering, to be honest, first I was really doubtful if I could pursue a doctoral degree in this department because my background had been civil/geotechnical engineering for a long time. I thought my ability to reason was already limited to a way of thinking as a civil engineer. Actually in the beginning, I had some problems with finding a way of solving reservoir engineering problems because I approached the new problems with my civil/geotechnical engineering background knowledge. However, the improved way of thinking and solving skills of petroleum engineering problems have fostered me to have a capacity for various thoughts and to find creative solutions for an engineering problem, alongside my civil engineering background.

If I had not met Dr. Noynaert, I would have had a big problem continuing this doctorate or may have even stopped it. His consideration and encouragement have let me think and use my own valuable skills I obtained from my previous experiences. His contributions have been unlimited, in all the ways in which he has supported me as well as academically. He has not been just an academic advisor but a real mentor during my doctoral study and life in the United States. He has always encouraged me and provided me a better environment to let me devote myself to this doctorate. I really believe in the power of praise to make people successful. Dr. Noynaert has always given unstinted praise to me, believed in and supported me. I have been very lucky and grateful to have him as my advisor.

I also must thank Dr. Roberto Suarez-Rivera for his unstinted advice and help to accomplish this dissertation. I learned a lot of things from work with him at W.D. Von Gonten Laboratories, LLC, which cannot be learnt from school. The practical lessons from working with the industry people have prevented me thinking inside the box. I really thank Dr. Suarez-Rivera for providing me all these opportunities. Also, I have been really honored to know and work with him during my doctoral study.

I also gratefully acknowledge my committee members, Dr. Jerome Schubert, Dr. Kan Wu, and Dr. James Boyd, for their valuable comments and guidance both inside and outside classrooms. Especially, Dr. Schubert and Dr. Wu's classes were great for me. When I first transferred to this petroleum engineering department, in the first semester, I had a little problem fully understanding reservoir engineering. However, Dr. Schubert's class, PETE 661 Drilling Engineering, let me get motivated to persist this career path. I was very interested in his lectures comparing to my background knowledge in geotechnical engineering. I am also thankful to Dr. Wu for her kind answers of my questions during her class, PETE 689 Rock Mechanics Related to Hydraulic Fracture. This class was directly related to my doctoral study and dissertation, so I was very lucky to take this course before graduation.

Also, I really thank Dr. Boyd for his input on my casing study, a part of my dissertation. Whenever I had trouble with the concepts about elastic and plastic behaviors of casing steels, he kindly explained them and led me in the right direction on the study. In addition, when I was stuck with modeling with ABAQUS, he introduced his students and let them help me to find a good solution. His interest in my country, South Korea, also has allowed me feel comfortable to contact and visit him even though he is a committee member from outside the department of petroleum engineering.

I also want to express my thanks to Dr. Andrew Bunger and his students, Navid Zolfaghari and Pengju Xing for their input on my American Rock Mechanics Association (ARMA) paper published in 2017. We met at the University of Pittsburgh, during my internship at W.D. Von Gonten Laboratories, LLC. Dr. Bunger fostered my numerical problem-solving skills through his wisdom and valuable advice. I also thank Navid for his help to improve my modeling skills associated with ABAQUS.

A special thanks must go to Mrs. Terri Smith for her technical writing class and help to review my papers and proposals. Whenever I asked for her help to review them, she always said okay without hesitation. Her comments and recommendations on them were very helpful.

I cannot leave out words of thanks to all my friends and colleagues for their friendship and encouragement. Especially, I must thank Soon-do Hwang who is no different than my real older brother. He always welcomed me whenever I went to my country for relaxation and refreshment from hard work.

Finally, I would greatly like to thank to my family for their love and encouragement. Especially I am very thankful to my in-laws for their prayer and unstinting support for me.

CONTRIBUTORS AND FUNDING SOURCES

Contributors

This work was supervised by a dissertation committee consisting of Professors Noynaert (chair), Schubert and Wu of the Harold Vance Department of Petroleum Engineering and Professor Boyd of the Department of Aerospace Engineering.

The work conducted for Sections 2 and 3 was completed by the student under the main guidance of Dr. Suarez-Rivera of W.D. Von Gonten Laboratories, LLC. The work for Section 3 was also conducted under the advisement of Navid and Professor Bunger of the Department of Civil & Environmental Engineering at the University of Pittsburgh and was published in 2017.

All other work conducted for the dissertation was completed by the student independently or under the advisement of all the dissertation committee members, especially the chair.

Funding Sources

This work conducted during the student’s doctoral study was supported by Tenaris, U.S. Steel and W.D. Von Gonten Laboratories, LLC.

NOMENCLATURE

API	American Petroleum Institute
CSS	Cyclic Steam Stimulation
CZ	Cohesive Zone
CZM	Cohesive Zone Model
EL	Elongation
EOR	Enhanced Oil Recovery
FEA	Finite Element Analysis
FEM	Finite Element Method
HC	Hydraulic Conductivity
HF	Hydraulic Fracture or Hydraulic Fracturing
KGD	Khristinaovic-Geertsma-de Klerk
LCF	Low Cycle Fatigue
LEFM	Linear Elastic Fracture Mechanics
NF	Natural Fracture
OD	Outer Diameter
PPCE	Pore-Pressure-Cohesive-Element
SAGD	Steam Assisted Gravity Drainage
SGS	Sequential Gaussian Simulation
S	Surface
V	Volume

$\{F\}$	Body Force Vector
$\{\Phi\}$	Surface Traction Vector
$\{\delta\varepsilon\}^T$	Strain Increment Vector
$\{\delta u\}^T$	Displacement Increment Vector
$\{\sigma\}$	Internal Stress Vector
$\{d\}$	Nodal Displacement Vector
$\{u\}$	Internal Displacement Vector
u, v, w	Displacement Parameters at Any Point in Cartesian Coordinates
$\{\varepsilon\}$	Internal Strain Vector
$[N]$	Shape Function Matrix
$[B]$	Strain-Displacement Matrix
$[E]$	Young’s Modulus Matrix
$\{\varepsilon_0\}$	Initial Strain Vector
$\{\sigma_0\}$	Initial Stress Vector
$[k]$	Element Stiffness Matrix
$\{f\}$	Nodal Force Vector
$[K]$	Global Stiffness Matrix
$\{D\}$	Global Displacement Vector
$\{F\}$	Global Displacement Vector
σ_v	Total Vertical Stress
σ_H	Maximum Total Horizontal Stress
σ_h	Minimum Total Horizontal Stress

ε_H	Lateral Tectonic Strain (in the direction of σ_H)
E_v, E_h, E_H	Young's Moduli Associated with the Directions of σ_v, σ_h, and σ_h
ν_v, ν_h, ν_H	Poisson's Ratios Associated with the Directions of σ_v, σ_h, and σ_h
τ	Shear Stress
τ_{max}	Maximum Shear Stress
S_y	Yield Strength
S_u	Ultimate Strength
c'	Cohesion
σ'	Effective Stress
ϕ'	Friction Angle
μ	Friction Coefficient
${\sigma_v}'$	Effective Vertical Stress
${\sigma_H}'$	Maximum Effective Horizontal Stress
${\sigma_h}'$	Minimum Effective Horizontal Stress
$(\sigma_\theta)_{max}$	Maximum Tangential Stress
$(\sigma_\theta)_{min}$	Minimum Tangential Stress
α	Biot Coefficient
P_p	Pore Pressure
ΔP	Difference Between the Fluid Pressure in the Formation and That in the Borehole
K_0	Coefficient of Lateral Earth Pressure at Rest
K_1, K_2	Parameters of Material Anisotropic Elastic Properties

τ_{12}	Shear Stress in x-y Plane
τ_{23}	Shear Stress in y-z Plane
τ_{1f}, τ_{2f}	Frictional Shear Stresses in Principal Directions 1 and 2
E	Young’s Modulus
G	Shear Modulus (= $E/2(1+v)$)
v	Poisson’s Ratio
T	Traction in the Traction-Separation Law
T_{max}	Maximum Tensile Stress
G_c	Fracture Energy
K_{IC}	Fracture Toughness
δ	Separation in the Traction-Separation Law
δ_0	Critical Separation at Damage Initiation
δ_f	Critical Separation at Complete Failure
K	Cohesive Stiffness
α	Critical Separation Ratio (= δ_0/δ_f)
x	Fracture Length
q	Local Flow Rate per Unit Height
q_l	Local Fluid Loss to the Permeable Medium
w	Fracture Opening
p	Fluid Pressure
t	Time
u	Average Fluid Velocity Over the Cross-Section of the Fracture

μ	Fluid Dynamic Viscosity
k_t	Tangential Permeability
t_{orig}	Initial Thickness of the Crack
t_{curr}	Current Thickness of the Crack
g_{init}	Small, Non-physical Initial Opening
d	Numeric Fracture Opening (= $t_{curr} - t_{orig} + g_{init}$)
$\hat{d}$	Actual Fracture Opening Used in ABAQUS (= $t_{curr} - t_{orig}$)
K	Hydraulic Conductivity
κ	Intrinsic Permeability
ρ	Fluid Density
g	Gravitational Acceleration
$\sigma_{xx}, \sigma_{yy}, \sigma_{zz}$	Normal Stresses in Cartesian Coordinates
$\tau_{xy}, \tau_{zx}, \tau_{yz}$	Shear Stresses in Cartesian Coordinates
$\gamma_{xy}, \gamma_{zx}, \gamma_{yz}$	Engineering Shear Strains in Cartesian Coordinates
$\varepsilon_{xy}, \varepsilon_{zx}, \varepsilon_{yz}$	Shear Strains in Cartesian Coordinates
E_1, E_2, E_3	Young's Moduli Associated with the Material's Principal Directions
v_{12}, v_{13}, v_{23}	Poisson's Ratios Associated with the Material's Principal Directions
G_{12}, G_{13}, G_{23}	Shear Moduli Associated with the Material's Principal directions
E_p	Young's Modulus in the Plane of Isotropy
E_t	Young's Modulus in the Normal Direction to the Plane of Isotropy
v_p	Poisson's Ratio in the Plane of Isotropy
v_{pt}	Poisson's Ratio in the Normal Direction to the Plane of Isotropy

ν_{tp}	Poisson’s Ratio That Identifies the Strain in the Plane of Isotropy Developing from Stress Normal to It
G_p	Shear Modulus in the Plane of Isotropy (= $E_p/2(1+\nu_p)$)
G_t	Shear Modulus in the Normal Direction to the Plane of Isotropy
Q_0	Injection Rate
E'	Plane Strain Elastic Modulus
$w(x,t)$	Fracture Opening
$l(x,t)$	Fracture Half-Length
$p(x,t)$	Net Fluid Pressure
$\varepsilon(t)$	Small Dimensionless Number
$L(t)$	Lengthscale of the Fracture Half-Length
$P(t)$	Dimensionless Evolution Parameter
ξ	Scaled Coordinate $(= x/l(t))$ $(0 \leq \xi \leq 1)$
Ω	Dimensionless Crack Opening
γ	Dimensionless Crack Opening or Radius
Π	Dimensionless Net Fluid Pressure
ε_m, L_m	Dimensionless Parameters in a Viscosity Scaling
ε_k, L_k	Dimensionless Parameters in a Toughness Scaling
κ_m	Dimensionless Toughness
M_k	Dimensionless Viscosity
T	Temperature
D_{max}, D_{min}	Maximum and Minimum Outer Diameters

TABLE OF CONTENTS

Page

LIST OF FIGURES

Page

Page

Page

LIST OF TABLES

1. INTRODUCTION

1.1 Problems

Traditional rock mechanics model assumes homogeneous rocks and welded interfaces. However, unconventional reservoir systems are heterogeneous, thinly layered, and often exhibit strongly contrasting properties between layers and the associated varying interface strength. When tectonic stresses are applied, shear stress and shear displacement develop in a heterogeneous layered rock system. When the interface between layers are week, shear failure along the interface may occur. If the contrast in elastic properties (such as Young's modulus and Poisson's ratio) between layers is large, the interface is weaker and more susceptible to shear failure because the two layers at the interface do not deform the same amount. Shear slip along weak interfaces can result in serious economic loss by wellbore instability, casing shear failure, and reduced well production by the reduced fracture height growth after hydraulic fracturing.

When addressing unconventional reservoirs, such as shale and mudstone, numerical simulation of the hydraulic fracture propagation is more challenging due to the nature of the rocks and the influence of the associated interfaces between layers on hydraulic fracture height growth. Conventional methods for numerical modeling of hydraulic fractures were developed for homogeneous and elastic rocks. These generally do not provide adequate solutions for inhomogeneous, layered rocks with strongly contrasting elastic properties.

Hydrocarbon production is proportional to the propped surface area that is in contact with the reservoir and remains connected to the wellbore. Yet, the propped surface area controlling production appears to be considerably smaller than the surface area created during pumping. Somehow hydraulic fractures are disconnected, truncated, and reduced during production. One important mechanism causing this segmentation is the opening and shear displacement of weak interfaces between rock layers with contrasting properties. Therefore, for better predictions of well production, it is important to evaluate the relationships among interface properties (strength and fluid flow properties), fluid loss along the interfaces, and fracture height growth.

When the presence of weak interfaces between adjacent rock layers exists, formation slip accompanied by shear failure along the interfaces may occur and consequently result in casing shear when the interfaces intersect the paths of wells at depth. The localized horizontal shear at the planes of weakness including bedding planes can be driven by many sources: tectonic movement induced by geologic structure, reservoir compaction or heave, vertically growing hydraulic fractures, non-uniform thermal expansion rates of formation layers during a thermal recovery process, and other formation in-situ stress changes. In this study, as the primary source of formation slippage-related casing shear deformation, the thermal recovery processes such as cyclic steam stimulation (CSS) and steam assisted gravity drainage (SAGD) are considered. The casing impairment induced by formation shear slip can also result in serious economic loss causing casing failure, loss of well integrity, and loss of access to wells during completion operations.

1.2 Objectives of Study

As mentioned in the previous section, it is important to understand the sources of formation and casing shear and hydraulic fracture segmentation, and consequently the layered and heterogeneous nature of the reservoir and the existence of interfaces between layers. The main purposes of this study are to investigate the consequences of the presence of rock layers and weak interfaces on:

1) formation shear stress development, shear slip along interfaces, and wellbore stability,
2) hydraulic fracture height growth, and
3) casing shear impairment.

The topics shown above are considered and investigated as separate scenarios with their own numerical simulations.

The primary intent of the first scenario is to investigate the consequences of the existence of contrasting mechanical properties and non-welded interfaces between layers, on the development of localized shear stresses and shear displacements at the weak interfaces as well as on wellbore stability. Increased potential interface slip during hydraulic fracturing is also investigated. In the second scenario, using numerical representation of hydraulic fracture propagation through layered rocks, the effects of rock layering and interfaces on fracture height growth are investigated. Localized and total fluid loss along the interfaces and the associated fluid efficiency are also evaluated. The main purpose of the third scenario is to examine casing impairment induced by formation shear movement occurring with slippage along the weak bedding-plane interface between adjacent rock layers. We also investigated the impact of thermally-induced stresses and diminished material properties at elevated temperatures, on casing plastic deformation.

1.3 Outline of Dissertation

Section 1, a section of introduction, provides the main problems and objectives of this research work. The outline of this dissertation is also provided in this section. Numerical challenges for the existence of rock layers and weak interfaces in unconventional reservoirs are presented and the methodologies of numerical simulations are also introduced. Objectives are presented under three different scenarios of simulations.

Sections 2, 3 and 4 are the main body of this dissertation, and include numerical simulations of each scenario shown in the previous section. As a paper format, each section has subdivisions such as introduction, basic definitions and theories, finite element model setup, numerical simulations, and conclusions.

In section 2, the effect of rock layers and weak interfaces on formation shear stress development, shear slip along interfaces, and wellbore stability was investigated. 3D finite-element simulations were conducted on layered and discontinuous rocks, and specifically, organic mudstones and carbonate sequences. Three different layered rock models were investigated and compared: laterally-homogeneous, laterally-heterogeneous, and strongly laterally-heterogeneous models.

In section 3, the effect of rock layers and weak interfaces on vertical propagation of hydraulic fracture was investigated. The relationships between overall fracture loss at interfaces, fracture height growth and fracturing fluid efficiency were also evaluated. To validate the model and for comparison, we conducted simulations on elastically-homogeneous and elastically-layered rocks and, for the latter, we used a range of tensile strength and fluid flow properties at the interfaces between layers, to understand their impact on vertical hydraulic fracture (height) growth.

In section 4, the effect of rock layers and weak interfaces on casing impairment induced by formation shear movement was investigated. 3D finite-element simulations were conducted in a casing-cement formation system, to examine the casing curvature change, casing plastic deformation, and cement tensile failures induced by formation slip movement arising with shear failure along the planes of weakness between two distinct rock layers. This study discusses thermal recovery processes as the primary source of formation slippage-related casing shear failures. We also investigated the impact of thermally-induced stresses and diminished material properties at high temperatures, on casing shear damages.

In section 5, a section of conclusions, summary of this study were mainly presented. Limitations of the proposed numerical models and recommendations for future work were also addressed.

2. EFFECT OF ROCK LAYERS AND WEAK INTERFACES ON FORMATION SHEAR STRESS DEVELOPMENT, SHEAR SLIP ALONG INTERFACES, AND WELLBORE STABILITY

2.1 Introduction

Unconventional reservoir systems are heterogeneous, thinly layered, and often exhibit strongly contrasting properties between layers. In addition, the interfaces between layers vary in strength (friction and cohesion) and when weak they provide preferential directions to rock failure and fluid flow. The weak interfaces tend to have low tensile strength, low shear strength, and high hydraulic conductivity. Thus, they easily detach (in tension) and slip (in shear), as the hydraulic fracture approaches and intersects them, allowing for fluid penetration and leak off. Weak interfaces most often occur between layers of strongly contrasting properties (unconformities, or at the contacts of layers deposited over erosional surfaces). Traditional rock mechanics modeling for hydraulic fracturing, wellbore stability, stress prediction, and other petroleum-related applications assume homogeneous rocks and welded interfaces. This assumption is hard to reconcile with the strongly layered texture and varied layer composition observed in unconventional rocks (Figure 2.1).

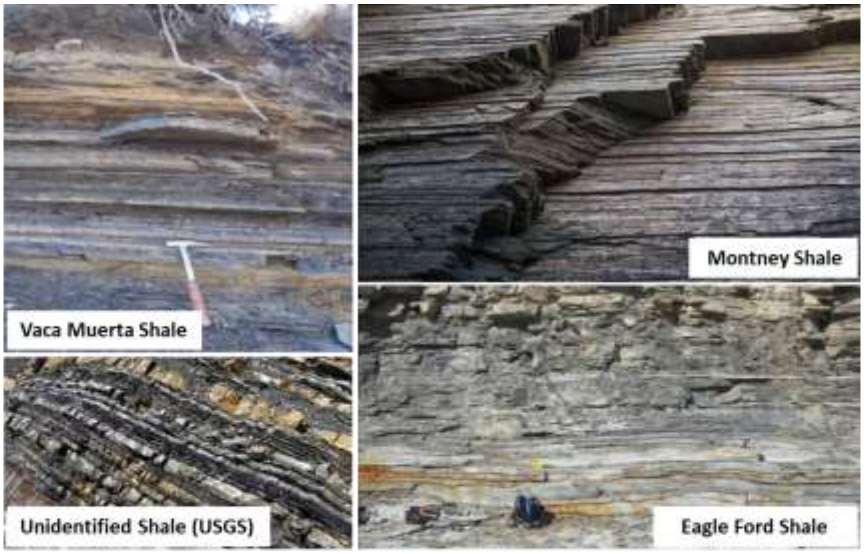

Figure 2.1 - Strongly layered and heterogeneous nature in unconventional rocks often not accounted for in modeling (modified from Suarez-Rivera et al., 2016).

In this work, we conducted numerical simulations on layered and discontinuous rocks, specifically organic-rich mudstones and carbonate sequences, to investigate the effect of rock layers with contrasting mechanical properties, and with weak interfaces between layers, on hydraulic fracturing, wellbore stability and stress development. In particular, we are interested in the potential development of localized shear stresses and shear slip along the interfaces between rock layers, which are defined in the homogeneous model as principal planes. This mechanism often results in fracture segmentation and is responsible for the differences that occur between the fracture that is created during fracturing and the fracture that remains connected to the wellbore after fracturing and during production. This study was motivated primarily by problems of bedding-plane slip, however we also discuss implications to wellbore instability and fracture segmentation occurring during hydraulic fracturing in unconventional reservoirs

(Cooke and Underwood, 2001; Gu et al., 2008; Zhang, 2013; Suarez-Rivera et al., 2013; Rutledge, 2016).

The effect of casing deformation and shear failure during long-term reservoir production has been previously investigated and reported (Hilbert et al., 1996; Hilbert et al., 1999; Dusseault et al., 2001; Bruno, 2002; Furui, et al., 2012, Han et al., 2006; Hu et al., 2016, Yudovich, et al, 1989). These authors highlighted multiple causes of shear failure during field operations, and recommend a number of mitigation strategies to prevent them. These included reservoir pressure maintenance, altering the well trajectories to avoid regions with shear, use of casing with deformable joints, and others. More recently, several researchers have investigated casing shear during hydraulic fracturing (Bar-Cohen and Zacny, 2009; Dusseault, 2011; Zhonglan et al., 2015) and evaluated the pressure and stress alteration during hydraulic fracturing, and the presence and failure of geologic faults, as the main causes of these failures. Our hypothesis is that rock heterogeneity, fluid leakoff, and the increase in pressure, along weak interfaces between rock layers with contrasting properties are the causes of casing shear failures during hydraulic fracturing. We propose that shear slip along weak interfaces may be possible during hydraulic fracturing, and given their bed-parallel orientation, and highest concentration along the vertical direction, vertical wells are more susceptible to this form of failure. To evaluate this potential risk, we created vertically-heterogeneous rock models, representing their layered fabric, and defined these layers with contrasting rock properties. In addition, we consider that each of these layers could be horizontally homogeneous and heterogeneous.

Elastic-rock heterogeneity, including the vertical heterogeneity of layered rocks, has been investigated previously (Bourne, 2003; Langenbruch and Shapiro, 2015). Different methods for homogenization and scaling of layered heterogeneous media have been proposed (Warren and Price, 1961; Deutsch, 1989; King 1989; Norris et al., 1991; Khajeh et al., 2012). The Sequential Gaussian Simulation (SGS) technique is commonly used to define the spatial variability of material properties. SGS represents the material properties by inputting a random variable, transforming them into Gaussian random variables with zero mean and unit variance, by defining the spatial correlation of the random data, and then conducting Monte Carlo simulations (Elkateb et al., 2003).

In this study, we define the lateral-heterogeneity of the layered rocks using a concept similar to SGS and treat the rock elastic properties of Young's modulus, shear modulus, and Poisson's ratio as the material properties represented with random variables. We did not include any spatial correlation information to the distribution of these properties and define them by a uniformly distributed set of random values within a prescribed finite range. This results in property variability with non-correlated distributions. In reality, the distributions of rock properties are correlated to some extent, however, this effect was not investigated in this initial work.

We first examined the development of shear stress in laterally-homogeneous and laterally-heterogeneous layered reservoirs, as resulting by the in-situ stress loading, defined by a combination of gravity loading and lateral tectonic deformation. We also evaluated the potential for traditional wellbore shear failures and shear development at interfaces along the wellbore walls, under the same conditions. We then conducted an analysis of fluid leakoff, increased pressure along interfaces, and potential interface slip as would be experienced during hydraulic fracturing treatments. The above numerical investigations are the unique objective and novelty of this work, which have not been previously studied, as our extensive literature survey (conducted as part of the field work) showed it.

The laterally-homogeneous model represents a reservoir made of layers of different material properties, often with strongly contrasting properties. However, each layer is homogeneous and is defined with properties that are invariant with location. The laterally-heterogeneous model is similar to the previous, but in this case each layer is heterogeneous and exhibits a random distribution of properties along its lateral extent in the range ±20% from their reference values. The strongly laterally-heterogeneous model is identical to the previous but the random variability of elastic properties is ±50%.

The stress development at interfaces between layers and the potential generation of localized shear slip are investigated using the Coulomb slip failure model. The effect of water movement along weak interfaces during hydraulic fracturing is evaluated by assuming a reduction of the friction coefficient. Results provided an increased understanding of shear slip on laterally-homogeneous and laterally-heterogeneous layered reservoirs when the planes of weakness were pressurized. The economic consequences of shear slip along weak interfaces are associated to the reduced fracture height growth by fracture segmentation or by high fluid loss into the interfaces, and the resulting reduction of well production. The formation of shear slip may also cause shearing-caused casing failures and loss of well accessibility. Thus, the induced shear stress and shear slip of weak interfaces should be considered in proper design of casing/cement in wells. Developing adequate mitigation strategies for these problems depends on understanding the sources of shear, and consequently, the layered and heterogeneous nature of the reservoir.

2.2 Basic Definitions and Theories

2.2.1 Elastic Stress and Strain in Rocks

2.2.1.1 Stress Matrix in Linear Elasticity

Figure 2.2 shows the stress notations of compressive and positive shear stresses in a xyz coordinate system commonly used in ABAQUS, but it should be noted that in continuum mechanics the x- and y- axes typically represent the horizontal directions and the z-axis typically represents the vertical direction. The nine stress components can be organized and written in a stress matrix, which is given by

$$\begin{pmatrix} \sigma_{xx} & \tau_{xy} & \tau_{xz} \\ \tau_{yx} & \sigma_{yy} & \tau_{yz} \\ \tau_{zx} & \tau_{zy} & \sigma_{zz} \end{pmatrix} \tag{2.1}$$

where σ_{xx}, σ_{yy}, and σ_{zz} are the normal stresses acting on the surfaces normal to the x, y, and z directions, respectively; τ_{xy}, τ_{yx}, τ_{xz}, τ_{zx}, τ_{yz}, and τ_{zy} are the shear stresses. The first subscript of the stress shows the direction of the surface which the stress vector acts and the second subscript shows the direction of the stress component. The shear stresses across the diagonal are identical and have the following relations:

$$\tau_{xy} = \tau_{xy}, \quad \tau_{xz} = \tau_{zx}, \quad \tau_{yz} = \tau_{zy} \tag{2.2}$$

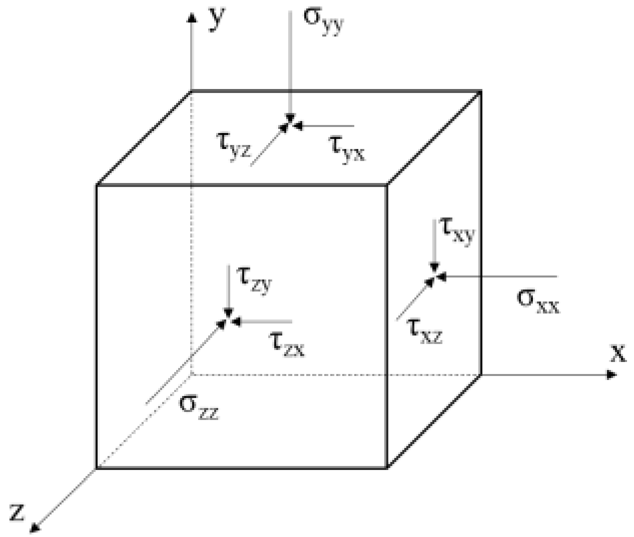

Figure 2.2 - Stress notations in the three-dimensional space used in this study (modified from Helwany, 2007). The sign convention used in rock mechanics is opposite to that employed in ABAQUS.

2.2.1.2 Isotropy

The most general and simplest form of linear elasticity is the generalized Hooke's law, for an isotropic material which is called when the elastic properties (such as Young's modulus, *E*, and Poisson's ratio, *v*) are orientation dependent. The generalized Hooke's law for isotropic materials is given by

$$\begin{bmatrix}\sigma_{xx}\\ \sigma_{yy}\\ \sigma_{zz}\\ \tau_{xy}\\ \tau_{zx}\\ \tau_{yz}\end{bmatrix} = \frac{E}{(1+\nu)(1-2\nu)}\begin{bmatrix}1-\nu & \nu & \nu & 0 & 0 & 0\\ \nu & 1-\nu & \nu & 0 & 0 & 0\\ \nu & \nu & 1-\nu & 0 & 0 & 0\\ 0 & 0 & 0 & 1-2\nu & 0 & 0\\ 0 & 0 & 0 & 0 & 1-2\nu & 0\\ 0 & 0 & 0 & 0 & 0 & 1-2\nu\end{bmatrix}\begin{bmatrix}\varepsilon_{xx}\\ \varepsilon_{yy}\\ \varepsilon_{zz}\\ \varepsilon_{xy}\\ \varepsilon_{zx}\\ \varepsilon_{yz}\end{bmatrix} \qquad (2.3)$$

Some literatures may use engineering shear strains, γ_{xy}, γ_{zx}, and γ_{yz}, where $\gamma_{xy} = \varepsilon_{xy} + \varepsilon_{yx} = 2\varepsilon_{xy}$, etc., multiplying each shear strain of ε_{xy}, ε_{zx}, and ε_{yz} by a factor 2. Eq. (2.3) can be inverted to obtain

$$\begin{bmatrix} \varepsilon_{xx} \\ \varepsilon_{yy} \\ \varepsilon_{zz} \\ \varepsilon_{xy} \\ \varepsilon_{zx} \\ \varepsilon_{yz} \end{bmatrix} = \begin{bmatrix} 1/E & -\nu/E & -\nu/E & 0 & 0 & 0 \\ -\nu/E & 1/E & -\nu/E & 0 & 0 & 0 \\ -\nu/E & -\nu/E & 1/E & 0 & 0 & 0 \\ 0 & 0 & 0 & 1/2G & 0 & 0 \\ 0 & 0 & 0 & 0 & 1/2G & 0 \\ 0 & 0 & 0 & 0 & 0 & 1/2G \end{bmatrix} \begin{bmatrix} \sigma_{xx} \\ \sigma_{yy} \\ \sigma_{zz} \\ \tau_{xy} \\ \tau_{zx} \\ \tau_{yz} \end{bmatrix} \tag{2.4}$$

where the shear modulus G can be given by $G = E/2(1+\nu)$.

2.2.1.3 Transverse Isotropy

A transversely isotropic material possesses a plane of isotropy and different properties in orthogonal directions to the plane. For example, transversely isotropic multi-layered rocks have different elastic and strength properties in the horizontal and vertical directions.

Assuming the x-y plane to be the plane of isotropy at every point, the transversely isotropic rock is characterized by $E_1 = E_2 = E_p$, $\nu_{31} = \nu_{32} = \nu_{tp}$, $\nu_{13} = \nu_{23} = \nu_{pt}$, and $G_{13} = G_{23} = G_t$, where p and t represent “in-plane” and “transverse,” respectively (Abaqus, 2016). Thus, E_p is the Young’s modulus in the x-y symmetry plane. The Poisson’s ratios ν_{tp} and ν_{pt} characterize the strain in the plane of isotropy developing from stress normal to it and the transverse strain in the normal direction to the plane of isotropy resulting from stress in the plane, respectively. The quantities of ν_{tp} and ν_{pt} are not generally equal and are related by $\nu_{tp}/E_t = \nu_{pt}/E_p$, where E_t is the Young's modulus in z direction. The stress-strain laws are written by

$$\begin{bmatrix}\sigma_{xx}\\ \sigma_{yy}\\ \sigma_{zz}\\ \tau_{xy}\\ \tau_{zx}\\ \tau_{yz}\end{bmatrix} = \begin{bmatrix} \frac{1-\nu_{pt}\nu_{tp}}{E_pE_t\Delta} & \frac{\nu_p+\nu_{tp}\nu_{pt}}{E_pE_t\Delta} & \frac{\nu_{tp}+\nu_p\nu_{tp}}{E_pE_t\Delta} & 0 & 0 & 0\\ \frac{\nu_p+\nu_{pt}\nu_{tp}}{E_tE_p\Delta} & \frac{1-\nu_{tp}\nu_{pt}}{E_tE_p\Delta} & \frac{\nu_{tp}+\nu_{tp}\nu_p}{E_tE_p\Delta} & 0 & 0 & 0\\ \frac{\nu_{pt}+\nu_p\nu_{pt}}{{E_p}^2\Delta} & \frac{\nu_{pt}+\nu_p\nu_{pt}}{{E_p}^2\Delta} & \frac{1-\nu_p^2}{{E_p}^2\Delta} & 0 & 0 & 0\\ 0 & 0 & 0 & 2G_p & 0 & 0\\ 0 & 0 & 0 & 0 & 2G_t & 0\\ 0 & 0 & 0 & 0 & 0 & 2G_t \end{bmatrix} \begin{bmatrix}\varepsilon_{xx}\\ \varepsilon_{yy}\\ \varepsilon_{zz}\\ \varepsilon_{xy}\\ \varepsilon_{zx}\\ \varepsilon_{yz}\end{bmatrix} \qquad (2.5)$$

where ν_p is the Poisson's ratio in the x-y symmetry plane; G_p is the shear modulus in the x-y plane and given by $G_p = E_p/2(1+\nu_p)$; G_t is the shear modulus in z direction; Δ is given by

$$\Delta = \frac{(1+\nu_p)(1-\nu_p-2\nu_{pt}\nu_{tp})}{{E_p}^2E_t} \qquad (2.6)$$

The components across the diagonal in the stiffness matrix shown in Eq. (2.5) are also identical. Eq. (2.5) can also be inverted to yield

$$\begin{bmatrix}\varepsilon_{xx}\\ \varepsilon_{yy}\\ \varepsilon_{zz}\\ \varepsilon_{xy}\\ \varepsilon_{zx}\\ \varepsilon_{yz}\end{bmatrix} = \begin{bmatrix} 1/E_p & -\nu_p/E_p & -\nu_{tp}/E_t & 0 & 0 & 0\\ -\nu_p/E_p & 1/E_p & -\nu_{tp}/E_t & 0 & 0 & 0\\ -\nu_{pt}/E_p & -\nu_{pt}/E_p & 1/E_t & 0 & 0 & 0\\ 0 & 0 & 0 & 1/2G_p & 0 & 0\\ 0 & 0 & 0 & 0 & 1/2G_t & 0\\ 0 & 0 & 0 & 0 & 0 & 1/2G_t \end{bmatrix} \begin{bmatrix}\sigma_{xx}\\ \sigma_{yy}\\ \sigma_{zz}\\ \tau_{xy}\\ \tau_{zx}\\ \tau_{yz}\end{bmatrix} \qquad (2.7)$$

2.2.2 Shear Slip Mechanism

The Coulomb failure criterion is expressed as a linear relationship between the normal stress applied on the sliding plane and the shear stress required for shear failure, see Figure 2.3. The relation is written as

$$\tau = c' + \sigma' tan\phi' \tag{2.8}$$

where, τ is the shear stress on the sliding plane at the onset of slip (at failure); σ' is the effective stress normal to the sliding plane; c' is the cohesion of the sliding plane; and ϕ' is the friction angle of the sliding plane. The friction coefficient μ is calculated from the friction angle ϕ', as $tan\ \phi'$. These two parameters define the frictional behavior and failure of the sliding plane and can be obtained experimentally via laboratory testing, by determining the shear stress required for slip failure under increasing levels of the effective normal stress. These conditions of shear stress and normal stress are plotted in the Mohr space and the linear fit to the experimental data is used to define c' (the intercept at zero effective normal stress) and ϕ' (the slope of the linear fit) as seen in Figure 2.3.

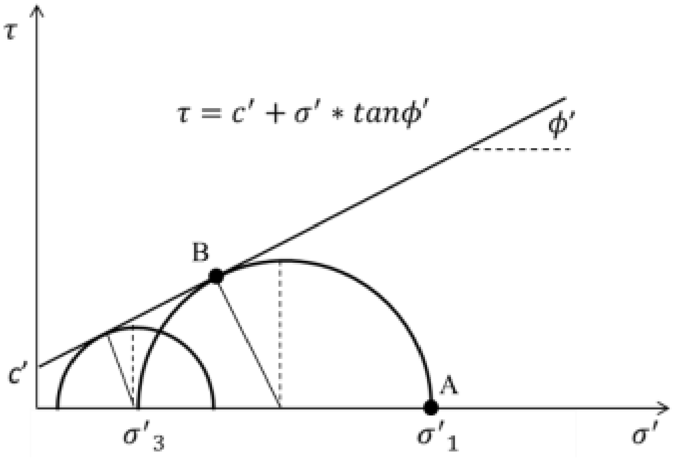

Figure 2.3 - Coulomb failure criterion and Mohr stress representation. Results from two laboratory tests are represented. c' and ϕ' are the cohesion and the friction angle of the sliding plane. σ'_1 and σ'_3 are the maximum and minimum principal stresses of each Mohr diagram.

The orientation of the plane of weakness in Figure 2.3 (point B) is arbitrary and larger than 90 deg in the Mohr space (which corresponds to an orientation larger than 45 deg in the real space). For the purpose of this study, we are interested in planes that are bed-parallel and perpendicular to σ' (point A). The Mohr representation indicates that this is a plane with no shear, and consequently no shear failure, independent of the magnitude of the normal stress (i.e., the interfaces between rock layers are predominantly bed-parallel and are principal planes). The purpose of these investigations is to evaluate if material heterogeneity, in the form of layering and lateral-heterogeneities within layer, sufficiently perturb the distribution of local stresses (magnitude and orientation), such that localized shear can be developed along regions in these interfaces.

2.2.3 Radial and Tangential Stresses Around a Wellbore

The relationships for stress concentrations around a wellbore in homogeneous, isotropic elastic rocks, and subjected to different principal stresses along its boundaries are well known (Kirsch, 1898 and Jaeger and Cook, 1979) as shown in Figure 2.4. Disregarding any thermal stresses, the maximum and minimum hoop stress concentrations that develop around a wellbore in elastically-isotropic rocks are represented in the following expressions:

$$(\sigma_\theta)_{max} = 3\sigma_H' - \sigma_h' - \Delta P \tag{2.9}$$

$$(\sigma_\theta)_{min} = 3\sigma_h' - {\sigma_H}' - \Delta P \tag{2.10}$$

where $(\sigma_\theta)_{max}$ is the maximum tangential stress; $(\sigma_\theta)_{min}$ is the minimum tangential stress; and ΔP is the difference between the fluid pressure in the formation and that in the borehole. The wellbore is assumed to be impermeable.

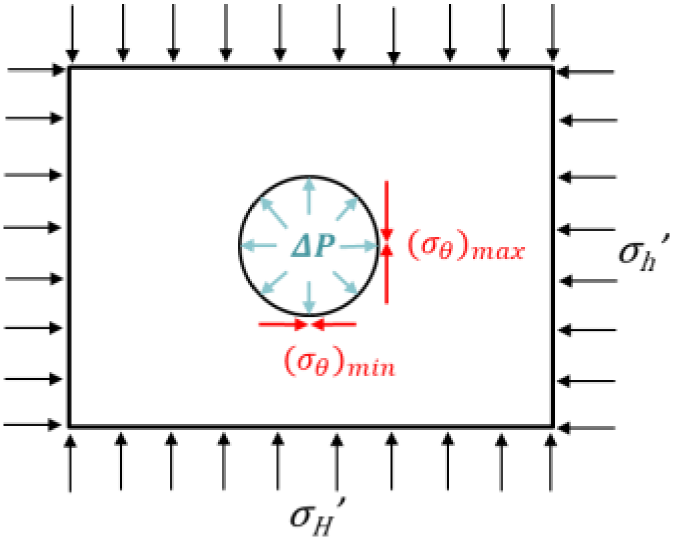

Figure 2.4 - Stress concentration around a wellbore in elastically-isotropic rocks. The maximum tangential stress $(\sigma_\theta)_{max}$ and the minimum tangential stress $(\sigma_\theta)_{min}$ develop around a wellbore under in-situ stresses of the maximum effective horizontal stress $\sigma_H{}'$ and the minimum effective horizontal stress $\sigma_h{}'$. ΔP represents the difference between the drilling mud pressure and the pore pressure.

2.2.4 Finite Element Formulation

Finite element method is a numerical approach for solving physically or geometrically complex problems that require approximate solution of partial differential equations. The method partitions the whole domain into small pieces called finite elements and yields approximate solutions of these partitions by interconnecting them at discrete points called nodes, to form a global solution valid over the entire domain (Zohdi, 2015).

Employing the principle of virtual work, for any quasistatic and admissible displacement, the virtual strain energy stored is equal to the virtual work done by prescribed body forces $\{F\}$ acting in volume V and surface tractions $\{\Phi\}$ acting on surface S. This relationship is given by (Cook et al., 2002)

$$\int \{\delta\varepsilon\}^T \{\sigma\} dV = \int \{\delta u\}^T \{F\} dV + \int \{\delta u\}^T \{\Phi\} dS \tag{2.11}$$

where $\int \{\delta\varepsilon\}^T$ and $\{\delta u\}^T$ are the vectors of strain and displacement increment, respectively; $\{\sigma\}$ is the stress vector.

An array of nodal displacements $\{d\}$ can be described by a displacement function $\{u\}$ which relates the nodal displacements to the internal displacements through an entire element and is defined as:

$$\{u\} = [N]\{d\} \tag{2.12}$$

where the matrix $[N]$ contains shape functions; $\{u\}$ contains three displacement parameters u, v and w at any point in three dimensional problems of elasticity and is written as:

$$\{u\} = [u \quad v \quad w]^T \tag{2.13}$$

Using the displacement function, the vector of internal strains within the element $\{\varepsilon\}$ are written in matrix from as:

$$\{\varepsilon\} = [B]\{d\} \tag{2.14}$$

where $[B]$ is the strain-displacement matrix and given by

$$[B] = [\partial][N] \tag{2.15}$$

Therefore, the internal stress throughout the element, from Hooke's Law, can be calculated by

$$\{\sigma\} = [E]\{\varepsilon\} = [E][B]\{d\} \tag{2.16}$$

where $[E]$ is the matrix of Young's modulus. From Eqs. (2.12) and (2.14), we obtain

$$\{\delta u\}^T = \{\delta d\}^T [N]^T \tag{2.17}$$

and

$$\{\delta \varepsilon\}^T = \{\delta d\}^T [B]^T \tag{2.18}$$

Substituting Eqs. (2.16) through (2.18) into Eq. (2.11) and including initial strain $\{\varepsilon_0\}$ and initial stress $\{\sigma_0\}$ give (Cook et al., 2002)

$$\begin{aligned}\{\delta d\}^T \bigg(\int [B]^T\, [E][B]\{d\} dV - \int [B]^T\, [E]\{\varepsilon_0\} dV + \int [B]^T\, \{\sigma_0\} dV - \int [N]^T\, \{F\} dV \\ - \int [N]^T\, \{\Phi\} dS \bigg) = 0 \end{aligned} \tag{2.19}$$

For any virtual displacement vector $\{\delta d\}^T$, Eq. (2.19) must be true and therefore yields the following simple relationship:

$$[k]\{d\} = \{f\} \tag{2.20}$$

where $[k]$ is the element stiffness matrix which is given by

$$[k] = \int [B]^T\, [E][B] dV \tag{2.21}$$

and $\{f\}$ is the nodal force vector which defines (Cook et al., 2002)

$$\{f\} = \int [N]^T\, \{F\} dV + \int [N]^T\, \{\Phi\} dS + \int [B]^T\, [E]\{\varepsilon_0\} d - \int [B]^T\, \{\sigma_0\} dV \tag{2.22}$$

Assembly of elements form global equations which are given by

$$[K]\{D\} = \{F\} \tag{2.23}$$

where $[K]$ is the global stiffness matrix; $\{D\}$ and $\{F\}$ are the global displacement vector and prescribed force vector, respectively.

2.3 Numerical Simulations

2.3.1 Layered Rock Architecture and Material Properties

Figure 2.5 shows the simplified stratigraphic sequence in an organic-rich mudstone reservoir. This is represented with 5 lithologies: a carbonate, three mudstones, and a sandstone. The basement rock is identical with the sandstone of Material 5. This is done to minimize the boundary effects at the contact between Materials 4 and 5, the Material 5 is simply extended to the boundaries of the model with the basement. The schematic layer architecture was constructed based on the seismic data, together with petrophysical logs and continuous core sections along the regions of interest, to define the layered fabric of the reservoir, the properties of the various rock layers, and the properties of their corresponding interfaces. The stratigraphy is primarily composed by stacked sequences of organic-rich mudstones and carbonates-rich lithologies. The name and location of this particular field will not be disclosed, however Figure 2.5 is shown to indicate that the present work is grounded on real field data from a known unconventional reservoir. A finite element model was developed to represent this simplified stratigraphy. For this work, a first order approximation was important, to evaluate the conditions of friction, cohesion, pore pressure, and others that would trigger failure along a plane of weakness. Clearly, in the field, rock layers and the behaviors along the weak planes are considerably more complex. However, understanding the simplified case would improve the possibility of understanding the complex case.

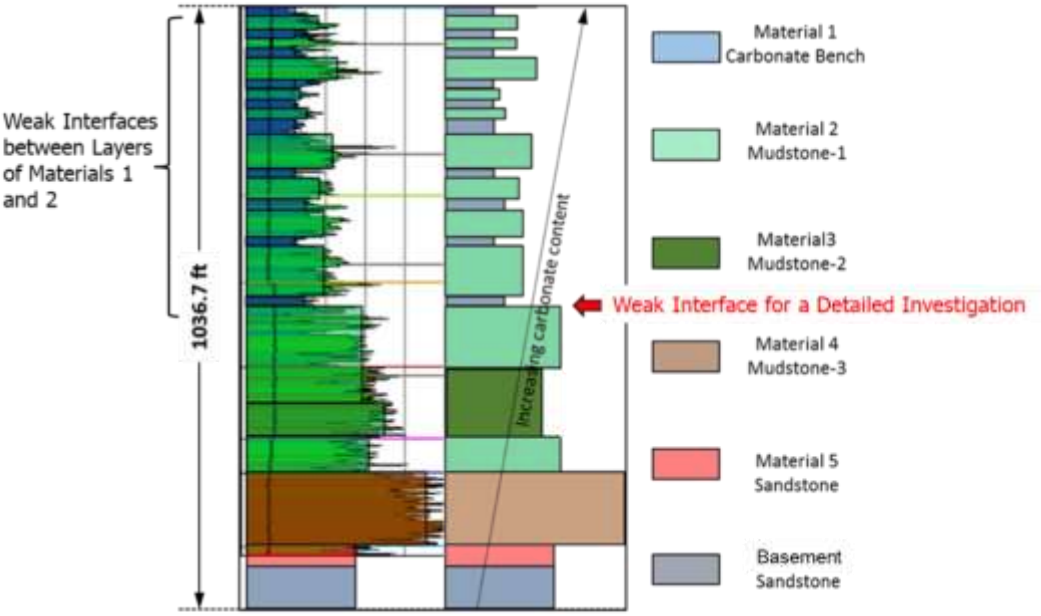

Figure 2.5 - Schematic layer architecture and its material distribution based on available field data. The interfaces between Materials 1 and 2 are weak due to their low friction coefficient and low shear strength with strongly contrasting properties. The interface which the red arrow indicates an arbitrary interface, selected to investigate the frictional shear stress development in both laterally-homogeneous and laterally-heterogeneous models, as shown in Figures 2.9 and 2.11, respectively.

The materials' elastic properties and strength properties are shown in Table 2.1. The carbonate and sandstone units (Materials 1 and 5) are isotropic and have identical elastic and strength properties in all directions. In contrast, the mudstone units (Materials 2, 3 and 4) are transversely isotropic rocks and have different elastic and strength properties in the horizontal (x,z) and vertical directions (y)[1]. Friction coefficients at the interfaces between the various lithologic contacts are shown in Table 2.2.

---

[1] Please notice that in this work the y-axis represents the vertical direction and the x- and z-axes represent the horizontal directions

Table 2.1 - Material properties of rocks.

Material	Young's Modulus (psi)		Poisson's Rato		Shear Modulus (psi)		Density (g/cc)	Peak Strength (psi)	Permerability (nD)	Porosity (%)	Void Ratio
1	**E_V**	9.040E+06	**v_V**	0.32	**G_V**	3.420E+06	2.8	65,394	50	3	0.0309
	E_H	9.040E+06	**v_H**	0.32	**G_H**	3.420E+06					
2	**E_V**	3.330E+06	**v_V**	0.15	**G_V**	1.090E+06	2.56	27,631	300	5	0.0526
	E_H	5.560E+06	**v_H**	0.18	**G_H**	1.440E+06					
3	**E_V**	1.790E+06	**v_V**	0.11	**G_V**	1.320E+06	2.51	18,174	300	5	0.0526
	E_H	3.598E+06	**v_H**	0.23	**G_H**	8.000E+05					
4	**E_V**	2.160E+06	**v_V**	0.225	**G_V**	1.036E+06	2.28	18,174	300	10	0.1111
	E_H	3.397E+06	**v_H**	0.316	**G_H**	8.800E+05					
5	**E_V**	4.000E+06	**v_V**	0.25	**G_V**	1.600E+06	2.5	20,250	1000	15	0.1765
	E_H	4.000E+06	**v_H**	0.25	**G_H**	1.600E+06					

Table 2.2 - Friction coefficient of interfaces. Cohesion was assumed to be zero at all interfaces.

Interface	Friction Coefficient, μ
Between Mat1 and Mat2	0.176
Between Mat2 and Mat3	0.364
Between Mat2 and Mat4	0.364
Between Mat4 and Mat5	0.840

Simplified stress-strain curves, based on their measured properties, were created for each of these layers to represent their behavior in the finite element modeling software used, ABAQUS. These simplified curves are shown in Figure 2.6 and provide a graphical representation of the elastic limit, the yield stress and the peak stress. It should be noted that the data in Figure 2.6 does not reflect the measured stress-strain behavior of the materials. Instead, it is a graphical representation of the constitutive law input into the FEA model, based on the properties in Table 2.1. Excluding the starting point, three stress points were selected: yield stress, ultimate stress, and the stress between them. The slope of these curves, within the elastic regime of deformation defines the Young’s modulus of each material. Figure 2.6 shows that the Young’s modulus and strength of the carbonate-rich units (Material 1) are considerably higher than the other rock units. One of the most calcareous mudstones (Material 2) has similar stress-strain behavior as the sandstone (Material 5). The other two mudstones (Materials 3 and 4) are weaker and less stiff due to lower Young's modulus.

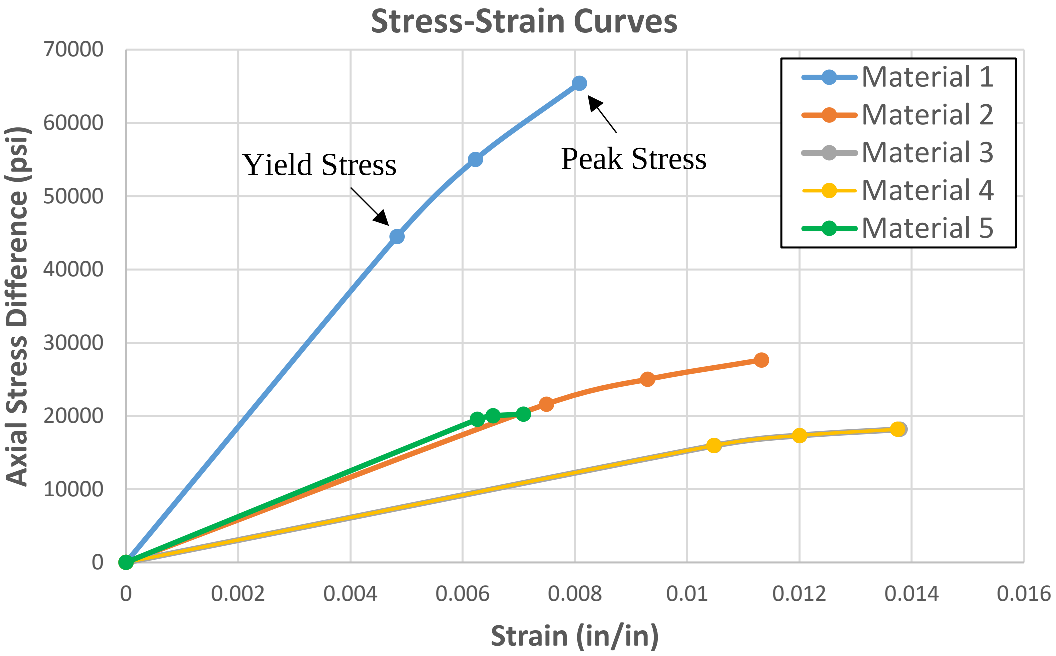

Figure 2.6 - Simplified stress-strain curves for Materials 1 to 5. The yield stress and peak stress of each material are indicated. The stress-strain relationships of Materials 3 and 4 are almost identical.

2.3.2 Finite Element Model

3D finite element simulations were conducted in ABAQUS using C3D20RP elements (20-node stress-pore pressure-coupled brick elements with reduced integration). Each node has 4 degrees of freedom (3 displacements and 1 pore pressure).

However, pore pressure was not evaluated explicitly in this study; the evaluation was conducted based on effective stresses and assuming that the poroelastic effect was fully equilibrated and small, and where the Biot coefficient α was taken as 1. Also, to simulate the overbalance pressure conditions during drilling a vertical well, an effective radial stress gradient of 0.05 psi/ft was applied to the borehole wall. The model represents a volumetric region with a length of 1000 ft, width of 600 ft, and height of 964.08 ft and was constructed using 203,592 elements with minimum and maximum element sizes of 0.196 ft and 70 ft in width, respectively.

The laterally-homogeneous model is built with each individual homogeneous layer defined with rock properties that are invariant with location while the laterally-heterogeneous model exhibits various rock properties in the horizontal direction of each layer. The lateral variability of Young’s modulus, shear modulus, and Poisson’s ratio, for each layer, was calculated using a random simulator based on a prescribed range (either ±20% or ±50%). All other rock properties were kept constant. Before generating the random values of the properties, the numerical model was divided into small blocks, each with an effective volume having a length of 125 ft, width of 30 ft, and height of approximately 15 to 40 ft depending on each layer thickness. The implementation of the random values into each block was attempted using the ABAQUS material subroutine (UMAT) for uniformly distributed random values of material properties within a finite range. The UMAT is generally written with Fortran 90 or higher versions. However, a limitation for using the random value generator in UMAT Fortran code was that the code generates new random values in every computation time step in ABAQUS.

Consequently, random values of the properties were generated in a Matlab code and exported to the UMAT Fortran code so that while initially randomly generated they would then remain fixed in value throughout a given simulation.

2.3.3 Development of In-Situ Stress

The in-situ stress was applied to the model by first allowing gravity to develop the vertical stress, under conditions of uniaxial vertical strain and no lateral deformation, and by subsequently applying a prescribed amount of lateral strain (approximately 0.03%), to represent tectonic deformation. This results in as much as 1.235 inches of vertical uplift. The vertical stress was defined to represent a highly overpressured reservoir system with an effective vertical stress gradient of 1.084 psi/ft. The effective horizontal stress (minimum and maximum) resulted from the combined effect of gravity loading and tectonic deformation. The effective in-situ stress is shown in Figure 2.7-a through 2.7-d. Figure 2.7-a shows the volumetric representation of the model after tectonic deformation. Figures 2.7-b, 2.7-c and 2.7-d compare the results of the numerical simulation with the corresponding in-situ stress values calculated analytically. The analytic solutions are expressed in the following formulas (Suarez-Rivera et al., 2011):

$$\sigma_h = K_0\left(\sigma_v - \alpha P_p\right) + \alpha P_p + K_1 \varepsilon_H \tag{2.24}$$

$$\sigma_H = K_0\left(\sigma_v - \alpha P_p\right) + \alpha P_p + K_2 \varepsilon_H \tag{2.25}$$

where σ_v, σ_h, and σ_H are the total vertical, minimum horizontal, maximum horizontal stresses, respectively; α is the Biot coefficient; P_p is the pore pressure; ε_H is the lateral tectonic strain in the direction of σ_H; K_0 is the coefficient of earth pressure at rest; K_1

and K_2 are the parameters representing the material anisotropic elastic properties. K_0, K_1, and K_2 are given by

$$K_0 = \left(\frac{E_H}{E_v}\right)\left(\frac{\nu_v}{1-\nu_H}\right) \tag{2.26}$$

$$K_1 = \frac{1}{E_v - E_v\nu_h - 2E_h\nu_v^2}\left(\frac{E_h(E_v\nu_h + E_h\nu_v^2)}{1+\nu_h} - \frac{E_h^2\nu_v^2}{1-\nu_h}\right) \tag{2.27}$$

$$K_2 = \frac{1}{E_v - E_v\nu_h - 2E_h\nu_v^2}\left(\frac{E_h(E_v - E_h\nu_v^2)}{1+\nu_h} - \frac{E_h^2\nu_v^2}{1-\nu_h}\right) \tag{2.28}$$

where E_v, E_h, and E_H are the Young's moduli in the directions of σ_v, σ_h, and σ_H, respectively; ν_v, ν_h, and ν_H are the Poisson's ratios in the directions of σ_v, σ_h, and σ_H, respectively. Each of effective stresses is obtained by subtracting the pore pressure multiplied by α from the total stress.

Good agreement is generally observed between the analytic- and the numeric-model results. The differences in the effective vertical stress distribution with depth results from the use of a constant average vertical gradient in the analytic model versus a layer by layer gradient, evaluated using the given bulk density of each rock type, in the numeric model.

The difference between the effective horizontal stress distributions with depth is also of interest. In the analytical model, the effective horizontal stress is calculated via effective vertical stress times a coefficient of lateral pressure at rest K_0. Given the same K_0 value for the analytical and the FEA models (these are simply associated to the elastic response of the rock), a higher effective vertical stress should result in higher effective horizontal stress. However, the FEA results show a lower horizontal effective stress (for the mudstones). The opposite is the case for the carbonates. The difference arises from the calculation of the horizontal stress associated to the tectonic straining. The analytical model assumes fully decoupled layers while the FEA model assumes coupled layers, in relation to their assigned friction and cohesion.

This is an evidence of the effect of the interfaces and their properties on in-situ stress developments under the tectonic shortening. The difference between the effective horizontal stress distributions from the analytic- and the numeric-model results vary with the interface properties. The larger the friction coefficient of the interfaces (assuming no cohesion), the higher the difference. The higher the friction coefficient, the stronger the interface, the least likely to fail (in shear), and thus the more similar to a welded (coupled) interface. Thus, the traditional rock mechanics assuming welded interfaces may fail to assess the realistic in-situ stress developments by the tectonic straining.

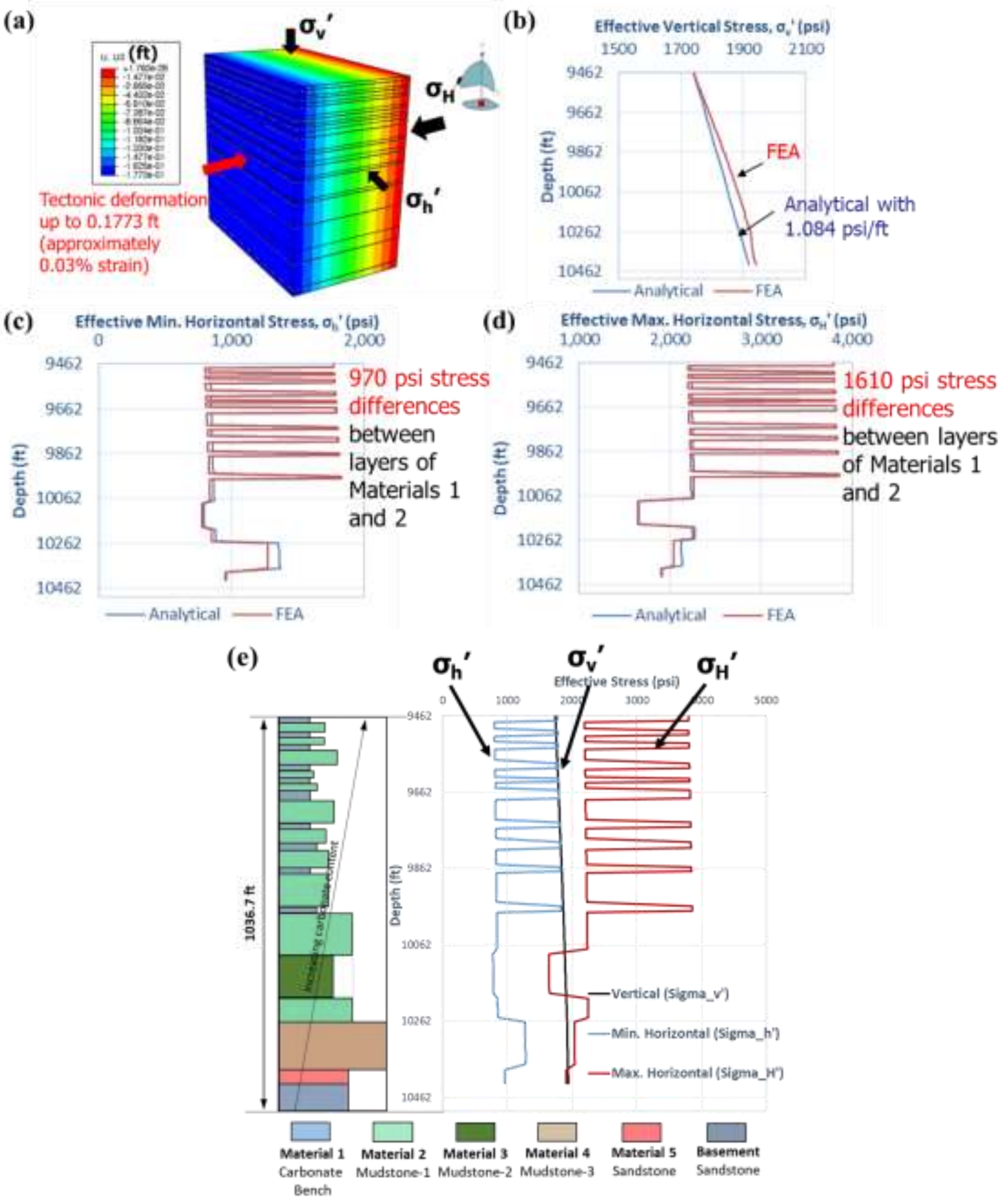

Figure 2.7 - Comparisons between analytical and FEA results of in-situ stresses resulting from gravity loading (under uniaxial-strain conditions) and subsequent lateral tectonic deformation: (a) In-situ stress development (effective vertical stress $\sigma_v{}'$, effective minimum horizontal stress $\sigma_h{}'$, and effective maximum horizontal stress $\sigma_H{}'$) under tectonic deformation; (b) Effective vertical stress; (c) Effective minimum horizontal stress; (d) Effective maximum horizontal stress; (e) Comparison among the three stresses in FEA.

Figures 2.7-c and 2.7-d show the large variability in horizontal stress between layers. The difference in the minimum horizontal stress between adjacent layers (Materials 1 and 2) is 970 psi, and the corresponding difference in the maximum horizontal stress is 1610 psi. It is anticipated that the large stress contrast between adjacent layers may result in differential deformation and slip failure at the surfaces of a drilled wellbore or at the surfaces of a created hydraulic fracture, when these are supported open by a uniform pressure. Figure 2.7-e shows the minimum, intermediate and maximum effective in-situ stress as a function of depth, alongside the stratigraphic vertical sequence of the system. A dominant strike-slip faulting regime is observed along the entire vertical section. The maximum effective horizontal stress is considerably higher than the vertical stress, and the minimum horizontal stress. Furthermore, within the stiff carbonate layers, the vertical stress and the minimum horizontal stress are approximately identical. In contrast, within the organic rich mudstones, the minimum horizontal stress is smaller than the vertical stress. For the calcareous mudstone (Material 3) the vertical stress is the largest stress, and along this region the in-situ stress represents a regime of normal-faulting. The presence of rock layering and the contrast in elastic properties between layers gives rise to complex stress distributions and localized changes in stress faulting regimes. In addition, the time-dependent properties of the layers (e.g., creep) further control the final magnitudes of the stress differences and the stress profile. Thus, simplified models that ignore rock layering and their properties will not provide realistic assessments of the in-situ stress.

2.3.4 Development of Shear Stress

In this section, we compare the development of shear stress and shear slip between the laterally-homogeneous and laterally-heterogeneous models, during in-situ stress loading. We would like to observe if layer heterogeneity results in the development of shear stresses. Figures 2.8-a and 2.8-b show results from the laterally-homogeneous model. There is no development of shear stresses along bed parallel and bed-perpendicular planes in this model. Figures 2.9-a and 2.9-b show the frictional shear stresses along a significantly weak interface defined between an organic rich mudstone (Material 2) and a carbonate layer (Material 1). Outputs CSHEAR1 and CSHEAR2 from ABAQUS are shown for the frictional shear stresses in the x and z directions, respectively. These results are in line with the theory (i.e., principal planes are devoid of shear stresses) and shear stresses are found to be negligibly small 1.24E-9 psi to 2.59E-9 psi.

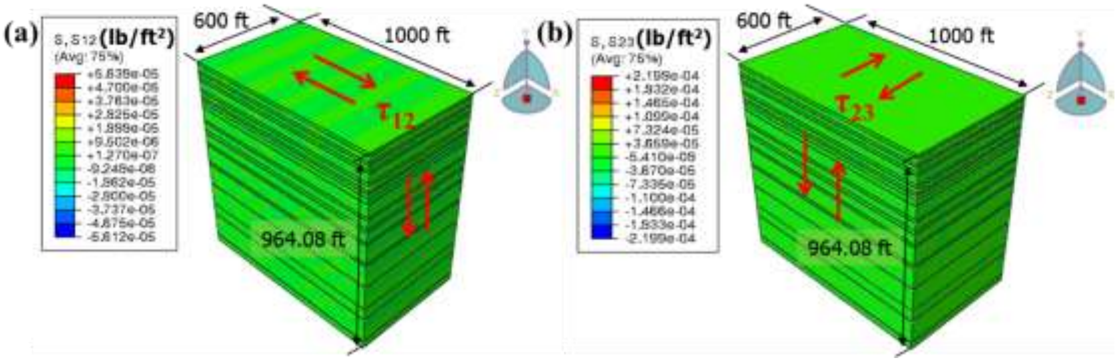

Figure 2.8 - Shear stress distributions in laterally-homogeneous rocks: (a) τ_{12} in x-y plane; (b) τ_{23} in y-z plane.

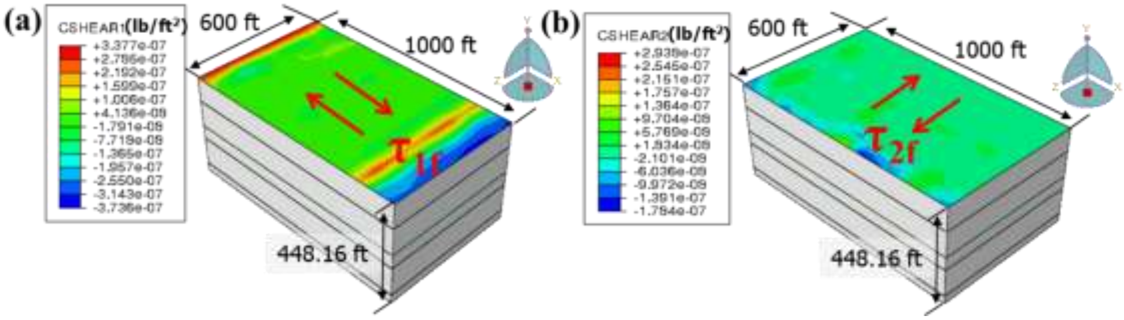

Figure 2.9 - Frictional shear stress distributions at the weak interface (see Figure 2.5) in laterally-homogeneous rocks: (a) Frictional shear stress τ_{1f} in principal direction 1 (x direction); (b) Frictional shear stress τ_{2f} in principal direction 2 (z direction).

Figures 2.10-a and 2.10-b show the corresponding results for the laterally-heterogeneous model, and Figures 2.10-c and 2.10-d show those for the strongly laterally-heterogeneous model. Results show the distinct development of shear stresses with values that vary locally. Shear stress values, τ_{12} in x-y plane and τ_{23} in y-z plane, in the range of approximately ±200 psi and ±360 psi, were observed. The lateral tectonic deformation (along the z-direction) causes a shear stress, τ_{23}, in y-z plane that is approximately 1.8 times higher than τ_{12} in x-y plane. In addition, the shear stress development increases with the degree of heterogeneity and is 2.5 to 3 times greater for the strongly laterally-heterogeneous model. When similar geological definitions and properties are assumed, however, different in-situ stress loading may cause different stress developments. Therefore, geologic history is a very important factor on the following geological events and the resulting stress and strain developments.

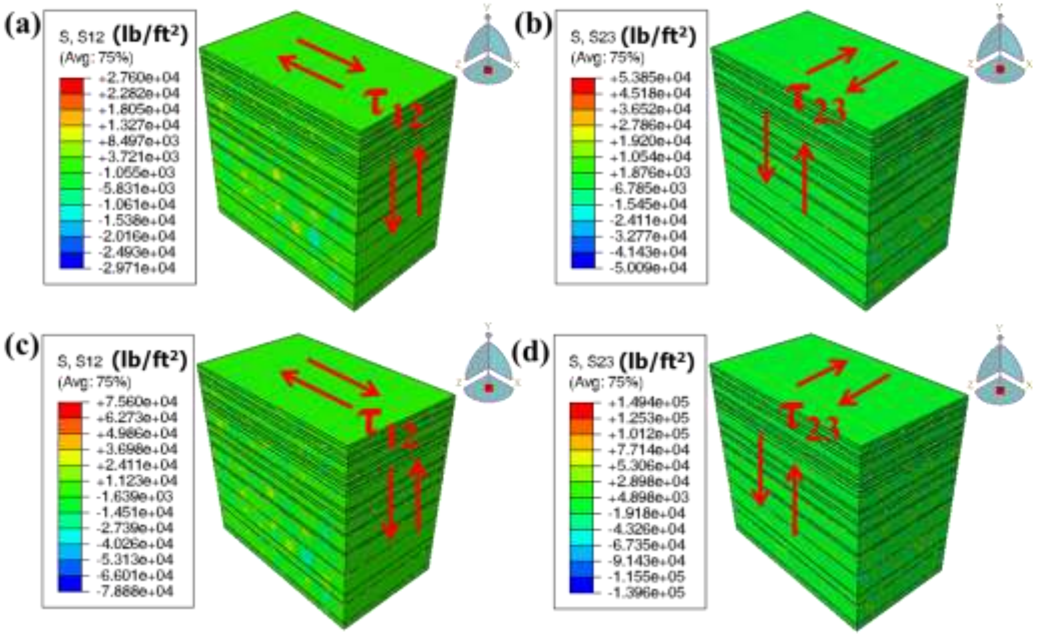

Figure 2.10 - Comparisons of shear stress development in laterally-heterogeneous rocks with randomly varied material properties (the model size is same as that in Figure 2.8): (a and b) τ_{12} in x-y plane and τ_{23} in y-z plane with the range of ±20%; (c and d) τ_{12} in x-y plane and τ_{23} in y-z plane with the range of ±50%.

Figures 2.11-a and 2.11-b show the frictional shear stress distributions within the significant weak interface defined in Figure 2.5. Frictional shear stresses in the x direction and z direction, are in the range of approximately ±3.5 psi and ±9.4 psi, respectively. These same values are higher (and ranging approximately ±10.2 psi and ±27 psi) for the strongly laterally-heterogeneous model. Localized shear slip was not observed, for this degree of material heterogeneity, but the resulting increase in shear stress with the magnitude of the of heterogeneity did increase the risk for shear slip at the weak interface.

As evidenced by the standard homogeneous layers model in Figure 2.9, given the configuration of the layered media with loading parallel and perpendicular to the layers, the bedding interfaces between layers are principal planes and there is no potential for shear generation. However, as different degrees of heterogeneity are introduced, the above principle is again satisfied in an average sense, across the entire interface, but locally things change. Thus the local development of shear can be observed. For equilibrium, the integration of all the shear across the entire surface should be zero. The entire surface will never slip, however, at the local level, the magnitude of the shear changes. In addition, the magnitude and localization of the shear stress depend on the strength and scale of the heterogeneity imposed in the model.

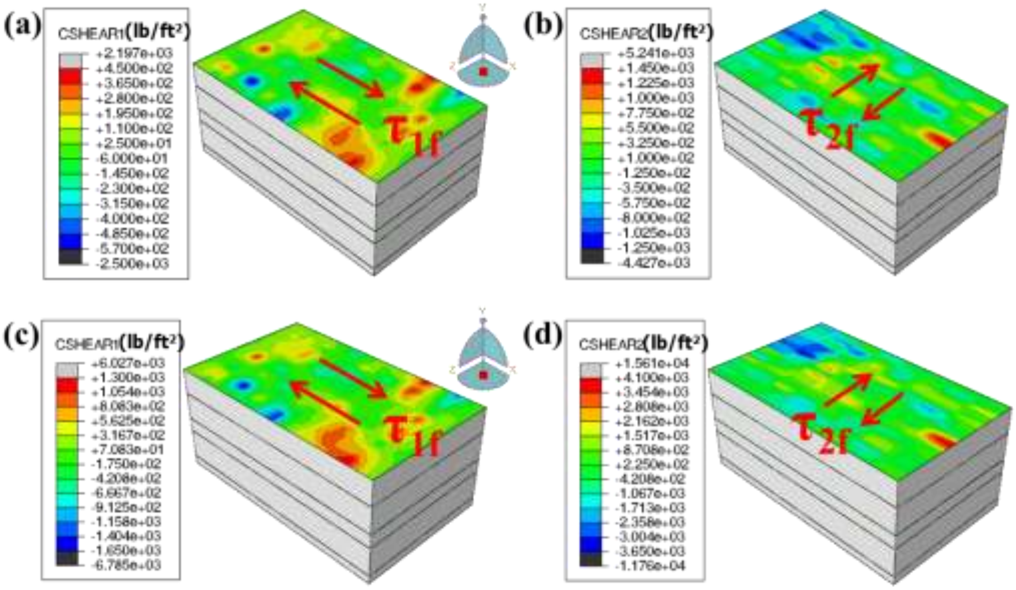

Figure 2.11 - Comparisons of frictional shear stress distributions at the weak interface (see Figure 2.5) in laterally-heterogeneous rocks with randomly varied material properties (the model size is same as that in Figure 2.9): (a and b) Frictional stresses in x direction (τ_{1f}) and in z direction (τ_{2f}) with the range of ±20%; (c and d) Frictional stresses in x direction (τ_{1f}) and in z direction (τ_{2f}) with the range of ±50%.

2.3.5 Wellbore Stability and Shear Stress Development Along Wellbore

When internal boundaries (e.g., wellbores or fractures) are created in the stressed model, as described previously, and these are subjected to uniform pressures across layers (e.g., drilling mud pressure or fracturing fluid pressure), one anticipates shear displacement at the interface between layers and potential slip failure. To evaluate this potential a 6-inch diameter vertical wellbore was located at 250 ft from the edge of the model and centered long the width of the model (Figure 2.12).

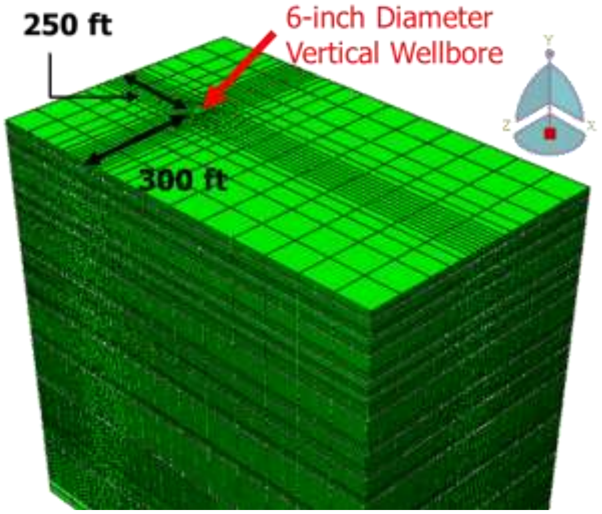

Figure 2.12 - Vertical well location. To obtain a reliable result for stress concentration along the wellbore, the meshes should be fine enough in the vicinity of the wellbore in the model.

The hoop stresses at the wellbore face were calculated based on Eqs. (2.9) and (2.10) (in the plane of transverse isotropy). Figure 2.13 compares the maximum hoop stresses, as a function of depth, provided by the analytical solution and the numerical model. The analytical (dark red) and numerical (blue) solutions for the laterally-homogeneous model show generally a good agreement but there are still small difference between them. The difference corresponds to that between the effective horizontal stress distributions from the analytic- and the numeric-model results, in Figures 2.7-c and 2.7-d. The analytical hoop stress for the mudstones is lower than the FEA hoop stress, and for the carbonates, the opposite is the case. This is also an effect of the interfaces and their properties. The difference between the laterally-homogeneous and laterally-heterogeneous cases is also of interest. Results indicate that increasing the lateral-heterogeneity of the model increases the hoop stress difference across the interfaces, and makes these more prone to failure.

These results are also compared against the yield stress and the peak stress for the individual layers, to evaluate the potential development of wellbore failure and wellbore breakouts. Results show that the wellbore is stable. That is, the developed maximum tangential stress is, at all depths, lower than the rock yield strength.

Although a sable wellbore is anticipated with the lower maximum tangential stress than the rock yield strength of each layer, in this study, a stronger lateral-heterogeneity of rocks with smaller yield strengths may cause wellbore failure under the given loading condition of the model. The presence of rock layering and the contrast in elastic properties between layers cause complex maximum hoop stress distributions with depth. In addition, the introduced lateral-heterogeneity of rock increases the variance of the stresses across the interfaces, increasing the potential for wellbore failure. Thus, rock layering with contrasting properties between layers and laterally-heterogeneous rocks will be required to realistic assessments of wellbore stability.

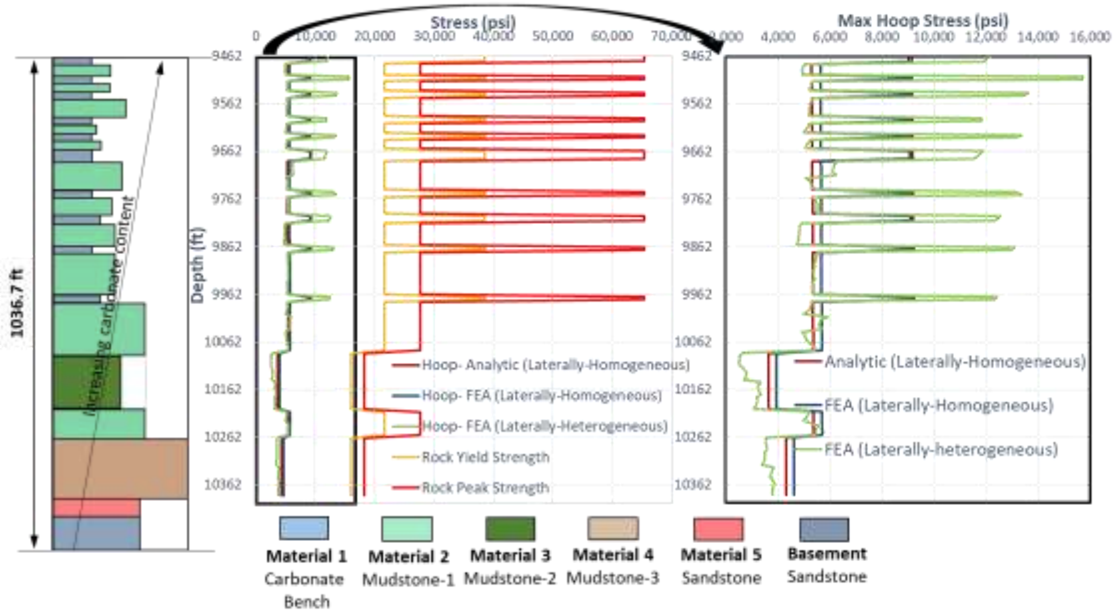

Figure 2.13 - Maximum hoop stress distribution along wellbore. The maximum hoop stresses obtained from the analytical and numerical solutions are compared with the yield strength and peak strength of each layer. The graph in the black box shows the comparison between the analytical and numerical solutions in both the laterally-homogeneous and the laterally-heterogeneous models.

Figures 2.14-a through 2.14-c show the distribution of the τ_{12} shear stress along the wellbore walls for the laterally-homogeneous and laterally-heterogeneous models. This corresponds to shear stresses along the xy plane. Figure 2.14-a shows the shear distribution in the laterally-homogeneous model. For this case, the shear stress is negligible within the xy plane except at the wellbore, where it localized and can be as high as 20 psi. The detail in Figure 2.14-a shows the significant wellbore shear that occurs in the region adjacent to the weak interface. Figure 2.14-b shows the corresponding development of shear for the laterally-heterogeneous case. Here one observes localized higher shear stresses along the body of the model and the wellbore. Figure 2.14-c compares the shear stress developed at the wellbore between the laterally-homogeneous and laterally-heterogeneous models.

From these results, it is seen that in the laterally-homogeneous model, the shear development is localized along the interfaces between layers. In the laterally-heterogeneous model, the development of shear is also controlled by the heterogeneous distribution of elastic properties within each layer, and thus is less localized along the interfaces. The magnitude of the shear stress, however, is comparable.

As shown in Figure 2.8, no shear stress developed in the laterally-homogeneous model without a wellbore. However, as a vertical well exists in the model, the wellbore acts as boundaries with potential shear displacements along each interface. However, shear displacement is restricted by the supporting rock around the circumference of the borehole and therefore shear stresses develop around the wellbore. If different degrees of heterogeneity are introduced to the model with a wellbore, the interfaces near the wellbore are not the only interfaces that develop shear stresses as shown in Figures 2.10-a to 2.10-d. Shear stresses can be developed in the laterally-heterogeneous model. Thus, the potential for shear stresses to develop in the system, including at the wellbore walls, may decrease or increase depending on the magnitude of the lateral heterogeneity in material properties.

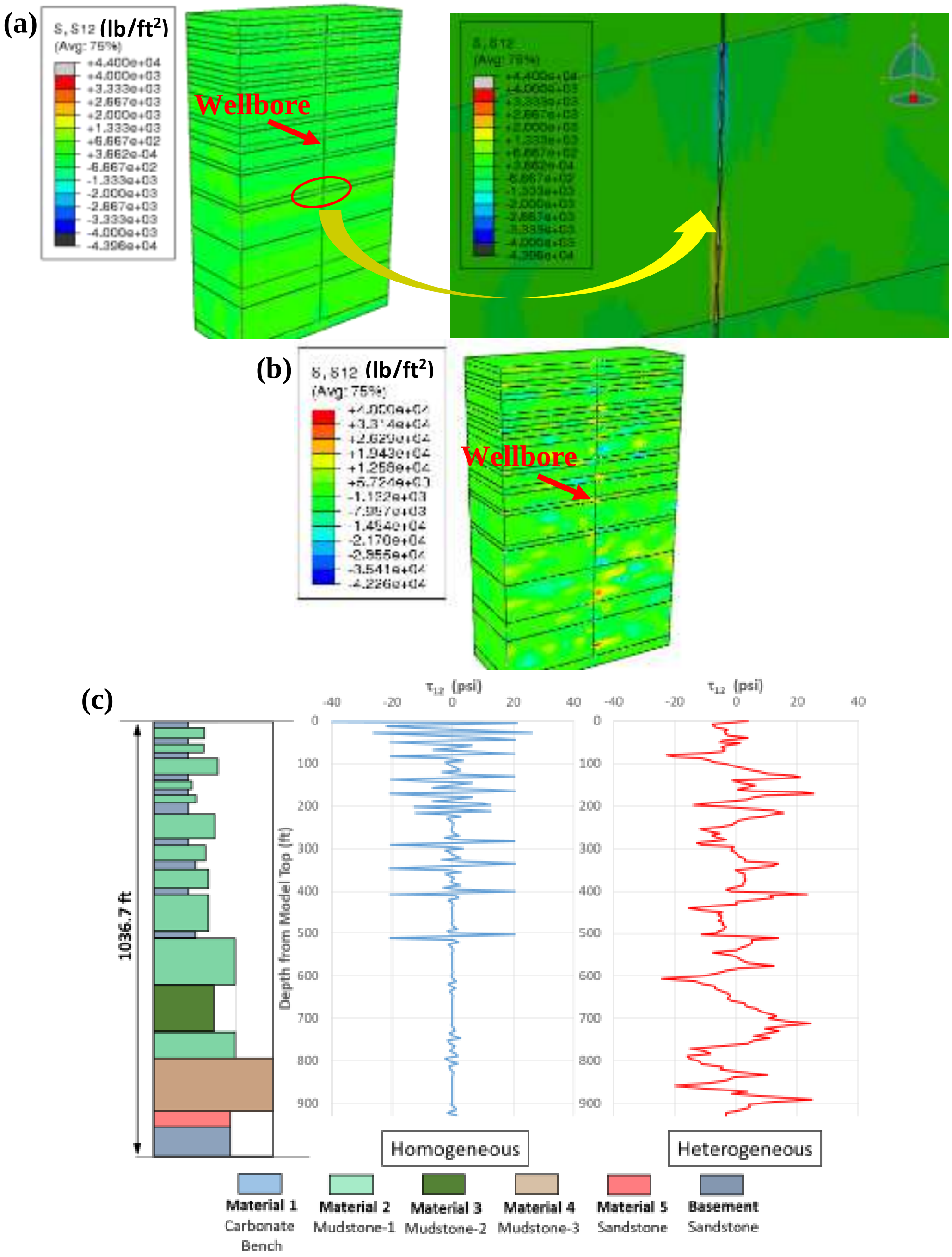

Figure 2.14 - (a) τ_{12} distribution in laterally-homogeneous rocks; (b) τ_{12} distribution in laterally-heterogeneous rocks with the range of ±20%; (c) Comparison between τ_{12} distributions along wellbore in laterally-homogeneous rocks and heterogeneous rocks with the range of ±20%.

2.3.6 Shear Slip along Weak Interfaces During Hydraulic Fracturing

When a hydraulic fracture is created in a layered media with large stress contrast between layers, and these layers become supported by a more uniform (fracturing) fluid pressure, relative shear displacement at the interfaces between layers is anticipated. In addition, the near-fracture failure may promote seepage of fluid to the interfaces and subsequent pressurization. This reduces the normal stress (contact pressure) at the interface and increases the potential for shear slip. To evaluate this effect, a vertical fracture was included in the model at the central location along the width of the model (Figure 2.15-a). The model does not represent the hydraulic fracture propagation as a function of pressure but simulates the effect of the fracture, after it has been propagated, as uniform pressure boundary condition to an internal surface (y-z) in the model. The model represent neither the presence of hydraulic fluids nor their potential seepage into weak interfaces between layers. However, it represents the mechanical effect of loading the heterogeneous system with uniform loading and allows us to investigate the potential generation of localized shear resulting from this, for a given realization of heterogeneity within the layers.

Figure 2.15-a shows hydraulic fracture created in the strongly laterally-heterogeneous model. The net pressure that develops during hydraulic fracturing, which is the difference between the treatment pressure and the minimum stress, typically varies in the range of 200 psi to 800 psi, with few exceptions. In the present model, the stresses vary from layer to layer, and thus we used a uniform pressure of 400 psi above the effective vertical stress (2250 psi). This choice reflects the small differences between the

vertical and minimum horizontal stress within the stiff layers (Figure 2.7). The fracture length and height are modeled as 600 ft and 445.3 ft, respectively. Figure 2.15-b exposes the surface along which the uniform pressure was applied to simulate the presence of a hydraulic fracture (red arrows) and the resulting deformations induced by the uniform pressure (blue to red). The largest deformation (0.103 ft) develops in the lower Young modulus calcareous mudstone (Material 3). The stiffer carbonate layers deform considerably less, in proportion to their higher Young Moduli. We are particularly interested in Interfaces 1 and 2, which represent weak interfaces at the contacts between the carbonate benches and the organic-rich mudstones (Figure 2.15-b). Figures 2.15-c and 2.15d show the frictional shear stress distributions (CSHEAR1 in lbs per square foot) within these surfaces. Results show the development of 45 psi of shear stress on Interface 1 (green region) and 110 psi on Interface 2 (dark green region). The extent of the region with increased shear stress varies from 125 ft to 250 ft from the fracture face.

Given the conditions of the model (parallel and horizontal planes of weakness, aligned with the in-situ stress), hydraulic fracturing alone does not elevate the shear to its critical value for failure. The weak interfaces need to be critically stressed for triggering failure. However, we anticipate that if the treatment pressures, during fracturing, are similar or higher than the vertical stress, seepage of hydraulic fracturing will be initiated by the development of shear in the neighborhood of the fracture face, and promoted further by the pressurization of these, as the fluid moves into the interface, increasing the potential for shear failure.

Given the conditions of the model at the faces of a hydraulic fracture, and at the interfaces between layers, shear stresses develop further beyond the effect of heterogeneous nature of rocks because the planes of weakness are pressurized during hydraulic fracturing. The magnitude of these depend on the contrast between the layer properties, the degree of heterogeneity and the magnitude of the pressurization. Given the low effective vertical stress, fluid penetration will be possible and, if the interfaces are very weak, they may fail.

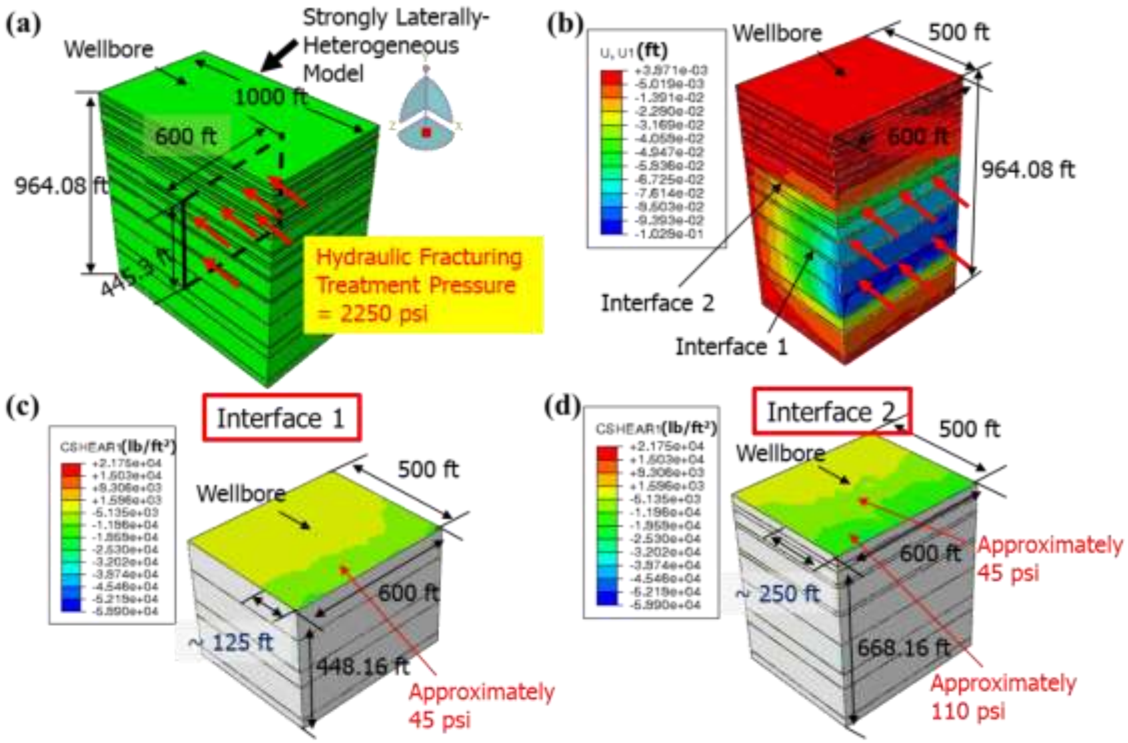

Figure 2.15 - (a) Hydraulic fracturing treatment; (b) Lateral deformations induced by hydraulic fracturing; (c and d) Frictional shear stresses in x direction at interfaces 1 and 2 indicated in (b).

2.4 Conclusions

Numerical (Finite Element Analysis) simulations were conducted on layered and discontinuous rocks, representative of organic-rich mudstones and carbonate sequences, which are typically found in unconventional reservoirs. This study, part of a broader field study, set out to investigate the consequences of rock layering with contrasting mechanical properties and non-welded interfaces, on shear stress development at interfaces between rock layers (which are bed parallel and sub-horizontal), during in-situ stress loading, well construction, and hydraulic fracturing. For these investigations, we simulated, using known field formation properties, three cases of laterally-homogeneous, laterally-heterogeneous, and strongly laterally-heterogeneous layered rocks with weak interfaces between layers.

The model's results show that shear stresses do not develop in the laterally-homogeneous model during in-situ stress loading, which includes gravity loading, under conditions of uniaxial-strain boundaries, followed by tectonic shortening. However, a small and localized shear development is observed in the laterally-heterogeneous modes, and the magnitude of the shear stress development is proportional to the magnitude and distribution of the imposed material-heterogeneity (i.e., the contrast and distribution in the elastic properties).

This study has identified that the interfaces and their properties influence the difference between the analytic- and the numeric-model results. This is true for both effective horizontal stress distribution with depth and hoop stress distribution at the vertical wellbore walls. The analytical model assumes fully decoupled layers in relation to their assigned interface properties while the FEA model assumes coupled layers.

Under in-situ stress loading, the presence of rock layering and the contrast in elastic properties between layers cause the large stress contrast between adjacent layers and localized changes in stress faulting regimes. In the case of a vertical well, shear stresses and complex hoop stresses develop along the borehole walls in the laterally-homogeneous model. Introducing lateral-heterogeneity into the rock increases the difference in the hoop stresses across the interfaces, resulting in the increased potential for wellbore failure, while the shear development will be affected by the combined result of layered heterogeneity and lateral heterogeneity at the wellbore walls, and can increase or decrease, accordingly.

Under uniform pressure loading, along a large area that simulates a hydraulic fracture being created, we observe a measurable shear stress development, along the bed-parallel direction, that propagates a significant distance into the reservoir (125 to 250 ft). However this is insufficient to level required for shear failure. Results indicate that the weak interfaces need to be critically stressed for shear failure to take place. The model does not evaluate fluid seepage into the weak interfaces, but we propose that if the treatment pressures are similar or higher than the vertical stress, which is common in overpressured unconventional reservoirs, seepage of hydraulic fracturing fluid will be initiated by the near-wellbore shear at the weak interfaces, and promoted further by the fluid penetration and pressurization of these interfaces, increasing the potential for shear failure.

The simulations we conducted show that strong heterogeneity and strong structural components are needed to develop sufficient shear for shear failure along the interfaces between rock layers. The economic consequences of shear slip along weak interfaces are associated to the reduced vertical extent of hydraulic fracture growth, the reduced well production, and the increased risk for well failure conditions. Therefore, for developing adequate mitigation strategies for these problems, it is very important to understand the sources of shear, and consequently, the layered and heterogeneous nature of the reservoir. Future efforts will aim to quantify the effect of hydraulic fluids and fluid seepage to the interfaces on shear slip along the weak interfaces. Future efforts will also be aimed at various case studies with inclined and discontinuous interfaces in actual field, for the potential shear failure.

3. EFFECT OF ROCK LAYERS AND WEAK INTERFACES ON HYDRAULIC FRACTURE HEIGHT GROWTH[*]

3.1 Introduction

Hydraulic fracturing (HF) treatments have been widely used to enhance oil and gas production (Economides and Nolte, 2000; Holditch, 2006). Improving the representation of these treatments with more adequate numerical modeling is important because it helps to increase the created fracture surface area, to reduce completion costs, and to improve well production. When considering more complex reservoirs, such as shale and mudstone, numerical simulation of the hydraulic fracture treatments is considerably more challenging because of the layered nature of the rock and the impact of the associated interfaces of contact between layers, inhomogeneity, and pre-existing natural fractures on hydraulic fracture growth.

Conventional methods for numerical modeling of hydraulic fractures were developed for homogeneous and elastic rocks. These generally do not provide adequate solutions for inhomogeneous, layered rocks, which are built with stiff and compliant layer couplets that can exhibit strongly contrasting elastic properties. In addition, the interfaces between these layers introduce displacement discontinuities and localized aperture-dependent fluid seepage.

---

[*] Reprinted with permission form "Finite-Element Simulations of Hydraulic Fracture Height Growth on Layered Mudstones with Weak Interfaces" by Rho, S., Noynaert, S., Bunger, A. P., Zolfaghari, N., Xing, P., Abell, B., and Suarez-Rivera, R., 2017, 51st US Rock Mechanics/Geomechanics Symposium. Copyright 2017 by Aemrcial Rock Mechanics Association (ARMA).

Whether considering a homogeneous stiff medium or otherwise, hydraulic fracture simulators inevitably must deal with challenges arising from the stress singularity that mathematically occurs at the fracture tip in the context of classical linear elastic fracture mechanics (LEFM, Rice and Rosengren, 1968; Sinclair, 1996). To resolve these problems using finite element analysis (FEA), the cohesive zone model (CZM) was introduced and developed (Barenblatt, 1959; Barenblatt, 1962; Dugdale, 1960; Mokryakov, 2011; Lecampion, 2012; Chen et al., 2009; Sarris and Papanastasiou, 2011; Sarris and Papanastasiou, 2012; Carrier and Granet, 2012; Yao, 2012; Yao et al., 2015; Haddad and Sepehrnoori, 2015). Using CZM, the problem of developing mathematical singularities by having zero fracture opening at the crack tip is avoided by assuming the existence of fracture process zone that results in a finite fracture opening at the crack tip. In addition, in CZM simulations of fracture propagation, each time step of numerical computation may proceed without the need of remeshing the model.

The cohesive zone (CZ) concept was first introduced by Barenblatt (1959, 1962), and Dugdale (1960). Chen et al. (2009) investigated the cases of hydraulic fracture propagation of penny shaped fractures propagating in a toughness-dominated regime, and in an impermeable infinite, elastic medium using the pore-pressure-cohesive element method. Sarris and Papanastasiou (2011) studied the influence of the cohesive process zone in hydraulic fracture propagation under plane-strain conditions. They also examined the influence of formation permeability, injection rate, and formation compressibility on fracture geometry using the cohesive zone numerical approach (Sarris and Papanastasiou, 2012). Carrier and Granet (2012) developed a zero-thickness-finite element method, to model fracture propagation in a permeable poroelastic medium by a cohesive zone model. They also investigated the influence of the porous medium permeability and fluid viscosity on the fracture propagation using their zero-thickness cohesive elements. Yao (2012) developed a 3D pore-pressure-cohesive zone model, to investigate the effects of rock properties on fracture geometry and on the fracture process zone. This model considered fracturing in quasi-brittle/ductile rocks. Yao et al. (2015) predicted the nucleation and propagation of a penny-shaped, fluid-driven fracture, in sandstone using the 3D-pore-pressure-cohesive zone model. Haddad and Sepehrnoori (2015) modeled 3D single- and double-stage hydraulic fracturing, using a pore-pressure-cohesive-zone model. They conducted parametric studies on rock mechanical properties (Young's modulus and Poisson's ratio), pumping rate, fluid viscosity, and leakoff coefficient, in an attempt to define important controlling factors to hydraulic fracturing and reservoir stimulation.

More recently, using CZM, many of investigators have provided numerical solutions for HF/NF interaction. Chavez-Gonzalez et al. (2015b) investigated two dimensional HF/NF interaction behaviors using cohesive zone methods. They presented important parameters that affect the HF/NF interaction and its resulting geometry. Chen et al. (2017) investigated the interaction of a single HF intersecting a single NF, using a fully coupled 2D CZM. They evaluated the effect of various parameters on hydraulic fracture propagation. Nikam et al. (2016) introduced a three layered, three dimensional geomechanical model with a HF intersecting with pre-existing NF, using cohesive elements. They conducted a detailed sensitivity analysis evaluating the impact of in-situ stresses, injection rate, injection fluid and NF properties on HF propagation and its interaction with a NF. Haddad et al. (2017) proposed a novel 3D fracture-intersection model to quantify HF/NF interaction behaviors and fluid infiltration to NFs.

In this study, we are interested in modeling the interaction between hydraulic fractures with rock layers and weak interfaces during hydraulic fracturing from a horizontal wellbore. This study has been conducted on multiple layers (at least 30 layers) with interfaces between layers, which have not been previously investigated using numerical simulations. To accomplish this, we used the pore-pressure-cohesive-element method in ABAQUS FEA software. Although the cohesive element approach has a limitation on the fracture propagation along predefined fracture paths, it is able to numerically simulate the coupling between rock deformation, fracture propagation, viscous fluid flow within the fractures, and fluid seepage to the weak interfaces. Elasticity theory and lubrication theory are the main physical modeling frameworks used to simulate rock deformation and fluid flow, respectively. Constructing this model using the pore-pressure-cohesive elements is accompanied by a number of challenges, and this study discusses these challenges and their resolution in the modeling.

The work also includes a parametric study conducted to evaluate the relationship between the localized fluid loss controlled by the hydraulic conductivity (HC) of the weak interfaces and the classical, macro-scale measure of total fluid loss and fluid efficiency evaluated at the end of the treatment (i.e., fluid efficiency which is defined as the ratio of the created fracture volume to the total injected fluid volume). The results show a systematic decrease in fracture height and fluid efficiency with increasing values of interface hydraulic conductivity (for an invariant number of interfaces and interface locations). This relationship is important because of its potential impact on improving fracture diagnostics in the field. We also observe that the interface strength and fluid viscosity have a strong effect on fracture height growth as well as fluid efficiency. The current model has limitations to some extent because it is 2D, but the above findings are important to give great ideas for developing better predictions of well productivity as well as an improved assessment of fracture height growth and the created fracture surface area.

3.2 Basic Definitions and Theories

3.2.1 Cohesive Traction-Separation Relations

The damage initiation and the evolution of the cohesive zone are defined by a bilinear traction-separation failure criterion, as shown in Figure 3.1. The material behaves in a linear elastic manner with the resistive traction, at the boundaries of the cohesive-element, increasing linearly with opening displacement up to its critical damage initiation displacement δ_0 and up to its maximum tensile stress T_{max}. Subsequently, the resisting traction decreases linearly with increasing opening displacement beyond δ_0. Damage of the cohesive zone thus accumulates linearly, until the separation reaches its critical value at complete failure δ_f and the resisting traction is zero. The area under the traction-separation bilinear failure law is defined as the work required to create the fracture or the fracture energy G_c, which is associated to the rock fracture toughness K_{IC} by (Rice 1968; Kanninen and Popelar 1985):

$$G_c = \frac{K_{IC}^2(1-\nu^2)}{E} \tag{3.1}$$

where E is Young's modulus and v is Poisson's ratio. To construct the traction separation law, one defines T_{max} and G_c from the known rock properties, then δ_f is calculated based on the known area (G_c) under the failure envelope. To estimate δ_0, a ratio α is introduced as δ_0/δ_f, which is defined as the critical separation ratio. Based on a value of α, δ_0 is evaluated, and knowing T_{max}, the slope representing the elastic behavior of the element is defined. The latter is defined as the cohesive stiffness K of the element, which can be expressed as the elastic modulus of the cohesive element per unit length. Using all the parameters introduced above, G_c is rewritten as

$$G_c = \frac{1}{2}T_{max}\delta_f = \frac{1}{2\alpha}T_{max}\delta_0 = \frac{T_{max}^2}{2\alpha K} \tag{3.2}$$

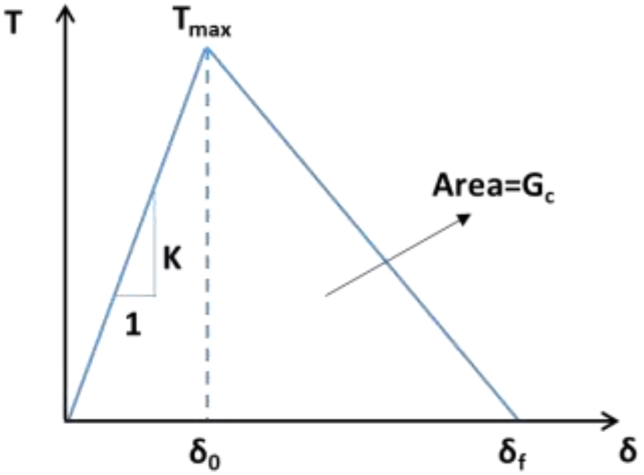

Figure 3.1 - Typical bilinear traction-separation law for the cohesive element.

Figure 3.2 illustrates the mechanism of hydraulic fracturing with a finite-sized cohesive zone, which is separated into unbroken and broken cohesive-zone regions. The unbroken cohesive zone represents the region immediately adjacent to the fracture tip and is called the fracture process zone. The traction-separation law is still valid with nonzero surface tractions at the boundary of the fracture process zone. The broken cohesive zone represents the open fracture at some distance from the fracture tip. Once the cohesive zone is completely broken and the fracture is filled with fluid, the traction-separation law no longer applies, and the separation is controlled by the fracturing fluid pressure acting on the fracture surfaces as coupled to the deformation of the adjacent rock.

Currently, there is no standard method for identifying the fracture tip location, but there are three specific locations that can be identified from the traction-separation failure envelope: 1) the first location is defined when the element separation is just about to be initiated (δ=0); 2) the second location corresponds to the point where the resisting traction reaches the cohesive strength T_{max} ($\delta = \delta_0$); and 3) the last location corresponds to the point when the resisting traction is zero ($\delta = \delta_f$) (Shet and Chandra, 2002). Figure 3.2 shows the relationship between the mathematical crack tip, which gives rise to singularities, and the alternative representation by the cohesive crack tip ($\delta = \delta_0$) and the material crack tip ($\delta = \delta_f$), which are defined within the unbroken cohesive zone (Shet and Chandra, 2002). The cohesive crack tip is generally considered as the front of the fracturing fluid and the boundary to which this can permeate into the damaged cohesive zone ($\delta_0 \leq \delta \leq \delta_f$).

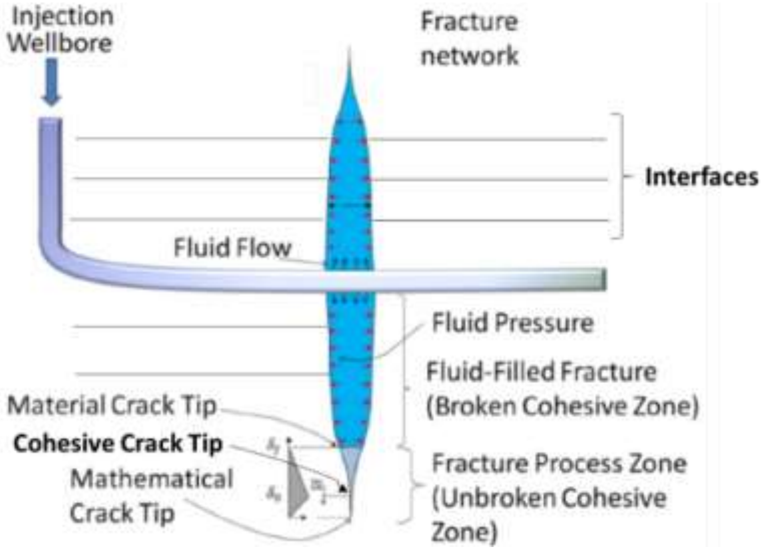

Figure 3.2 - Schematic diagram of cohesive zone in hydraulic fracturing (modified from Gonzalez et al., 2015a).

3.2.2 Tangential Permeability and Hydraulic Conductivity within the Cohesive Zone

A schematic fluid flow diagram within the fracture and near the fracture tip is shown in Figure 3.3. Two types of flow are highlighted in the figure: tangential flow and normal flow. The normal flow is not considered in this model because the fluid leakoff into the porous medium is negligibly small in nano-Darcy rock and is ignored in this study.

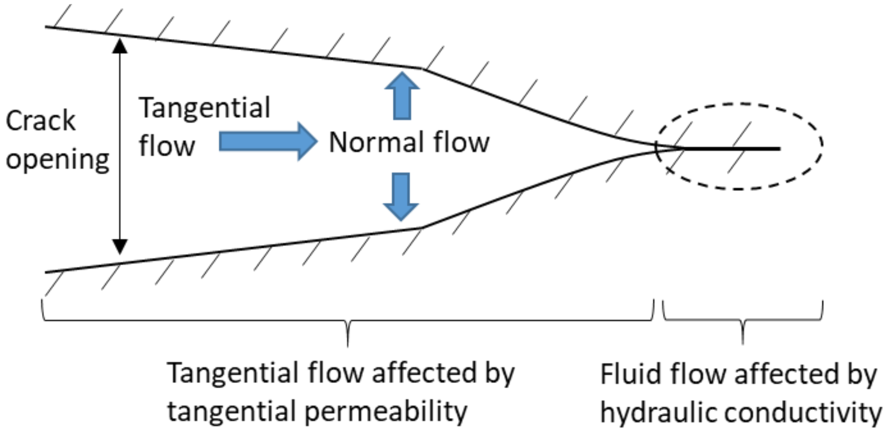

Figure 3.3 - Definitions of flow-related quantities in a hydraulic fracture with a cohesive zone.

Following the constraints of the lubrication theory, the hydraulic fracturing fluid is assumed to be an incompressible, Newtonian fluid. The requirement for conservation of mass in 1D flow (Boone and Ingraffea, 1990) is given by the 1D continuity equation, as follows:

$$\frac{dq}{dx} - \frac{dw}{dt} + q_l = 0 \tag{3.3}$$

where q is the local flow rate per unit height, along the fracture in direction x, q_l is the local fluid loss to the permeable rock (this was assumed zero in this study), and w is the fracture opening. The requirement of conservation of momentum is given by the lubrication equation, the Poiseuille's law, as follows:

$$q = uw = -\frac{w^3 dp}{12\mu dx} \tag{3.4}$$

where p is the fluid pressure, u is the average velocity of the fluid over the cross-section of the fracture, and μ is the dynamic viscosity of the fluid. Therefore we can write the fluid flow as

$$q = -k_t \frac{dp}{dx} \tag{3.5}$$

where k_t is the tangential permeability, dp/dx is the rate of pressure change in the direction of the crack. One challenge in the simulations is that for cohesive elements in ABAQUS, there are three different quantities that need to be defined properly in order to obtain the correct value of the fracture opening. The opening is found with $d = t_{curr} - t_{orig} + g_{init}$, where the three contributing quantities are:

1) t_{orig}, which is the initial thickness of the crack,
2) t_{curr}, which is the current thickness of the crack,
3) g_{init} is a small, non-physical initial opening that is defined to avoid numerical difficulties for deriving fluid flow when the opening is zero.

Hence, ABAQUS uses $\hat{d} = t_{curr} - t_{orig}$ as the opening in Poiseuille's law, so $w = \hat{d}$ or aperture, and the assumed value for g_{init} is 0.0001 m, which is used only for the first element close to the inlet in this study. Combining Eq. (3.4) and Eq. (3.5), the tangential permeability k_t is obtained as

$$k_t = \frac{\hat{d}^3}{12\mu} \tag{3.6}$$

The tangential permeability is thus defined by the resistance to fluid flow between two smooth parallel walls that are separated by an aperture ($\hat{d}$) and by the viscosity (μ) of the fracturing fluid. Within the broken cohesive zone, once the cohesive-elements are opened, the tangential permeability governs the coupling between fluid flow and fracture propagation, following the cubic law relationship to the fracture aperture, as shown in Eq. (3.6). However, within the unbroken cohesive zone, before the cohesive-elements are totally opened, fluid flow is governed by Darcy law as

$$q = -\frac{K\hat{d}}{\mathrm{\rho g}}\frac{dp}{dx} \tag{3.7}$$

where K is the hydraulic conductivity and is defined as

$$K = \kappa\frac{\rho g}{\mu} \tag{3.8}$$

Here κ is the intrinsic permeability, ρ and μ are the fluid density and viscosity, respectively, and g is the gravitational acceleration. The hydraulic conductivity is defined by Eq. (3.8) but also applied identically to Eq. (3.6) with a constant prescribed opening allowing fluid to move into the unbroken cohesive-zone, building pressure, and thus promoting opening and failure of the cohesive-zone. The same concept of cohesive-element behavior is used for the numerical representation of the hydraulic fracture and the weak interfaces between rock layers. The difference between the two resides in the properties assigned to their elements.

3.2.3 Analytical Solution for KGD Model

In this study, the numerical model was validated by benchmarking against Adachi’s solution (Adachi, 2001) for the Khristinaovic-Geertsma-de Klerk (KGD) model (Geertsma and de Klerk, 1969). The KGD model is a 2D plane-strain model based on linear elastic fracture mechanics (LEFM).

Assuming no leakoff into the porous medium, the solution of the plane strain KGD hydraulic fracture in an infinite elastic body is a function of the injection rate Q_0, and the three material parameters E', K', and μ', which are identified by

$$E' = \frac{E}{1-\nu^2}, \qquad K' = \left(\frac{32}{\pi}\right)^{1/2} K_{IC}, \qquad \mu' = 12\mu \tag{3.9}$$

where E' is the plane strain elastic modulus, and K' and μ' are simply introduced to tidy up the governing equations. E', K', and μ' simply mean elastic modulus, toughness, and fluid viscosity, respectively.

In Adachi's solution for the KGD model, the fracture opening *w(x,t),* the fracture half-length *l(t),* and the net fluid pressure *p(x,t)* are calculated by (Adachi, 2001)

$$\begin{gathered} w(x,t) = \varepsilon(t)L(t)\Omega[\xi, P(t)] = \varepsilon(t)L(t)\gamma[P(t)]\bar{\Omega}(\xi) \\ p(x,t) = \ \varepsilon(t)E'\Pi[\xi, P(t)] \\ l(t) = \gamma[P(t)]L(t) \end{gathered} \tag{3.10}$$

where $\varepsilon(t)$ is a small dimensionless number; *L(t)* is the lengthscale of the fracture half-length; *P(t)* is the dimensionless evolution parameter; ξ is the scaled coordinate and given by $\xi = x/l(t)$ $(0 \le \xi \le 1)$; Ω, γ, and Π are the dimensionless fracture opening, length or radius, and net fluid pressure, respectively.

There are two types of propagation regime except for the leakoff-dominated regime: the viscosity-dominated and toughness-dominated regimes (Adachi, 2001). The propagation regime is defined as a regime in which one particular process accounts for most of the dissipated energy during fracture propagation, and therefore the viscosity-dominated and toughness-dominated regimes

These two propagation regimes require two scaling schemes: viscosity and toughness scaling, respectively. The detailed explanations for the scaling can be found in the corresponding literature (see Adachi, 2001), but the required equations for calculating Eq. (3.10) are presented in this dissertation. In the viscosity scaling (denoted by a subscript *m*), the dimensionless parameters ε and L can be written by

$$\varepsilon_m = \left(\frac{\mu'}{E't}\right)^{1/3}, \quad L_m = \left(\frac{E'Q_0^3t^4}{\mu'}\right)^{1/6} \tag{3.11}$$

where the subscript ‘m’ represents the use of the viscosity scaling

The evolution parameter *P(t)* corresponds to a dimensionless toughness κ_m, given by

$$\kappa_m = K'\left(\frac{1}{E'^3\mu'Q_0}\right)^{1/4} \tag{3.12}$$

In the toughness scaling (denoted by a subscript *k*), the scaling factors ε_k and L_k are expressed by

$$\varepsilon_k = \left(\frac{K'^4}{E'^4Q_0t}\right)^{1/3}, \quad L_k = \left(\frac{E'Q_0t}{K'}\right)^{2/3} \tag{3.13}$$

and the evolution parameter *P(t)* can be interpreted as a dimensionless viscosity M_k, given by

$$M_k = \mu'\left(\frac{E'^3Q_0}{K'^4}\right) \tag{3.14}$$

K-vertex solution in the toughness-scaling, corresponding to a case with M_k, = 0 (the limit of inviscid fluid), can be written in the following forms (Perkins and Kern, 1961; Garagash, 2006):

$$\gamma_{k0} = \frac{2}{\pi^{2/3}}, \quad \overline{\Omega}_{k0} = \pi^{1/3}\sqrt{1-\xi^2}, \quad \Pi_{k0} = \frac{\pi^{1/3}}{8} \tag{3.15}$$

where $\overline{\Omega}_{k0} = \Omega_{k0}/\gamma_{k0}$.

3.3 Finite Element Modeling

3.3.1 Model Implementation

Numerical simulations were carried out using pore-pressure-cohesive-elements in ABAQUS 2016. CPE4R elements (4-node plane-strain elements with reduced integration) were used for rock matrix defining the rock layers, and COD2D4P elements (two-dimensional pore-pressure-cohesive-elements (PPCE)) for the predefined main vertical fracture, and for the bed-parallel weak interfaces in the layered rock. The PPCEs are helpful in representing the mechanical interaction between the propagating fracture and the weak interfaces, as well as the partitioning of fluid flow between main fracture and the horizontal fracture offshoots. Therefore, they enable evaluating the crossing or no-crossing conditions of the hydraulic fracture growing through a sequence of weak interfaces, as well as the overall fluid loss to these interfaces during fracture propagation.

The schematic diagram shown in Figure 3.4 represents the geometry of the model with one exception that for the sake of presenting, all the PPCEs shown with a thickness, while in practice the PPCEs associated with the main, vertical hydraulic fracture have zero thickness. This is constructed to model the upper half of a hydraulic fracture generated from a set of perforations along a horizontal well. In the numerical model, the surfaces of rock elements and PPCEs are tied together so that the cohesive elements are surrounded by two layers of rock.

Assuming no far-field stress, the model is constructed with fixed boundaries at all surfaces except the bottom surface, which is constrained only in y-direction. In order to get more accurate results that follow real geometry, all the rock layers are made so as to be large relative to the fracture displacement. There are no tractions applied to the model, and the stresses are only developed passively at the fixed boundaries. Also, the opening of the interfaces must not reach the boundary of the model before the hydraulic fracturing process is completed, and therefore the total length of the model is much larger than its total height.

In practice, however, it is difficult to avoid the boundary effects of the bottom surface in this half model. The opening behavior of the first interface is affected by the model boundary unless the first interface is located sufficiently far away from the inlet – which is impractical to do. Thus, for analysis of the results, it is recommended to ignore the early time calculations when the propagating tip is still very close to the lower boundary.

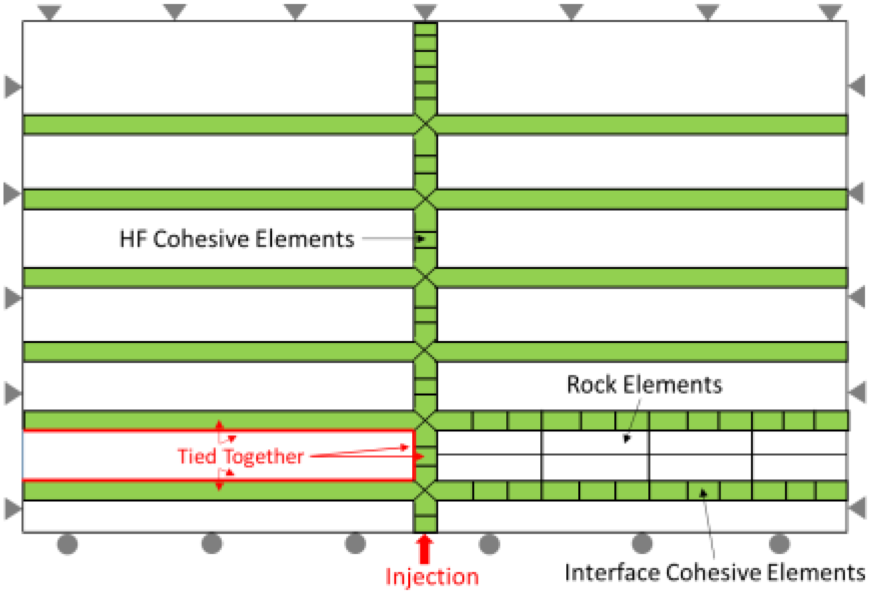

Figure 3.4 - Schematic diagram of multi-layered rocks with pore pressure cohesive elements. To better show the geometry, all cohesive elements have a thickness applied. However, the cohesive elements that represent hydraulic fracture have zero thickness.

Special attention is required at the intersection between the main, vertical hydraulic fracture and each interface between rock layers. The technique, illustrated in Figure 3.5, accounts for the interaction of these intersecting fractures by sharing the four pore-pressure-nodes of each hydraulic fracture element with the interface cohesive-elements at a node. This means that when the fluid pressure reaches the shared pore-pressure node, the other three elements will be set to that pressure and hence can potentially be a path for hydraulic fracture. At this point, we also recommend to break the bounding of the four elements and make them already open so that fluid can initiate in any favorable direction. Additionally, the main hydraulic fracture is modeled with zero-thickness cohesive elements in which the top and bottom nodes lay directly on each other. However, the interface nodes require special treatment to avoid interpenetration as the main hydraulic fracture approaches them. Hence, the interface CZ elements are given an initial thickness of 1 mm. This is sufficiently large compared to the hydraulic fracture width so as to minimize any distortion or pinching of interface CZ elements when main hydraulic fractures opens near the regions of intersection between the hydraulic fracture and the interface CZ elements.

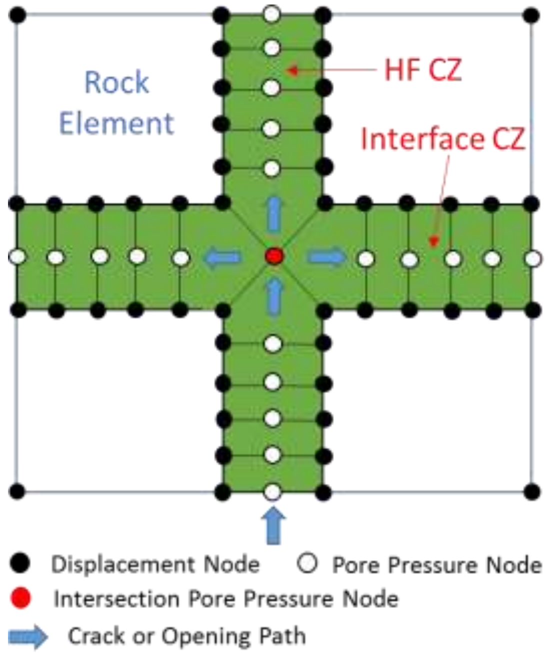

Figure 3.5 - Connection of cohesive elements at HF/interface intersections.

3.3.2 Input Parameters

Table 3.1 shows the mechanical properties (Young's modulus and Poisson's ratio) of the three rock types used in the model: soft, intermediate and hard. The values were estimated based on unconventional field data.

Table 3.1 - Rock Properties.

Rock	Young's Modulus (GPa)	Poisson's Ratio
Soft	20.7	0.2
Intermediate	30	0.25
Hard	41.4	0.3

Table 3.2 - Cohesive zone properties and injection rate.

Cohesive Zone		**HF**	**Interface**	**Notes**
Cohesive Strength, T_{max} (Pa)		1.E+06	5.E+04	T_{max} of interface CZ is 20 times less than that of HF CZ.
Cohesive Stiffness, K (Pa/m)		6.944E+11	1.563E+11	K of CZs is recommeded to be greater than that of rocks (about 30 times and 7 times greater than the minimum K of rocks for HF and interface CZs, respectively).
Fracture Energy, G_c (Pa*m)		36	4	G_c of Interface CZ is 9 times less than that of HF CZ.
Fracture Toughness, K_{IC} (Pa*m$^{0.5}$)	Soft Rock	8.81E+05	2.94E+05	K_{IC} is a function of G_c in T-S curve and E and ν of rocks.
	Intermediate Rock	1.07E+06	3.58E+05	
	Hard Rock	1.28E+06	4.27E+05	
Viscosity, μ (Pa*s)		0.0001		μ is negligibly small for benchmarking a toughness-dominated regime.
Hydraulic Conductivity, K (m/s)		0.001	0.1 ~ 1.5	K of HF CZ is negligibly small because of no fracture permeability in the initial zero-thickness elements. However, that of interface CZ is various depending on the interface intrinsic permeability with a constant μ.
Injection Rate (m^3/s/m)		0.001		It should be noted that the unit is m^3/s/m in the 2D model.

Crack opening within the PPCE is only related to the normal traction applied to the cohesive elements (tensile stress), and does not depend on the shear tractions in the directions parallel and perpendicular to the fracture. Thus, only the normal stresses are considered in the fracture propagation criteria, and shown in Table 3.2. The cohesive strength T_{max} and the fracture energy G_c of the bilinear fracture separation law for the cohesive elements in the hydraulic fracture are defined as 1 MPa and 36 Pa.m, respectively. The latter is calculated using Eq. (3.1). The cohesive stiffness K is calculated using Eq. (3.2). The elastic modulus of the cohesive elements is defined as the cohesive stiffness per the unit length ($E = K$*unit length) in ABAQUS.

For a homogeneous medium, or for a layered rock with welded interfaces, the elastic modulus of the HF-cohesive-elements is the same as that of the homogeneous rock or the rock layers. For a layered rock with non-welded interfaces, the elastic moduli of the HF-cohesive elements and the interface-cohesive elements should be larger than those of the rock layers. This assures that the two types of elements remain tied together. For interface opening and fluid loss along interfaces (we will simply call this “fluid loss” from now on), the cohesive strength and cohesive energy of the CZ-interface-elements should be very small compared to those of the CZ-HF elements because of the difficulties of the interface opening at the pumping rate used and under the fluid pressure within the fractures in this study. We used interface elements with cohesive strength (T_{max}) 20 times smaller (50 kPa) and a cohesive energy (G_c) 9 times smaller (4 Pa.s) than the CZ-HF elements. The strength of the interfaces is directly related to the cohesive strength and cohesive energy of the interface-CZ elements.

Note that we used a very small viscosity (0.0001 Pa.s) in these simulations. The purpose was to restrict consideration to cases in which viscous dissipation can be neglected (“toughness-dominated regime”). This is convenient for benchmarking and for limiting the relevant parametric space for these initial numerical experiments. A range of hydraulic conductivity between 0.1 m/s to 1 m/s is used to evaluate the sensitivity to fluid loss and to the resulting hydraulic fracture height growth. The injection rate used for all cases is 0.001 m^3/s/m. A summary of the relevant input parameters is given in Table 3.2.

3.3.3 Simulation Procedure

Finite element simulations for this hydraulic fracturing study are conducted in multiple steps. Figure 3.6 shows the flow diagram for the numerical simulation procedure. First, finite element model geometry, mesh size, and properties of both rock and cohesive elements as well as injection rate are defined in an Excel input file. In the next step, to create an ABAQUS input file, pre-built Matlab scripts are opened, and most conditions required in the numerical simulation are defined: initial gap opening in cohesive elements, boundary and loading conditions, total computational time, time increment sizes, maximum number of iteration, etc. Once the ABAQUS input file (*.inp) is created, it is run in ABAQUS/Standard. The results are plotted directly in ABAQUS/CAE or calibrated being plotted in different sources.

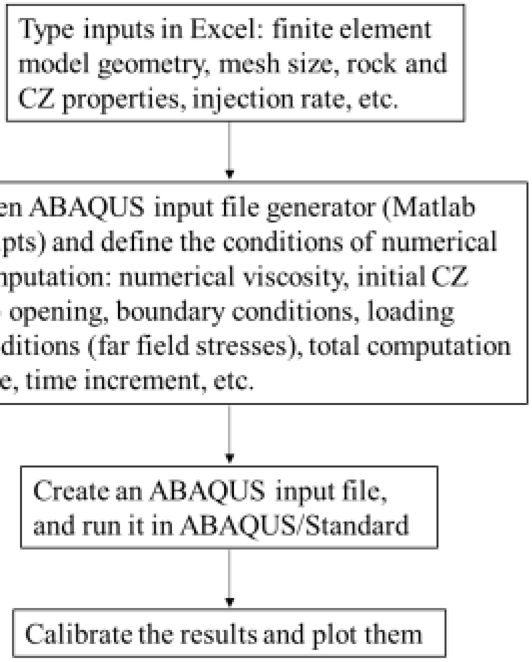

Figure 3.6 - Flow diagram for simulation procedure.

3.4 Numerical Simulations of Hydraulic Fracture Height Growth

3.4.1 Benchmark of KGD Model in a Toughness-Dominated Regime

The numerical model was validated by benchmarking against Adachi’s solution (Adachi, 2001) for the Khristinaovic-Geertsma-de Klerk (KGD) model (Geertsma and de Klerk, 1969). The KGD model is a 2D plane-strain model based on linear elastic fracture mechanics (LEFM). The numerical model was validated for the zero-viscosity (toughness-dominated) regime for a homogeneous, impermeable solid.

Hydraulic fracture growth using multiple, identical layers with welded interfaces was simulated in ABAQUS to compare and benchmark with the analytical KGD model. Figure 3.7 shows these results. The properties for the “intermediate” rock, shown in Table 3.1, were used for this comparison. Results from the analytic solution (red) and ABAQUS (light blue) are shown and represent 10 seconds of injection at 0.001 m^3/s/m injection rate. There is good agreement between the analytic and the FEA models. As mentioned in the introduction, the KGD model based on LEFM is more suitable to stiff rocks, so good agreement would also be expected between the analytic and the FEA models for the “hard “ rock shown in Table 3.1. It should be noted that the fracture height is provided in meters, while the fracture width is provided in millimeters for presentation purposes. The use of an exaggerated width scale, here and throughout this section, is essential for visual inspection of the relationship between fracture height and width in the models.

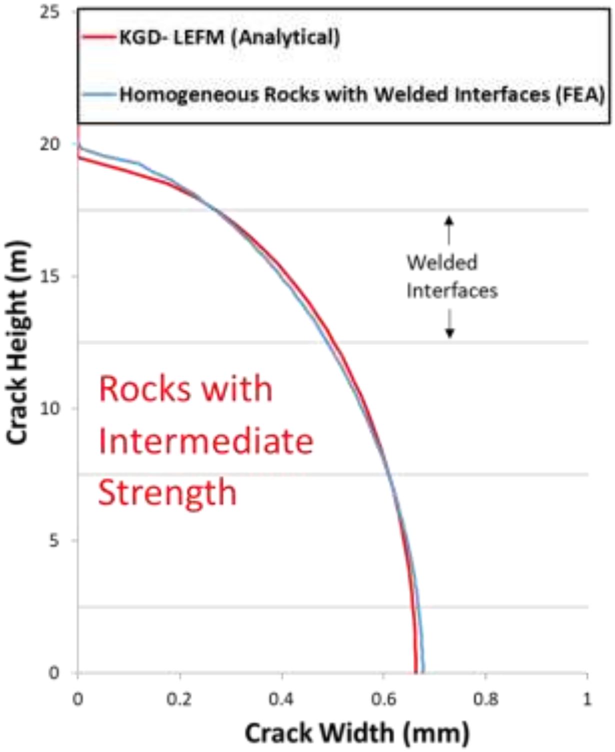

Figure 3.7 - Hydraulic fracture height versus width, in homogeneous layered rocks with welded interfaces (benchmarking KGD model).

3.4.2 Effect of Rock Layering with Contrasting Elastic Properties (Welded Interfaces)

Following a successful benchmarking of the FEA model with the well-known KGD solution, we conducted numerical simulations to evaluate the effect of rock layering on the fracture height versus fracture width relationship. For this purpose, a model simulating layered rocks with a periodic pattern of high Young’s modulus (hard) and low Young’s modulus (soft) layers was constructed (Table 3.1). Figure 3.8 shows the model and the resulting fracture height versus width relationship after 10 seconds of injection at 0.001 m^3/s/m pumping rate. The effect of the layering is evident; a strong contrast in deformation is observed between the stiff and compliant rock layers.

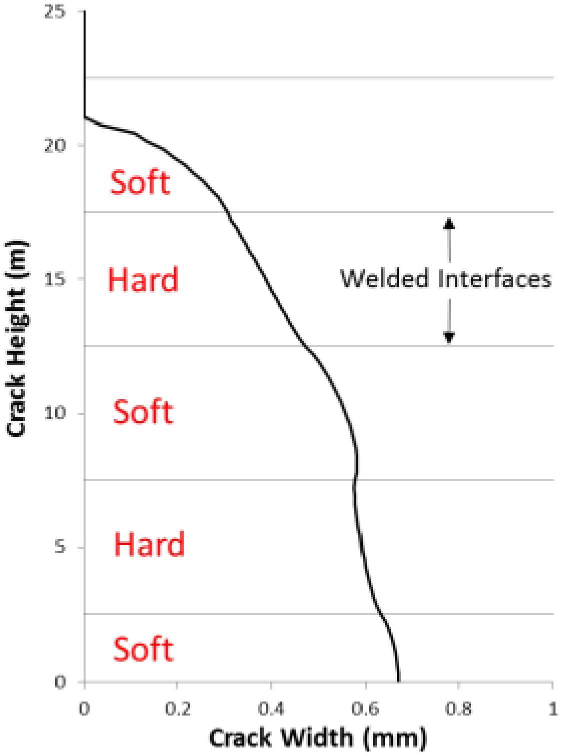

Figure 3.8 - Layering effect on hydraulic fracture propagation.

3.4.3 Effect of Interface Hydraulic Conductivity (Non-Welded Interfaces)

Non-welded interfaces are provided with an initial hydraulic conductivity which increases as the interface opens. This provides the model with pressure-dependent localized regions of fluid loss. To evaluate the effect of the interfaces on fluid loss and fracturing fluid efficiency, we first conducted a parametric evaluation of hydraulic conductivity and its effect on fracture height growth. For this, we maintain all interface properties of cohesive strength and cohesive energy constant and vary the hydraulic conductivity to represent three conditions: 0.1 m/s, 0.5 m/s, and 1 m/s.

Figure 3.9 shows results from these simulations (light blue, red, gray) compared to the case with welded interfaces (black). Figures 3.9-a to 3.9-d, show the fracture height growth as a function of time and at 1, 5, 10 and 20 seconds.

After 1 second of injection, all three curves have a similar fracture height versus fracture width behavior and the differences between them are small. A maximum difference of approximately 20% is observed. As the injection continues, the differences between the various cases increases. The relative differences, however, appears to be the same for the last three cases. The reference case represents a case without fluid loss. The other cases represent conditions of fluid loss associated with the weak interfaces, as controlled by the original hydraulic conductivity of these interfaces and their subsequent increase in hydraulic conductivity with increasing aperture, as the fluid pressure in the interface increases. Thus, the higher the initial hydraulic conductivity, the faster the seepage of fluid to the interface, the faster the subsequent increase in fluid pressure and aperture of the interface, and the higher the overall fluid loss.

Results also show an inverse relationship between fracture height growth and fluid loss. The higher the fluid loss, the smaller the fracture height. For example, at 20 seconds, the fracture height for the model with highest hydraulic conductivity (1 m/s) is the lowest (22.5 m), as compared to 33 m for the fracture without fluid loss. The effect of rock layering and the contrasting elastic stiffness between layers is also observed in

Figures 3.9-a to 3.9-d. The higher the pressure becomes within the fracture, the higher the contrast in deformation between the stiff and compliant layers.

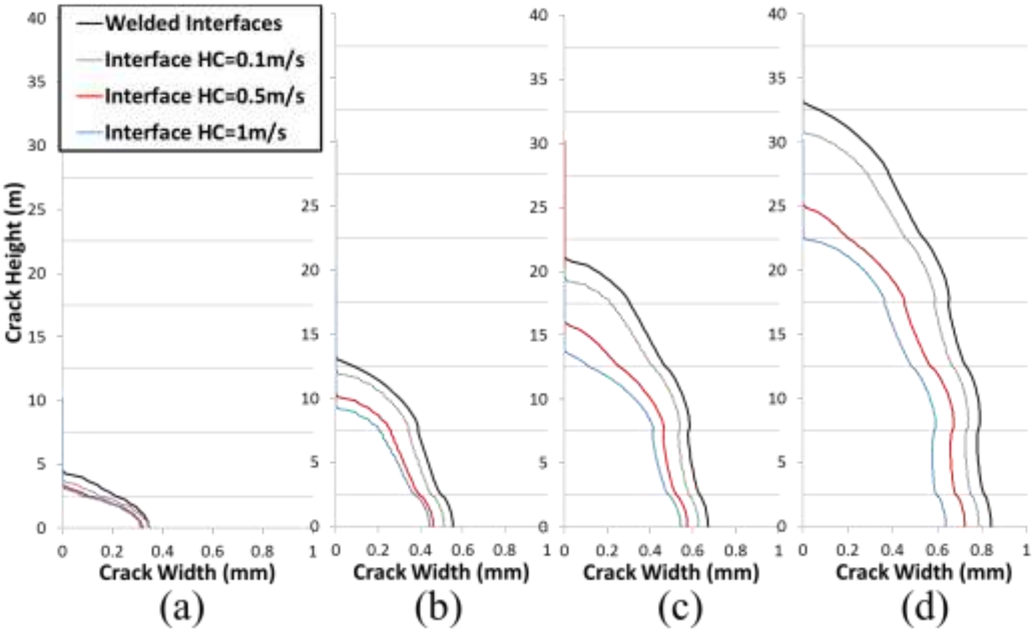

Figure 3.9 - Hydraulic fracture propagation affected by hydraulic conductivity of interfaces: (a) at 1sec; (b) at 5 sec; (c) at 10 sec; (d) at 20 sec.

3.4.4 Effect of Interface Strength (Non-Welded Interfaces)

Figure 3.10 shows the effect of interface strength (T_{max} and G_c) on hydraulic fracture propagation. Three conditions of interface strength are considered with a hydraulic conductivity of 0.5 m/s: high, intermediate and low. The values of the cohesive strength T_{max} and the corresponding fracture energy G_c for these cases are provided in Table 3.3. Figures 3.10-a to 3.10-d, show results of fracture height growth versus width for these cases, as a function of time, after from 1, 5, 10 and 20 seconds of injection. The contrasts between the layered-rock cases and the homogeneous rock (shown in black) are dependent on the interface strength. The higher the interface strength, the smaller the contrast between the fracture heights obtained in the non-welded cases and the welded case. In the near-wellbore region, in the range of fracture height from 0 to 10 m, however, the differences between the behaviors of all three cases are small comparing to those with the larger injection time.

This observed dependence on the interface strength is understood to arise because the fluid's fluid loss in the near-wellbore region is affected by the fluid pressure and fluid velocity more than the interface strength. The fluid pressure reaches the cohesive strengths of the interfaces almost simultaneously and the interfaces open identically for all cases. Away from the wellbore, however, at distances beyond 10 m, the fluid effect in the near-wellbore diminishes, differences in behavior are apparent, and the larger the injection time, the higher the difference in fracture height between the weak and strong interfaces. In these cases, the strength of the weak interface (cohesive-elements) are smaller and can be reached earlier. Therefore, the weak interfaces open earlier resulting in introducing higher fluid loss and less fracture height growth.

Table 3.3 - Three interface strengths based on T_{max} and G_c.

Interface Strength	Cohesive Strength, T_{max} (kPa)	Fracture Energy, G_c (Pa*m)
Strong	250	18
Intermediate	120	12
Weak	50	4

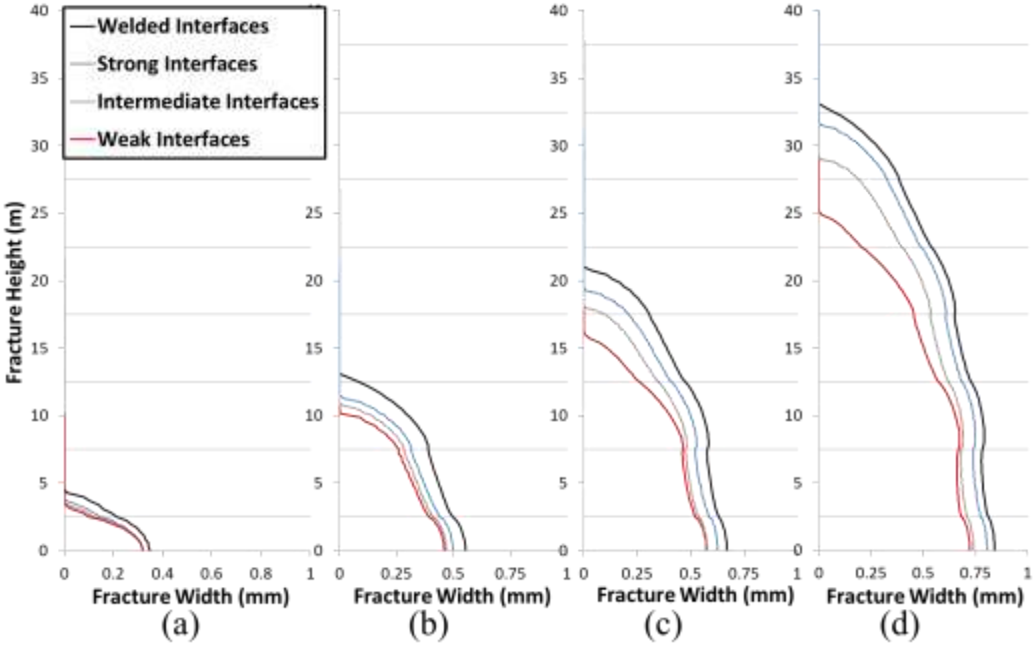

(a) (b) (c) (d)

Figure 3.10 - Hydraulic fracture propagation affected by interface strength: (a) at 1sec; (b) at 5 sec; (c) at 10 sec; (d) at 20 sec.

3.4.5 Effect of Interface Density

The effect of the number of interfaces (interface density) on fluid loss and the fracture height to width relationship was also investigated. For these, a model with 30 rock layers and layer thickness of 5 m (moderately layered rock) is compared to a second model with 60 layers and layer thickness of 2.5 m (finely layered rock). Figure 3.11 shows these results. The behavior of the moderately layered rock is plotted in solid lines and the behavior of the finely layered rock is plotted in dotted lines. Two cases of welded-interfaces and non-welded interfaces (with a hydraulic conductivity in the non-welded cases of 0.5 m/s) are considered. The fracture height growth versus width is shown as a function of time and at 5, 10, 20 and 40 seconds. The finely layered rock, which obviously has a higher density of interfaces per unit length of rock, experiences higher fluid loss to the interface at all times of injection. This is as expected. In contrast, when the interfaces are welded, the results from both cases are identical to each other. This indicates that the differences in fracture height versus width as a function of the increased number of layers with contrasting stiffness is small, and that the differences arise mainly from differences in fluid loss. That being said, in reality there is an expectation that additional fracture energy is spent to cross each interface. So, the larger the number of interfaces, increased energy loss is expected, and hence one would expect diminished height growth. In the control models with welded interfaces, however, the additional energy dissipation associated with non-elastic behavior of the interfaces during crossing is not represented and so they likely represent an understatement of the role of the interfaces in the absence of fluid loss.

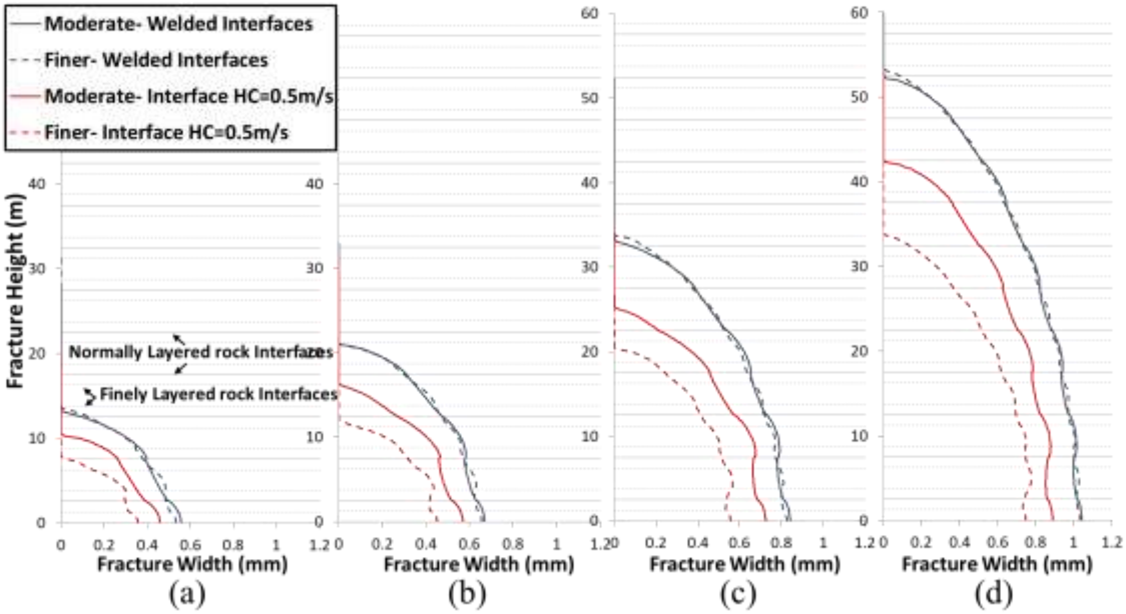

Figure 3.11 - Hydraulic fracture propagation affected by interface density which is characterized by the number and thickness of rock layers: (a) at 5 sec; (b) at 10 sec; (c) at 20 sec; (d) at 40 sec.

3.4.6 Fluid Efficiency

The fluid efficiency is defined as the ratio of the created fracture volume to the total injected fluid volume. To calculate this ratio, the fracture volume per unit length is estimated from the area defined by the fracture height versus fracture width plots in the 2D model. The total injected fluid volume is calculated from the injection rate and the injection time. Figures 3.12-a and 3.12-b show the results of these calculations. The two cases of moderately layered rock and finely layered rock are compared. The total injected fluid volume is plotted in black. The volume of the resulting fracture is plotted in light blue. The difference between these two curves is the fluid loss, and is plotted in orange. At the beginning of the hydraulic fracturing treatment, before the fracture reaches the first interface, the fracture volume equals the total volume, and the fluid efficiency is 100%. Figure 3.12-c shows that until approximately 0.5 seconds, the fluid efficiency of the 5 m thickness layers is 100%. By this time the fluid efficiency of the 2.5 m thickness layers is 46.3%, because the fracture intersected a number of interfaces by this time. After 1 second of injection, the hydraulic fracture in the 5 m thickness layers rock has reached the first interface and 31% of the total fluid has been leaked. At the same time, in the 2.5 m thickness layers rock, the fluid efficiency is significantly lower and equal to 33.5%. Both cases show that each of the fluid efficiency converges to a relatively constant value.

These results represent special cases in that all the interface properties are constant. This is not typically the case. In addition, the injection was stopped before the fluid loss rate along the interfaces became larger than the injection rate. In reality, however, the fluid efficiency may decrease with time, depending on the various interface properties and interface density per unit length of rock, the chosen injection rate, and the length of the treatment. As shown in Figures 3.11-a to 3.11-d and 3.12-c, the finely layered rocks exhibit more fluid loss, along the interfaces, and consequently a lower fracturing fluid efficiency and a shorter fracture.

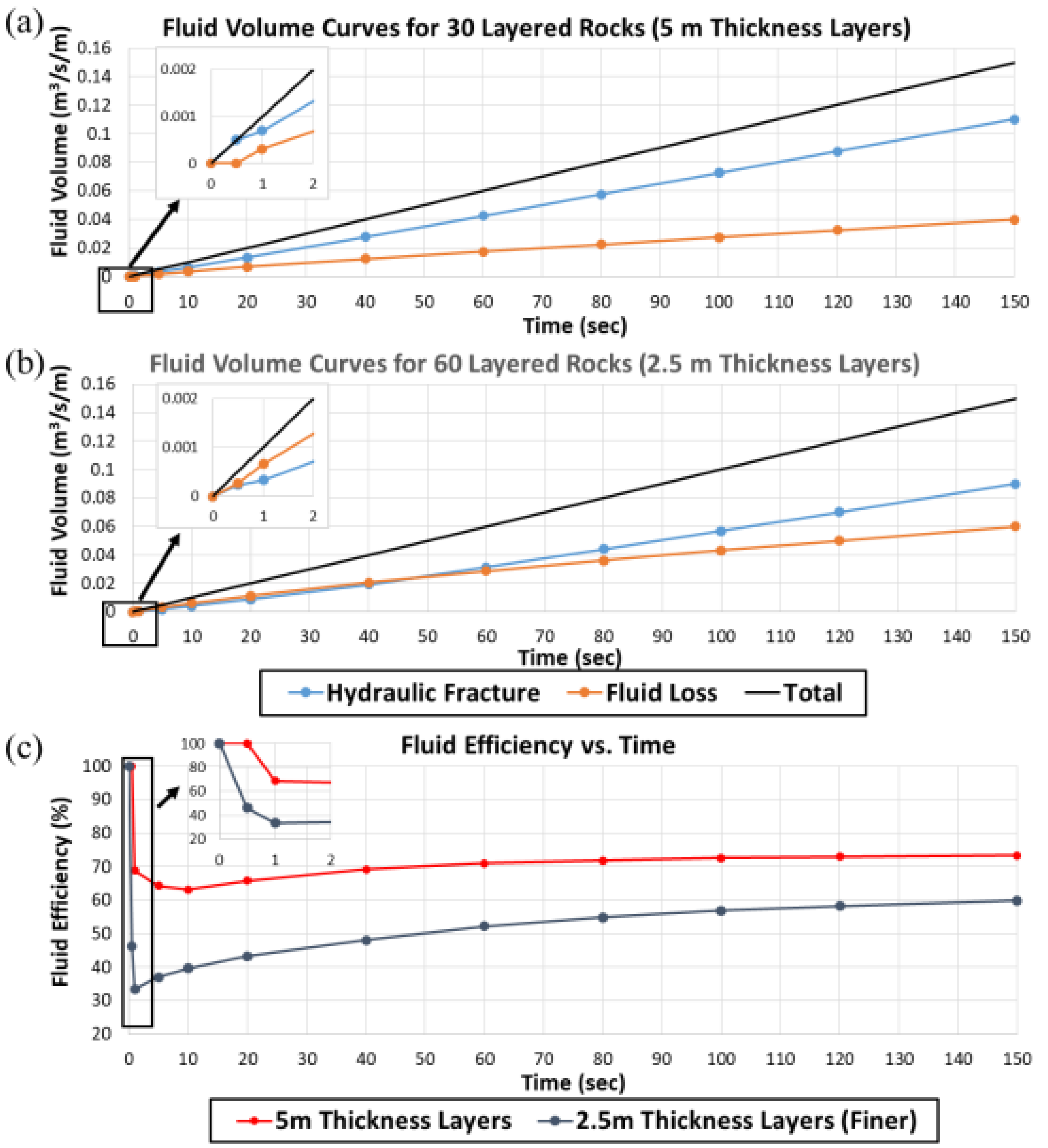

Figure 3.12 - Comparisons of fluid volume and fluid efficiency between 30 and 60 layered rocks with 5 m and 2.5 m thickness layers, respectively: (a) Fluid volume curves for 30 layered rock; (b) Fluid volume curves for 60 layered rocks; (c) Fluid efficiency curves.

3.4.7 Effect of Fluid Viscosity (Non-Welded Interfaces)

The effect of fluid viscosity was also investigated with maintaining other interface properties (T_{max} and G_c) constant. The hydraulic conductivity of pre-existing interface is written as

$$K = \kappa * \frac{\rho g}{\mu} \tag{3.16}$$

where κ is the intrinsic permeability, ρ is the density of the fluid, g is the acceleration due to gravity, and μ is the dynamic viscosity of the fluid. Assuming constant intrinsic permeability within the interface, the hydraulic conductivity and the viscosity have an inverse relationship. The values of sets of hydraulic conductivity and viscosity are provided in Table 3.4. Here three viscosity types are investigated and compared with that in a zero-viscosity regime: low, intermediate and high.

Figures 3.13-a to 3.13-d, show the fracture height growth as a function of time and at 5, 10, 20 and 40 seconds. The fracture height to width relationship in the zero-viscosity regime (red) had already been obtained in Figures 3.9 or 3.10 (both red curves) and also presented here for comparison purposes. As shown in Figures 3.13-a to 3.13-d, all three curves of low, intermediate and high viscosity fluids have an inverse relationship between the fracture height growth and the viscosity, while the fracture width and the viscosity have a direct relationship. However, an important notice should be provided here again. The current model is 2D, and has limitations to some extent because 3D models may give some contradictions to the results of the 2D model.

Table 3.4 - Three types of fracturing fluid based on the viscosity and hydraulic conductivity (assuming constant intrinsic permeability of interfaces).

Viscosity	Viscosity (Pa.s)	Hydraulic Conductivity (m/s)
Zero-Viscosity Regime	0.0001	0.5
Low	0.001	0.05
Intermediate	0.005	0.01
High	0.05	0.001

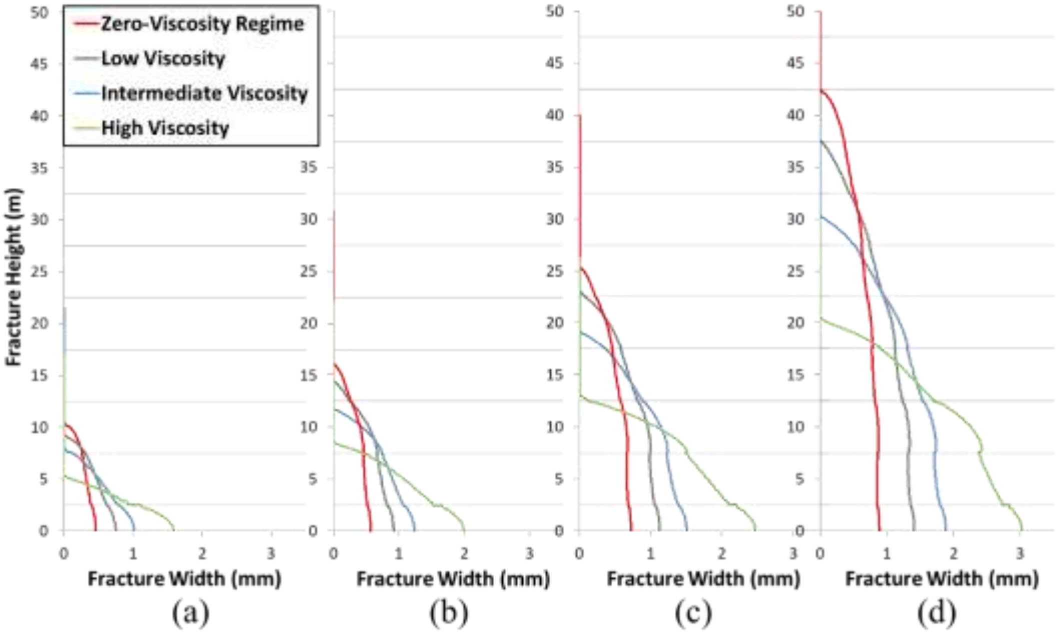

Figure 3.13 - Hydraulic fracture propagation affected by fracturing fluid viscosity: (a) at 5sec; (b) at 10 sec; (c) at 20 sec; (d) at 40 sec.

Figure 3.14 shows the fluid efficiency curves of different viscosity types shown in Table 3.4. The behaviors of all the cases (in the zero-viscosity regime and with the low, intermediate, and high viscosity fluids) show a similar trend in that the fluid efficiency decreases in the near-wellbore region, gradually increases, and then becomes relatively constant at approximate values of 74%, 92%, 96.7% and 99%, respectively. As shown in Figure 3.14, the higher the fluid viscosity, the lower the fluid loss along the interfaces, and consequently a higher fracturing fluid efficiency but a shorter fracture.

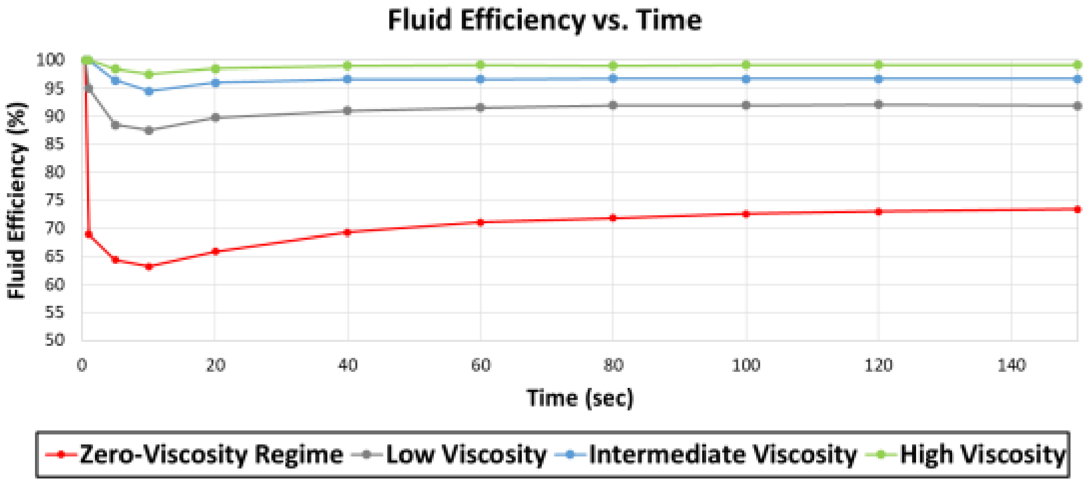

Figure 3.14 - Comparisons of fluid efficiency curves for the cases with various fluid viscosity.

This study has identified that the fluid intrusion through the weak interfaces and the hydraulic fracture geometry are highly influenced by the viscosity of the fluid used in hydraulic fracturing. Hydraulic fracture propagation in low viscous fluid injection is more prone to hindered by the weak interfaces resulting in localized fluid loss controlled by the hydraulic conductivity of the weak interfaces. On the other hand, in the case where high viscous fluid was injected, the fluid tended to create fluid-pressure-driven fracture with a little or almost no fluid loss along the interfaces. For the high viscosity fluid, the pressure at the fracture mouth is much higher resulting in a wider fracture in the proximity of the injection point. Even though the high viscosity fluid causes less fluid loss along the interfaces, the width in the near-wellbore region is relatively much larger and therefore the fracture high growth is retarded resulting in a shorter fracture.

3.4.8 Effect of Highly Layered Heterogeneity of Rocks and Varying Interface Properties

Rock layers with strong heterogeneity (various layer thickness, rock stiffness and interface properties) are investigated. However, this study was based on the assumption that there was no big jump of layer stiffness (from the weak to the stiff) or no extremely weak interface, to avoid hydraulic fracture termination. Table 3.5 shows the rock layer thickness and properties and the associated interface properties used in the model.

Both the layer and interface numbers were counted from the proximity of the well. For limiting a parametric space, a constant value of Poisson's ratio was used. Based on the layer thicknesses and properties shown in Table 3.5, the interface properties were varied with the strength, or both the strength and the hydraulic conductivity. In this study, the interface strength assumed a function of the degree of stiffness difference between neighboring rock layers, which show an inverse linear relationship between them. The hydraulic conductivity at an interface was also assumed to be inversely proportional to the maximum tensile stress T_{max} of the interface, from 0.1 m/s at the maximum T_{max} of 250 kPa to 1m/s at the minimum T_{max} of 15 kPa. The strength levels of the interfaces are based on Table 3.3, which shows that Interfaces 1, 7, 8, 9, 15, 20 and 27 are close to strong interfaces, while Interfaces 3, 4, 5, 6, 10, 11, 12, 14, 16, 17 and 23 are weak interfaces. The rest of the interfaces has intermediate strength.

Table 3.5 - Properties of vertically-heterogeneous rock layers and varying interfaces.

Rock				**Interface**			
Layer #	Thickness, m	E (GPa)	ν	Interface #	T_{max}, kPa	G_c, Pa*m	HC, m/s
1	3	25	0.25				
2	2	32	0.25	1	232	17.33	0.17
3	7	70	0.25	2	118	12.35	0.61
4	6	10	0.25	3	37	3.00	0.92
5	8	45	0.25	4	40	3.50	0.90
6	2	78	0.25	5	50	4.00	0.87
7	10	15	0.25	6	26	2.50	0.96
8	6	34	0.25	7	188	15.59	0.34
9	12	50	0.25	8	199	16.04	0.30
10	3	70	0.25	9	184	15.43	0.35
11	5	78	0.25	10	50	4.00	0.87
12	4	19	0.25	11	15	1.50	1.00
13	9	34	0.25	12	36	3.50	0.92
14	15	69	0.25	13	129	12.91	0.56
15	7	25	0.25	14	50	4.00	0.87
16	2	40	0.25	15	202	16.19	0.28
17	4	78	0.25	16	35	3.00	0.92
18	2	15	0.25	17	26	2.50	0.96
19	9	55	0.25	18	110	11.96	0.64
20	4	30	0.25	19	165	14.64	0.42
21	11	18	0.25	20	213	16.62	0.24
22	3	42	0.25	21	169	14.80	0.41
23	8	74	0.25	22	140	13.46	0.52
24	4	12	0.25	23	29	3.00	0.94
25	2	50	0.25	24	118	12.35	0.61
26	5	12	0.25	25	118	12.35	0.61
27	3	47	0.25	26	129	12.91	0.56
28	7	52	0.25	27	239	17.60	0.14
29	2	80	0.25	28	154	14.15	0.47
30	10	55	0.25	29	165	14.64	0.42

Figures 3.15-a to 3.15-d show the comparisons of the hydraulic fracture height growth with the various interface properties, as a function of time, after from 5, 20, 60 and 100 seconds of injection. Three cases were investigated with different interfaces: 1) interfaces with constant strength (T_{max} = 90 kPa and G_c = 9 Pa.m) and constant hydraulic conductivity (0.5 m/s); 2) interfaces with various strength (Table 3.5) and constant hydraulic conductivity (0.5 m/s); and 3) interfaces with various strengths and various hydraulic conductivities (Table 3.5). The reference case represents a case with welded interfaces (black), and the contrasts between the reference case and all the three cases are large.

The first obvious finding from the study is that the effect of rock layering is also significant in these cases. The various thickness and stiffness of rock layers caused uneven fracture geometry. Our results show that the first case for the interfaces with the constant strength and hydraulic conductivity (red) and the second case for the interfaces with the various strength and the constant hydraulic conductivity (light blue) are similar at all times of injection. On the other hand, the last case for the interfaces with various strengths and hydraulic conductivities (green) is different than the two cases with relatively less varying interfaces (red and light blue). The hydraulic fracture height growth for the case with the most varying interfaces (green) was larger than the latter two, in the near-wellbore region, and became similar to the other two scenarios at 20 seconds of injection. After the injection time of 60 seconds, the fracture height of the most heterogeneous interface case had changed to become the shortest height. This contrast between the cases increased as the injection time progressed from 60 to 100 seconds.

The results show a bigger impact on fluid loss along the interfaces due to interface hydraulic conductivity as compared to interface strength. The values of hydraulic conductivity were defined with an inverse linear relationship with the tensile strength (T_{max}) at the interfaces, so a weaker interface have a higher hydraulic conductivity resulting in more fluid loss along the interfaces. When the variance of the interface hydraulic conductivity was added to that of the interface strength, the change of the resulting fracture height versus width relationship was much bigger than that of the case of only the variance of interface strength, which means that the impact on the fluid loss along the interfaces due to interface hydraulic conductivity was bigger than that of varying interface strength, given the conditions.

As mentioned in section 3.4.4, the effect of fluid pressure and velocity on interface opening are more important than the interface strength, in the near-wellbore region. Except for the near-wellbore region, a combination of increasing or decreasing interface strength from the original (T_{max} = 90 kPa and G_c = 9 Pa.m) used in the constant strength case may minimize its impact on fracture height growth, because the total fluid loss at interfaces is roughly same as estimated from summing the increase or decrease of fluid loss at each interface. The interface opening and the associated fluid loss along the interfaces are a function of fluid pressure coupled with rock displacement and accordingly rock stiffness. As shown in Figure 3.8, the rock stiffness has a strong effect on hydraulic fracture geometry. Like the vertical hydraulic fracture, the interface opening displacement is also affected by the stiffness of tsurrounding rock mass. Thus, given the conditions, varying stiffness of rock layers in an erratic pattern (for both the thickness and properties) may minimize the impact of varying strength of interfaces between layers on hydraulic fracture height growth because the interface open as a function of its top and bottom layer stiffness as well as fluid pressure, while the rock effect on interface opening displacement is smaller in rock layers in a consistent pattern (e.g., vertically-homogeneous layered rocks and periodically layered rocks of soft and hard layers, with constant thickness of each layer). However, the interface hydraulic conductivity assumes a spate numeric variable that is not affected by adjacent rocks, during these simulations.

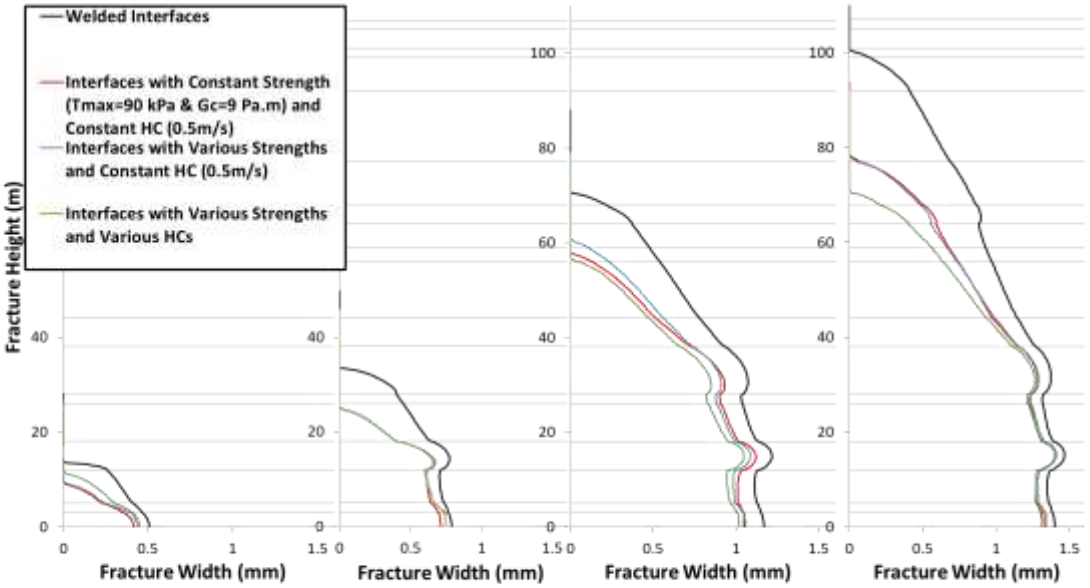

(a) (b) (c) (d)

Figure 3.15 - Comparisons of hydraulic fracture propagation with various layer properties and thicknesses and the associated interface properties: (a) at 5 sec; (b) at 20 sec; (c) at 60 sec; (d) at 100 sec.

Figure 3.16 shows the fluid efficiency for all three cases, as a function of time. The fluid efficiency curves plotted in red and light blue can be considered similar except for some relatively small discrepancies between them up to 80 seconds. This seems to be contradictory to the previous description which describes that fracture height growth is sensitive to interface strength (see Figure 3.10). However, as mentioned above, the influence of interface strength on interface opening and the associated fluid loss along the interfaces may become smaller by varying stiffness of each top and bottom layer of interfaces, if the rock layers are constructed with a combination of high, intermediate or low stiffness layers in an irregular pattern. However, the overall fluid loss in the most varying interface case (green) are totally different with the two cases shown in red and light blue and accordingly, the differences between the values of percent fluid efficiency are large. This happens because the given hydraulic conductivity at an interface is not controlled by adjacent rock layers, based on the definition used in this study.

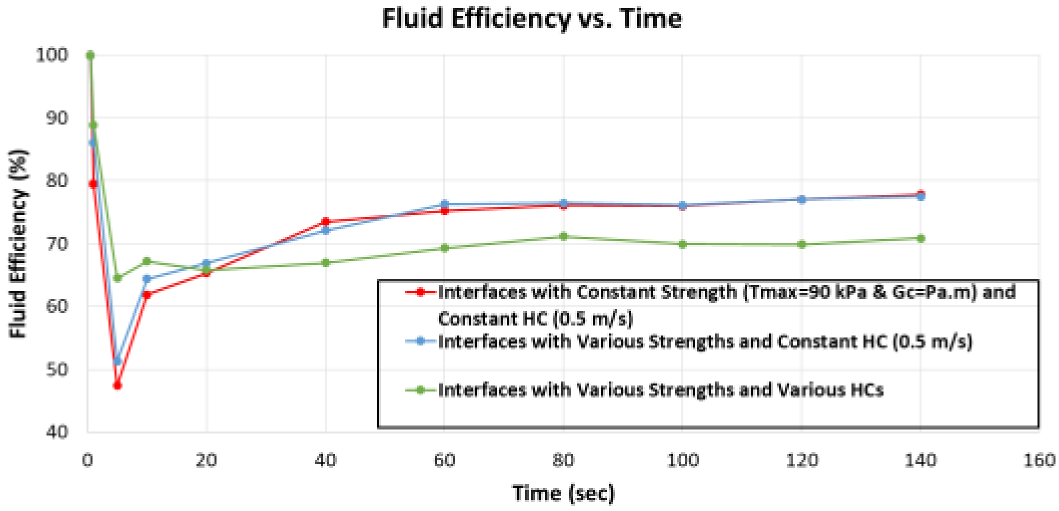

Figure 3.16 - Comparisons of fluid efficiency curves for the various interface cases.

3.5 Conclusions

This study set out to investigate the impact of finely layered reservoir rock structure on vertical propagation (height growth) of hydraulic fracture. This research used finite element simulations to study the interaction of hydraulic fracture with the weak and/or hydraulically-conductive interfaces between the layers. This was done using pore-pressure cohesive elements, which were recently updated to allow the numerical modeling of the hydraulic fracture intersection with crosscutting interfaces. The new features implemented in the code of ABAQUS 2016 are that the updated cohesive zone can identify the fluid properties of Darcy flow with its hydraulic conductivity and void ratio. This is a great importance of being capable of defining the fluid flow properties of an interface or a natural fracture because all non-welded interfaces and pre-existing natural fractures have micro-scale gaps (fluid channels).

The model implements a traction-separation law that has bilinear form and is well determined by properly fixing three parameters such as fracture energy (G_c), maximum traction prior to initiation of the damaging process (T_{max}), and critical separation ratio ($\alpha = \delta_0/\delta_f$). This numerical model benchmarked the simplified but well-known KGD geometry for homogeneous (non-layered) rocks in a toughness-dominated regime.

Rock layering (the presence of thin layers with contrasting elastic properties), the interface hydraulic conductivity, and interface strength were then shown to have an important impact on the width and length of the hydraulic fractures. We also evaluated the effect of interface density per unit length of rock, by contrasting moderately layered with finely layered rocks. Interface shear slip (i.e., non-welded interface behavior) is not considered in the present study.

The most obvious finding to emerge from this study is that interfaces with higher hydraulic conductivity cause higher fluid loss to the interfaces, thus providing a shorter hydraulic fracture height. This implies that in higher hydraulic conductivity, the hydraulic fracture has the propensity to follow the interfaces rather than continuing its path. Furthermore, the study has shown that in rocks with lower Young's modulus, the fracture geometry reflects a lower and wider fracture in comparison to that for rocks with higher Young's modulus, where the geometry reflects higher and narrower fractures.

Interface strength (as controlled by T_{max} and G_c) also defines the opening behavior of the interface under the treatment pressure, thus controlling the fluid loss. The higher the interface strength the lower the fluid loss. Conversely, weak interfaces lead to higher fluid loss, under the same conditions of treatment pressures.

This study has identified that finely layered rocks experience more fluid loss and accordingly less fracture height. This is to be expected because more interfaces provide more locations for fluid loss, and therefore less fluid is available in hydraulic fracture. We also observe that when all the interfaces have similar properties and the interface density per unit length of rock is constant, the fluid efficiency approaches a roughly constant value correlated to the layer thickness.

This study has also identified that fracturing fluid viscosity has a strong influence on fluid loss along the interfaces and its resulting hydraulic fracture height growth. The fluid viscosity has an inverse relationship with the fracture height growth, while the fracture viscosity and the width show a direct relationship. Low viscosity fluid causes more fluid loss at the interfaces, while in the case of high viscosity fluid, the fluid loss along the interfaces is relatively small resulting in a higher fluid efficiency.

The results of the rock model with highly layered heterogeneity and varying interface properties show that the hydraulic conductivity of interfaces may have more influence on fluid loss along the interfaces as compared to interface strength in the specific range of those of the interfaces and the vertically-heterogeneous layered rocks used in this study. The impact of interface strength seems even negligible except for the region in wellbore proximity. This may happen because the influence of interface strength on interface opening and its resulting fluid loss becomes smaller or larger in interaction with varying or constant thickness and/or stiffness of adjacent rock layers. On the other hand, even though the interface hydraulic conductivity has an inverse linear relationship with the interface strength, the former is less controlled by the vertical heterogeneity of rock layers.

The most importance of the current investigation is the ability of such a model to quantify the impact of fluid loss to interfaces on hydraulic fracture growth. Future efforts will be aimed at detailed parametric studies, seeking relationships among interface conductivity, layer thickness, and efficiency. Future efforts will also aim to quantify the inelastic deformation of the interfaces even in the absence of fluid loss, thereby enabling quantification of their impact on the energy required for hydraulic fracture height growth.

4. EFFECT OF ROCK LAYERS AND WEAK INTERFACES ON CASING IMPAIRMENT INDUCED BY FORMATION SLIP

4.1 Introduction

The majority of wells drilled for oil/gas production have to be cased and cemented in order to maintain zonal isolation and wellbore integrity. Casing cemented in place is typically one of the main structural components of a wellbore. It stabilizes the wellbore, prevents contamination of fresh water and production zones, isolates significantly different pressure gradients, and allows control of formation fluids and well pressures to be maintained during drilling and completion operations. Due to its importance to the long-term success of the well as well as the fact that once installed, it is operationally difficult to remediate issues with casing, it is paramount that the casing is designed and installed properly to begin with. The costs of casing installation makes up a significant portion of the overall well cost and any required remediation only increases that burden on the well's economics.

Casing failure may lead to the impairment of casing structural integrity which will result in leakage or the loss of well serviceability by restricted well access (Xie, 2006; Xie and Liu, 2008; Shafiei and Dusseault, 2013; Xie et al., 2016). Casing impairment induced by formation slip has become increasingly prominent during hydraulic fracturing and thermal recovery processes. Bedding-plane interfaces may experience localized slippage induced by contact with a connected opening vertical hydraulic fracture and reservoir expansion under a thermal recovery process. Figure 4.1

shows a schematic representation of a horizontal well which is susceptible to bedding-plane slip at uphole and the reservoir/caprock interface. This situation has been observed in the field, where vertical portions of the wellbore experienced casing failures during hydraulic fracture treatments (Rho et al., 2018). The well configuration shown in Figure 4.1 is commonly used today in production of unconventional reservoirs such as shale and mudstone and heavy oil reservoirs (Xie et al., 2016).

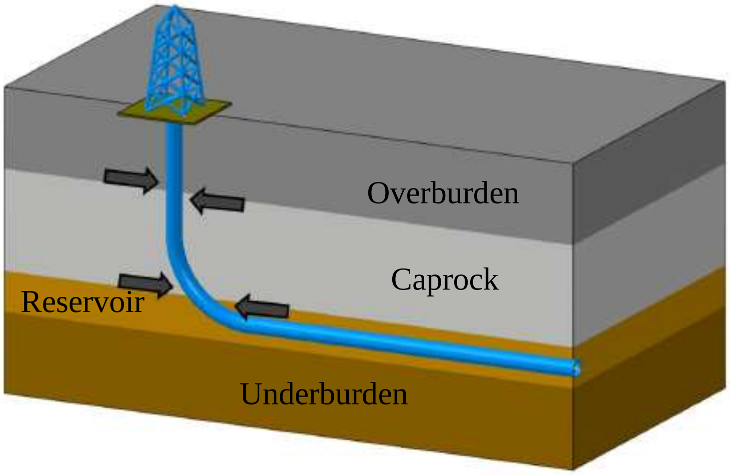

Figure 4.1 - Schematic representation of a horizontal well prone to experience bedding-plane slip (modified from Xie et al., 2016).

Various authors have investigated casing impairment caused by formation slip displacement through tectonic movement (Han et al., 2006; Cui, 2015; Hu et al., 2016). The effect of casing deformation and shear failure induced by reservoir compaction and long-term production has also been previously investigated and reported (Yudovich, et al., 1989; Hilbert et al., 1996; Hilbert et al., 1999; Dusseault et al., 2001; Dusseault, 2011; Bruno, 2002; Furui, et al., 2012).

Many researchers have also investigated the problems of bedding-plane slip occurring during hydraulic fracturing (Cooke and Underwood, 2001; Gu et al, 2008; Rutledge et al, 2015; Rutledge et al, 2016; Rho et al., 2018). Bedding-plane slip can be driven by fluid invasion and pressure at interfaces during vertical hydraulic fracture opening (Rutledge et al., 2016). Chuprakov and Prioul (2015) show the process of vertical hydraulic fracture growth and how it is slowed or halted as relatively weak interfaces are encountered. During crack arrest, shear at bedding planes can be promoted by fluid invasion and pressure along the bedding interfaces and increased horizontal stress by the fracture net pressure (Rutledge et al., 2016).

More recently, many investigators have considered that the formation slip movement and the subsequent casing impairment can also occur during thermal recovery processes (Wong and Chau, 2006; Xie 2006; Xie and Liu, 2008; Shafiei and Dusseault, 2013; Xie et al., 2016). In particular, Collins (2005) and Khan et al. (2011) conducted caprock integrity analysis in SAGD operations. They highlighted differential surface heave as a function of differential thermal expansion and shearing as well as dilation of oil sands during the thermal operations, as potentially being the source of localized slip along the weak interface between the reservoir and caprock. It should be noted that "surface" refers to the ground surface or the interface surface between the caprock and the underlying reservoir rock.

In addition, many researchers have investigated the behavior of casing itself in thermal recovery wells, in terms of its thermal properties and performance (Maruyama et al., 1990; Maharaj, 1996; Wu et al., 2005; Xie and Tao, 2010; Tang et al., 2013; Kang, 2014; Ikponmwosa et al., 2015). Stresses induced by thermal loads are one of the key factors that influence the integrity of the casing, especially considering they are typically in excess of 200°C, in heavy oil reservoirs. When coupled with physical casing-cement-formation interaction, casing damage may be accelerated due to the differences in thermal properties of materials.

In this study, we are interested in modelling of casing shear induced by formation shear movement, which has a distinct probability occurring during thermal recovery processes (Wong and Chau, 2006; Xie and Liu, 2008; Xie et al., 2016). Finite element analysis (FEA) was conducted to investigate the casing integrity in a casing-cement-formation system, using a commercial FEA software, ABAQUS. Two different cases were simulated and compared: casing shear induced by formation slip movement in the condition of no temperature elevation and at the peak casing temperature during a single thermal cycle in CSS.

Given certain conditions, the casing may not exhibit complete loss of integrity. Instead, it may deform enough that the necessary size tubulars or tools cannot pass through it and thus the well loses its serviceability. In this study, this too is considered a failure. Our results show that the 1.2 inch formation slip displacement caused large and abrupt change of casing curvature, particularly near the slip surface, and a wide range of tensile failure in the modeled cement sheath as well as lateral displacement, along the casing. Under these conditions, the casing shear also resulted in an operational failure due to reduction of drift diameter as a result of the severe cross-sectional ovality of the casing. This was a function of obvious plastic deformation after yield, near the shear plane. A deformation such as this will cause serious problems when installing equipment or accessing to the well during completion operations.

We also conducted simulations for investigating the impact of thermally-induced stresses and diminished material properties with increasing temperature and how these would affect casing deformation damage. The simulation focused on K55 steel casings that despite and sometimes because of its relatively low yield strength is used in thermal enhanced oil recovery (EOR) operations. When the same formation slip displacement was applied, the casing encountering high-temperature, high-pressure steam incurred higher plastic deformations near the slip surface. These findings are critical as they must be considered, when casing strings are designed for use in thermal recovery wells, in order to avoid or mitigate casing shear. This is especially true in the regions where formation slip movement occurs, accompanied by shear failure along the planes of weakness. Solutions, which will be discussed, include optimizing the well path, adopting special completions approaches, and considering other methods, such as under-reaming or use of slip joints.

4.2 Basic Definitions and Theories

4.2.1 Thermally-Induced Stresses During Cyclic Steam Stimulation

Cyclic Steam Stimulation (CSS), also known as Huff and Puff, consists of three phases: injection, soaking, and production. In CSS, steam is injected into the well at high pressure and temperature for time periods ranging from several days to several weeks. After the injection phase, the heat is allowed to soak into the formation for a period that typically lasts for 2 to 3 weeks. During the soaking phase, the mobility of the oil is improved due to both heating and the addition of any solvents or other chemicals introduced during the injection process. Finally, the hot oils is produced from a production well until the production rate drop below a short-term economic limit. The length of the production phase will vary based on reservoir and will range in time from weeks to months (Clark, 2007).

During CSS operations, the casing will experience a large number of heating and cooling cycles before the recovery per cycle drops below an overall economic limit and the well is abandoned. Since the annular space between the casing and the formation is filled with cement, thus allowing forces to be transmitted from the formation to the casing with minimal damping, the cyclic thermal loading of the formation itself, with its high temperatures, typically in excess of 200˚C (392 ˚F), results in induced high thermal stresses in the casing. The value of the induced thermal stresses in the casing may exceed the yield point of its material both in tension and compression.

Figure 4.2 illustrates three loading stages in a single thermal cycle, showing the general relationship between the casing’s axial stress and temperature over the temperature cycle, from the initial temperature to the maximum operating temperature and back to the original temperature. In the heating stage, the casing string itself expands and axial compressive stress develops because the string is axially constrained by the presence of a cement sheath around it (Xie et al., 2016). After the induced compressive stress reaches the yield point of the material, it begins to gradually decline during plastic deformation. Subsequently, in the hot-hold period, the axial compressive stress significantly decreases due to stress relaxation. In the cooling stage, the constrained casing begins to contract and the axial compressive stress dramatically decreases after being switched to tensile loading. Depending on the material properties and the peak temperature range, some low-strength casings (such as K55 and L80) reach yield under tension loading, at the end of a thermal cycle (Xie, 2006). This is of particular interest to this study as these low-strength materials are often used in thermal recovery projects.

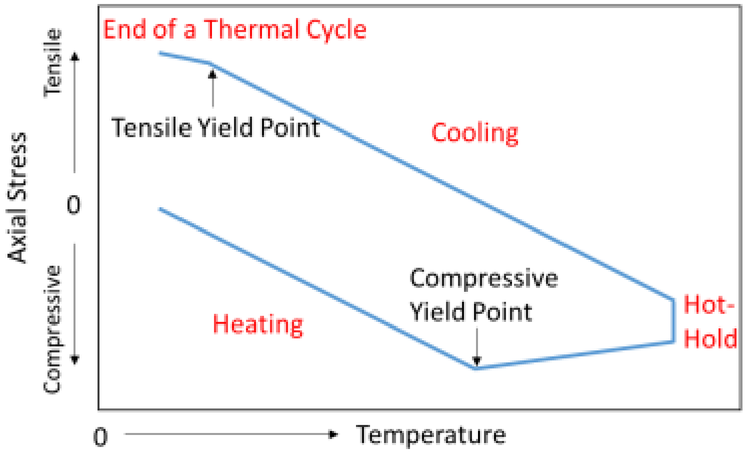

Figure 4.2 - General relationship between axial stress and temperature for a casing string (modified from Maruyama et al., 1990 and Xie and Tao, 2010).

4.2.2 Induced Formation Surface Heaving and Associated Localized Slip Along a Bedding Interface During Steam Assisted Gravity Drainage

As shown in Figure 4.3, in a SAGD operation, two horizontal wells (injector and producer) are drilled parallel to each other and separated by a constant vertical distance (typically 5 m). Steam is then injected into the upper well and a steam chamber develops and grows with a cone-like cross-section within a reservoir unit. The heat and steam rise, and condensed water and mobilized oil flow down by gravity, to be produced through the producer well (Butler, 1991).

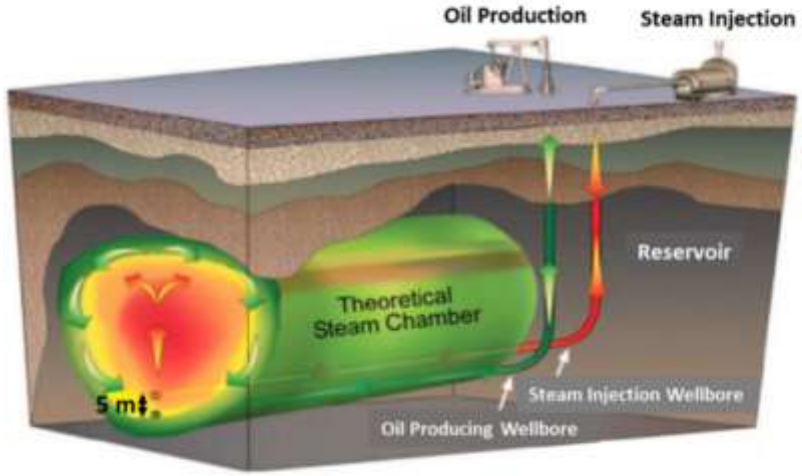

Figure 4.3 - Schematic illustration of typical SAGD Process (reprinted from Peacock, 2010).

Differential thermal expansion rates between the reservoir and the overburden caprock can be generated by a relatively rapid-convective-heating system (i.e., the reservoir) and a slow-conductive heating system (i.e., the caprock). This can lead to concentration of shear stress along the interface and when the shear stresses become large enough shear slip may occur along the interface. This can occur at differential temperatures between the reservoir and the caprock that are as low as 40 to 60˚C (104 to 140˚F).

Illustrating the SAGD-induced heave occurring after the continuous steam injection time of several months, Figures 4.4-a, b and c represent the simplified temperature profile, the induced stress concentration along the interface, and the possible localized bedding-plane slip, respectively. The simple surface heave model uses 200 °F steam and assumes the worst-case scenario that heat transfer takes place through only conduction and no heat is transferred to the caprock.

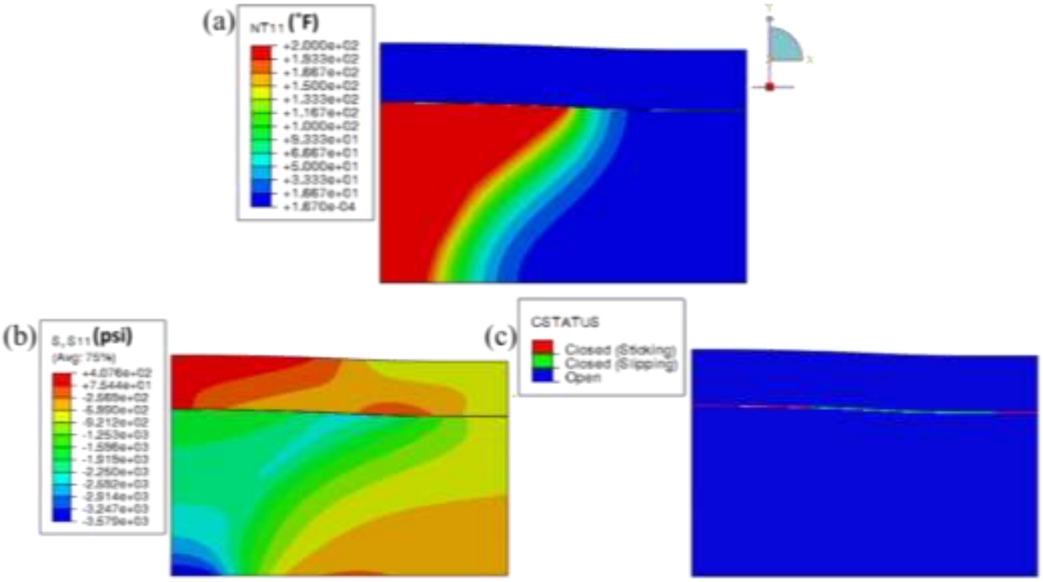

Figure 4.4 - Expected surface heave occurring after continuous steam injection for several months during a SAGD operation (no heat conduction to the caprock was assumed for a worst-case scenario): (a) Temperature profile; (b) Induced stress concentration; (c) Localized bedding-plane slip (green).

4.3 Finite Element Model Setup

4.3.1 Model Geometry and Mesh

Figure 4.5 shows the geometry and mesh for a casing-cement-formation model. The casing used in this study was a 7 inch (177.8 mm), 23 lb/ft (34.2 kg/m) K55 steel-grade string. K55 or N80 casings have been commonly used in thermal EOR applications, but their low yield strength possibly cause casing hot-yield during the thermal processes (Wu et al., 2005; Wu et al., 2008). All dimensions used in defining the geometry for the FEA model are displayed in Table 4.1. Neglecting the poromechanical effect in rocks, C3D8T elements (coupled displacement-temperature 8 nodes solid elements with full integration) were used for the cement as well as for the caprock and reservoir. For the casing pipe body, S4RT elements (coupled displacement-temperature 4 nodes shell elements with reduced integration and hourglass control) were used to investigate the curvature caused by the formation slip displacements. However, C3D8RT elements were used for the casing pipe body when considering the condition of high temperatures. This was because the casing model meshed by the thin shell elements was not able to support the compressive axial stress developed by its thermal expansion and axial confinement, due to its weakness to the stress. In this case, the mesh size for the thickness has to be small enough to approach the thickness of the shell elements. If the mesh size is not small enough for the casing thickness, the curvature and plastic strain would be overestimated due to its higher stiffness, given the same conditions. However, the results obtained from the mesh size we used in this study were within 5% of that of the shell elements.

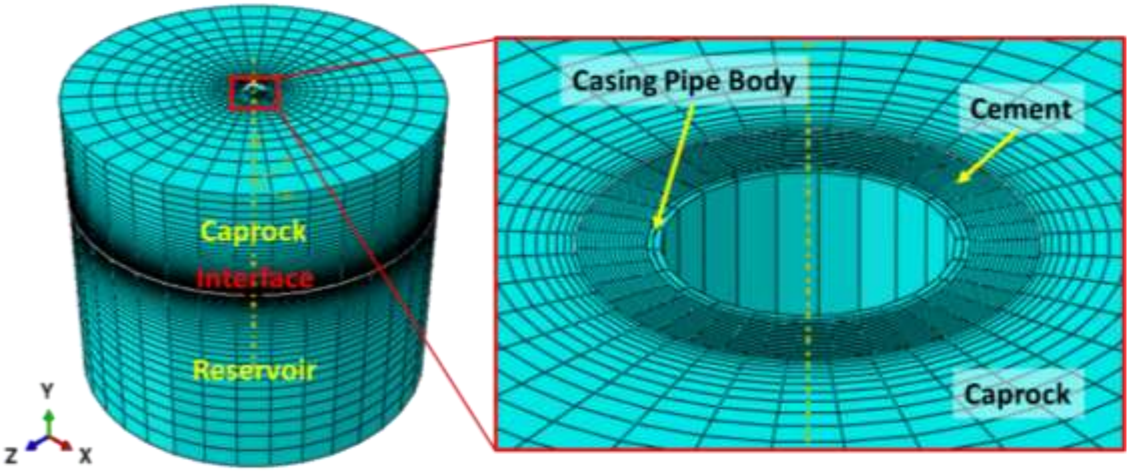

Figure 4.5 - Geometry and mesh of the model built in ABAQUS.

Table 4.1 - Dimensions of each unit in a casing-cement-formation system.

	Inner Diameter, D_{in}	Outer Diameter, D_{out}	Thickness, t	Height, h
Casing	6.366 in (161.7 mm)	7 in (177.8 mm)	0.317 in (8.05 mm)	180 in (4572 mm)
Cement	7 in (177.8 mm)	10 in (254 mm)	1.5 in (38.1 mm)	180 in (4572 mm)
Caprock	10 in (254 mm)	210 in (5334 mm)	100 in (2540 mm)	60 in (1524 mm)
Reservoir	10 in (254 mm)	210 in (5334 mm)	100 in (2540 mm)	120 in (3048 mm)

4.3.2 Material Properties

Table 4.2 shows the mechanical and thermal properties of the casing, cement, and rocks used in this study. For the rocks, we selected Athabasca McMurray Formation oil sands and their caprock, Wabiskaw Shales, both of which are commonly found in thermal EOR operations in western Canada. The original rock temperature before steam injection was assumed to be a room temperature (25˚C) for the both rocks. We are evaluating the specific case of casing response under formation shear movement, and therefore, except for the casing, the cement and rocks were defined as linear elastic materials for simplicity of modeling (Table 4.2). The material properties used in this study were obtained from available literatures (Scott and Seto, 1986; Collins, 2002; Zandi et al., 2010; Kaldal et al., 2013; Kaldal et al., 2015).

Table 4.2 - Mechanical and thermal properties of materials.

Parameter	K55 Casing	Cement	Caprock	Reservoir
Density, kg/m^3	7850	2300	2420	2320
Young's Modulus, GPa	207	15	0.25	0.343
Poisson's Ratio	0.3	0.23	0.35	0.3
Yield Strength, MPa (minimum)	388.17	-	-	-
Ultimate Tensile Strength, MPa (minimum)	730.84	-	-	-
Elongation, % (Minimum)	23.2	-	-	-
Thermal Expansion Coefficient, K^{-1}	1.20E-05	1.00E-05	1.00E-04	4.00E-05
Thermal Conductivity, W/(m.k)	45	0.8	1.5	2
Specific Heat, J/(kg.K)	490	900	900	900
Tensile Strength, MPa	-	2.7	-	-
Compressive Strength, MPa	-	27	-	-

For the K55 steel casing, the elongation (EL) rate as well as the diminished Young's modulus E, yield strength S_y, and ultimate strength S_u are defined for a range of temperatures T (Table 4.3). The increase of thermal expansion coefficient with temperature is also shown in Table 4.4.

Table 4.3 - K55 steel casing Young's modulus and strength degradation with temperature (modified from Snyder, 1979).

T (˚C)	E (GPa)	S_y (MPa)	S_u (MPa)	EL Rate
25	208.22	388.17	730.84	0.232
260	195.81	384.73	792.21	0.127
316	190.98	371.63	770.14	0.2
371	186.16	358.53	689.48	0.21

Table 4.4 - K55 steel casing thermal expansion coefficient increase with temperature (modified from Torres, 2014).

T (˚C)	α (K^{-1})
21	1.163E-05
93	1.296E-05
149	1.388E-05
204	1.467E-05
260	1.535E-05
316	1.595E-05
371	1.642E-05
427	1.679E-05

4.3.3 Loading and Boundary Conditions

Casing shear impairment is generally caused by both upper and lower formation slip displacements. The displacements overserved in several Canadian thermal EOR fields are approximately 1.2 inches in total (Xie and Liu, 2008). The formation shear displacements were applied in opposing directions over the two adjacent formation layers. Displacements of all elements in the normal direction were restricted except for the rocks. Assuming a relatively shallow reservoir at 200 m (656.2 ft) depth, overburden pressure of 367.5 psi, calculated by the vertical pressure gradient of 0.56 psi/ft due to the weight of rock only, was applied to the caprock surface and the Young's moduli of rocks were assumed to be relatively small.

To model the steam injection process, high temperature steam is injected on the inner wall of casing and the amount of heat is continuously propagated to the rocks through the casing and cement sheath, as a function of the injected steam temperature and wellbore heat losses (Saripalli et al., 2018). Assuming temperature gradually decreases with heat loss and becomes the original temperature of rocks on formation boundary, the temperature of formation boundary was maintained constant during the whole process of the simulation.

Both casing-cement and cement-formations interfaces have less influences on casing plastic deformation after some formation slip displacement occurs. This is because the cement can detach and slip independently if the shear stresses developed become greater than the maximum shear stress τ_{max} (shear strength) shown in Table 4.5. The interfaces' friction coefficient (μ) was also introduced using an isotropic Coulomb model, to define the interface sliding behavior (Table 4.5). The interface properties used in Table 4.5 were also obtained from available literature (Ladva et al., 2005; Capasso and Musso, 2010; Kaldal, et al., 2013).

Table 4.5 - Properties of casing-cement and cement-formation interfaces.

	Casing-Cement Interface	Cement-Formation Interface
Friction Coefficient, μ	0.3	0.5
Max Shear Stress, τ_{max} (MPa)	0.46	0.55

4.4 Numerical Simulation

4.4.1 Casing Shear

Output variable SK2 from ABAQUS gives the section curvature at integration points, about the y-axis in this xyz coordinate system, and the raw values are commonly converted to degrees per 30 m (in SI units) or degrees per 100 ft (in imperial or US Customary units). The peak curvature was 40°/100 ft and occurred near the slip surface on the R-R’ path. The casing curvature and deformation on the L-L’ path were relatively small.

Figure 4.6-a shows the schematic illustration of shear displacements applied in opposing directions over the two adjacent formation layers and the induced curvature change along the casing. Figure 4.6-b shows the curvature distributions along the two paths, L-L’ and R-R’, on the casing outer surface, after the slip displacement. Since the rate of slip displacement was kept constant in both directions, the casing curvature distributions on the paths were symmetrical with respect to the origin. The peak casing curvature was approximately 47°/100 ft, generated by stress concentration (compression) in the areas just above and below the shear plane. As shown in Figure 4.6-b, we observe large and abrupt change of curvature as well as lateral displacement, along the casing, due to formation shear movement. Obviously, this causes serious problems for future access into the well.

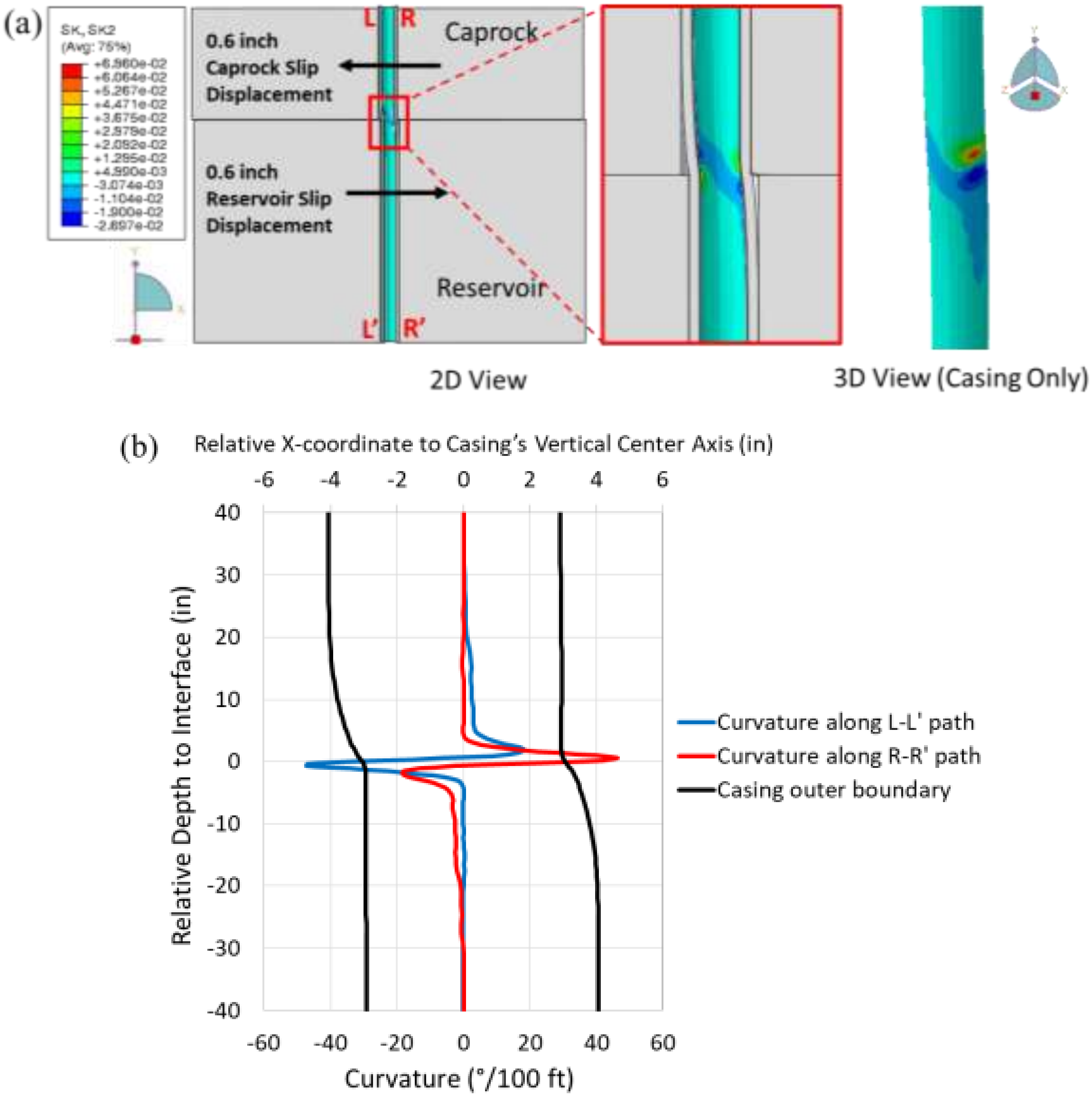

Figure 4.6 - (a) Schematic of a total 1.2 inch formation slip displacement (0.6 inch displacement in two opposite directions) over the shear plane and casing curvature caused by the formation shear movement; (b) Curvature distribution along the two L-L' and R-R' paths illustrated in (a).

Figures 4.7-a and 4.7-b show the equivalent plastic strain distribution along the casing and a schematic drawing of the casing's cross-sectional oval shape developed by casing lateral displacement, respectively, under the behavior shown in Figure 4.6-a. The cement sheath and formation were assumed to be elastic materials and therefore show zero plastic strain (blue). The maximum plastic strain value generated by the formation slip movement was approximately 0.055 and the regions of the maximum plastic strain correspond to those of the peak curvatures described in Figure 4.6. The plastic strain distribution on the casing also shows a symmetric pattern with respect to the origin because the rate of slip displacement and the total displacement of each formation are constant. As shown in 3D views in Figure 4.7-a, the maximum equivalent plastic strain value of each region where stress concentrations are formed is approximately 0.06.

Figure 4.7-b shows a cross-sectional view of the oval casing developed by the casing lateral displacement. As the maximum and minimum diameter, D_{max} and D_{min}, of the oval shown in Figure 4.7-b indicates, the serious oval shape of the casing exhibits casing failure. The maximum and minimum values of the casing outer diameter (OD), are 7.25 and 5.79 inches, respectively. If the D_{min} is less than the drift diameter (6.241 inches) for the 7 inch, 23 lb/ft casing used in this study, we call the condition an operational failure of casing.

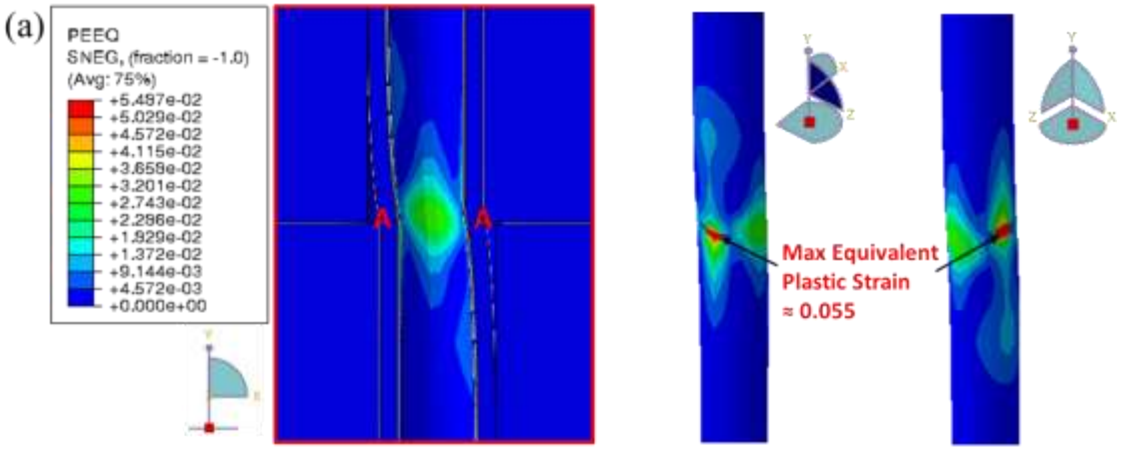

2D View

3D View (Casing Only)

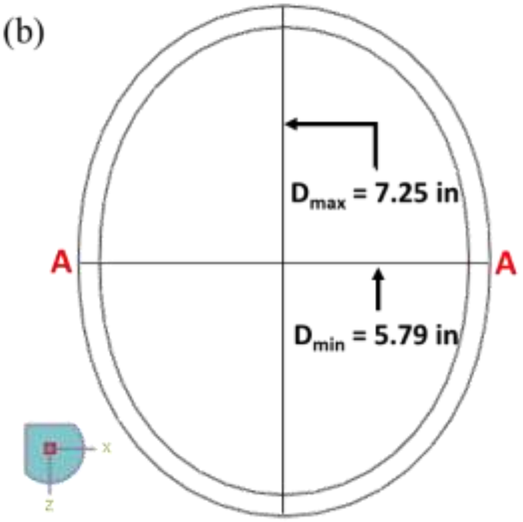

Oval Cross Section Along A-A

Figure 4.7 - (a) Equivalent plastic strain contours along the casing, after a total 1.2 inch formation slip displacement (0.6 inches in two opposing directions) over the shear plane; (b) Schematic drawing of the developed cross-sectional ovality of the casing along the section A-A. A-A represents the casing cross section corresponding to the shear plane.

4.4.2 Cement Failure

Cement was defined as a linear elastic material in these initial numerical experiments, therefore cement failures were investigated during post-processing of the simulation results. The tensile strength of cement is low and typically assumed to be 10 times smaller than the compressive strength (Kaldal et al., 2015). As shown in Figure 4.8, given the condition of the total formation slip distance of 1.2 inches (0.6 inches in two opposite directions) over the shear plane, large regions of the modeled cement sheath represent tensile failure (grey) due to its relatively low tensile strength. The large tensile failure regions may result from the assumption that the material is linear elastic with no crack development. A more accurate approach in regards to cement modeling would have been to model the cracks themselves, especially in this case with high tensile stresses. That would likely show that the cement would already be cracked around the shear plane, after a much smaller formation slip displacement, which gives the same end result – wellbore integrity failure. The compressive failure (black) in the cement is also shown near the regions where the cement encounters each formation at the slip surface. The area of the compressive failure in the cement is much smaller than that shown in the tensile failure regions of the cement. The investigation into the cement stresses is important for a proper casing/cementing design to mitigate or retard the casing shear.

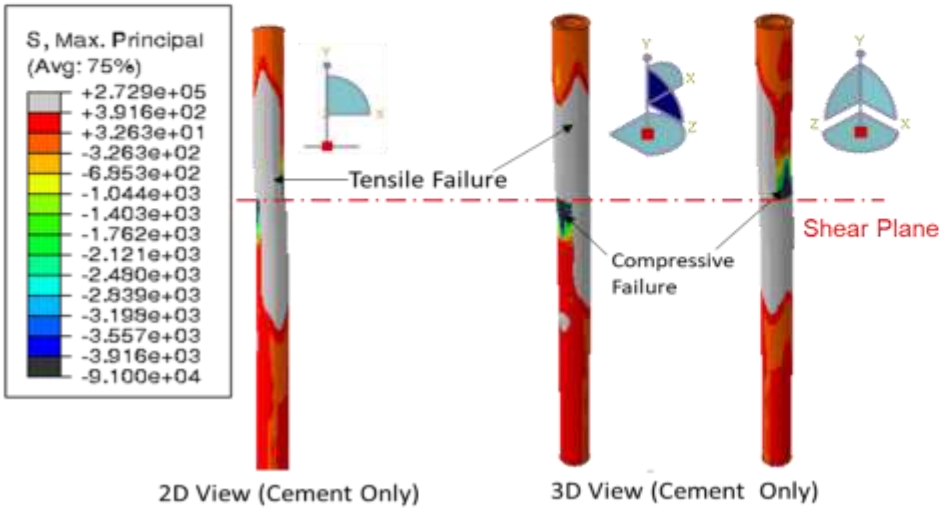

Figure 4.8 - Schematic representation of tensile and compressive failures in the modeled cement sheath, under the same conditions as Figures 4.6 and 4.7.

4.4.3 Effect of Thermally-Induced Stresses and Casing Strength Degradation at High Temperatures

Figures 4.9-a and 4.9-b show heat transfer taking place through only conduction in the casing-cement-formation system and the resulting temperature profiles in the heating and hot-hold stages, respectively. Output variable NT11 from ABAQUS represents the nodal temperature at each node. The steam temperature used in this study was set to 677 °F, for a worst-case scenario. The typical peak temperatures for CSS wells range between 330 °C (626 °F) and 350 °C (662 °F) (Xie and Liu, 2008). On the other hand, the steam pressure selected was relatively small, which is reasonable in the shallow reservoir depth assumed in this study, because injection pressures depend on the reservoir depth from which the current reservoir pressure and stiffness can be estimated. Injection pressures have to be greater than the current reservoir pressure at the depth, but should not cause serious damages to the formation (Rodríguez et al., 2008). The heating stage corresponds to the injection phase in CSS where the heat provided by steam injection begins to transfer to the neighboring medium. In the hot-hold stage, injection typically transitions to soaking and the temperature profile is steam temperature near wellbore transitioning to the original reservoir temperature in the outer side boundaries of rocks.

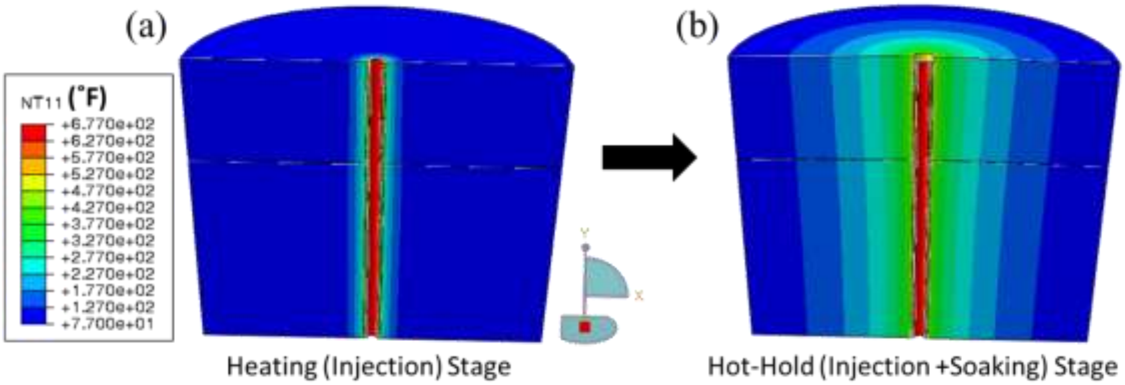

Figure 4.9 - Temperature contour plots during a single thermal cycle: (a) in the heating stage; (b) in the hot-hold stage.

Figure 4.10-a shows the schematic of two-way formation shear movement occurring during the hot-hold stage shown in Figure 4.9-b. Given the conditions, equivalent plastic strain contours on the casing pipe body are shown in 2D and 3D views (Figure 4.10-b). Even when a much smaller formation slip distance of 0.72 inches in total (0.36 inches in two opposing directions) was applied, a similar maximum equivalent plastic strain (0.0574) to the case with no temperature elevation (Figure 4.7-a) was developed just below the shear plane. The fact this failure occurs in a situation with

much lower applied displacement reveals the impact of degraded casing strength due to high temperatures as well as compressive stresses induced by thermal expansion due to the temperature increase of 600˚F, from the original (77˚F) to the injected steam's (677˚F).

Another obvious finding is that the largest equivalent plastic strain values in each of two paths, L-L' and R-R', are different and that in both paths, these large strain regions are located below the shear plane. This is a different result when compared to those shown in Figure 4.7-a. This could be explained by the interaction behavior between the cemented casing and formations at the high peak temperature. Different thermal properties (such as thermal conductivity and expansion) of the formations as well as thermally-induced compressive stresses in the casing likely induce a complex stress profile in the casing before the formation shear movement.

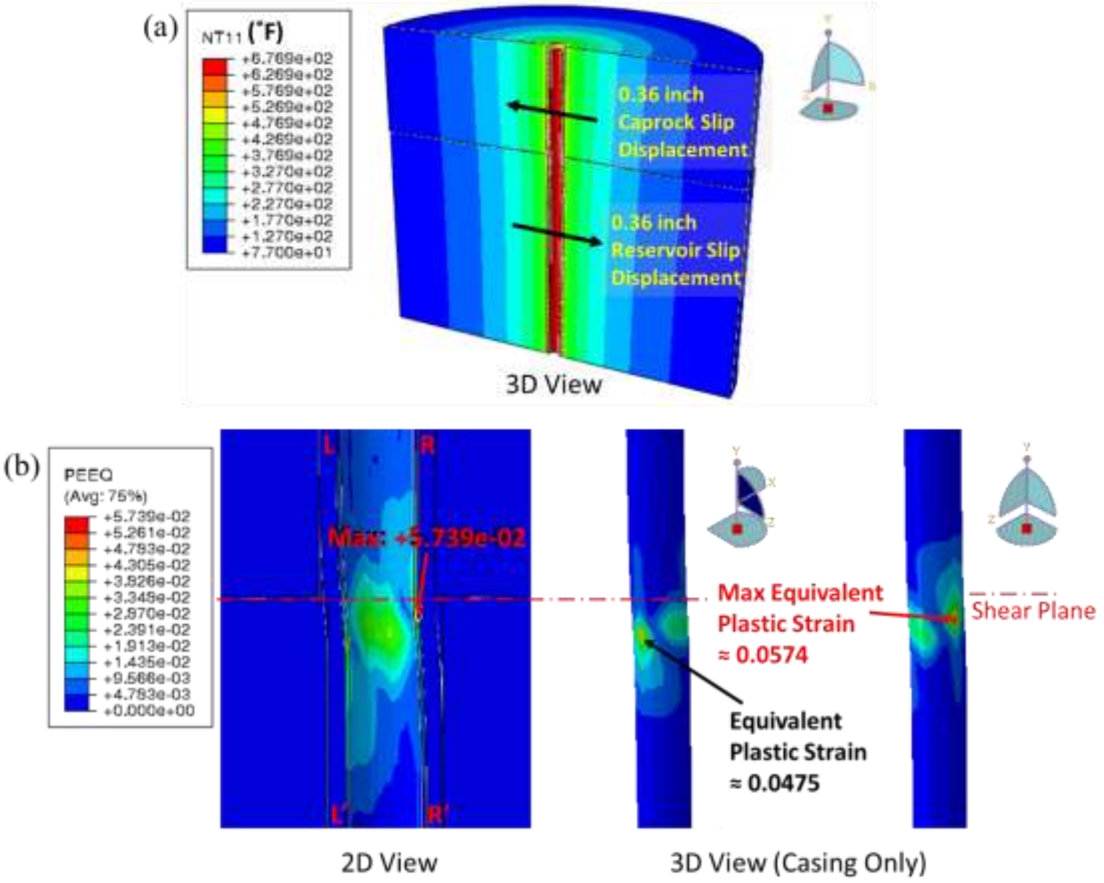

Figure 4.10 - (a) Schematic of a total 0.72 inch formation slip displacement (0.36 inch displacement in two opposing directions) over the shear plane, at the peak casing temperature 677 °F; (b) Plastic strain distribution along the casing, under the given conditions illustrated in (a).

4.4.4 Mitigation Strategies to Prevent Casing Shear Impairment

Attempting to strengthen the casing and cement is not likely to be beneficial when it comes to resisting the loads created by formation shear. The reaction force from the casing and cement is too small to resist the formation shear movement even for the strongest casing or cement materials. Solutions include leaving the annulus uncemented where bedding interfaces are encountered due to higher risk of formation slip. This can retard the casing shear because there is a space between the casing and the wellbore, allowing the formation slip displacement as much as the space. Other solutions also include avoiding of shearing zones, using of slip joints or ductile cement, and finding the special exploitation and completion approaches to mitigate the magnitude. In thermal reservoir stimulation, more uniform heating or slower heating may reduce the stress concentration along the interface between layers and accordingly formation shear and shear slip induced by the interface slippage.

4.5 Conclusions

3D finite-element simulations were conducted to examine the casing impairment induced by formation slip displacement occurring with shear failure along the week interface between two distinct rock layers. Using a casing-cement-formation system, two different cases of casing shear induced by formation slip were simulated and compared: casing shear with no temperature effect and at the peak casing temperature during a single thermal cycle in CSS.

When no temperature elevation was accounted for and formation slip displacement was a total of 1.2 inches, large and abrupt changes of curvature near the shear plane as well as large lateral displacements, along the casing where observed. This will likely cause loss of well serviceability (e.g., complete loss or restricted well access) during completion operations. The peak casing curvature near the slip surface was approximately 57°/100 ft and the curvature distributions along the L-L’ and R-R’ paths were symmetric, with respect to the origin (Figure 4.6-b).

The regions of the maximum plastic strain along the casing correspond to those of the peak curvatures. The maximum plastic strain value was approximately 0.06 near the slip surface, after the total 1.2 inch formation slip movement. Given the conditions above and the assumption that cement is a linear elastic material, large regions of the modeled cement sheath reveal tensile failure due to its relatively low tensile strength and no actual crack generated in the model. However, the cement may already have been cracked near the shear plane, after a much smaller formation shear displacement. These findings are important for a proper casing/cementing design to mitigate or retard the casing shear.

We also investigated the impact of thermally-induced stresses and degraded casing strength with increasing temperature, on casing shear deformations. At the peak temperature condition during a single thermal cycle, the casing had already entered a plastic period of the material’s elastoplstic behaviors and experienced obvious plastic deformation caused by the thermally induced compressive stresses and its weakened yield strength. This resulted in higher plastic deformations on the casing, comparing to the case of no temperature increase, if other variables, except for the temperature changes, were maintained and the same formation slip displacements were applied to the formations.

Strengthening the casing and cement is not likely to be helpful when it comes to resisting the loads created by formation shear. The reaction force form the casing and cement is too small to resist the formation shear movement. Solutions include avoiding of shearing zones, leaving shear zones uncemented, using of slip joints or ductile cement, and finding the special exploitation and completion approaches to mitigate the magnitude. In thermal reservoir stimulation, more uniform heating or slower heating may reduce the stress concentration along the interface between layers and accordingly formation shear and shear slip induced by the interface slippage.

Future efforts will aim to conduct 3D finite-element simulations on casing connections which are more susceptible to high stress concentration. Low cycle fatigue analysis of both casing pipe body and connection subjected to multiple cycles of steam stimulation will also have to be conducted to investigate the cyclic degradation of casing strength and stiffness and the accumulated plastic deformations after each cycle. Finally, future efforts will include more realistic reservoir simulations supported by actual field temperature profiles and poromechanical effect in reservoirs. This will be capable of simulating coupling behaviors of rock matrix and pore fluids and analyzing shear dilation and permeability enhancement of the heavy oil reservoirs.

5. SUMMARY, CONCLUSIONS AND RECOMMENDATIONS

5.1 Summary and Conclusions

This work was done with three major subjects of numerical simulations. We used finite element simulations to investigate the impact of the presence of rock layers and weak interfaces on: 1) shear stress development, shear slip at interfaces, and wellbore stability; 2) hydraulic fracture height growth; and (3) casing shear impairment.

The first scenario, part of a broader field study, set out to investigate the conducted on layered and discontinuous rocks, specifically organic-rich mudstones and carbonate sequences, to investigate the effect of rock layers with contrasting mechanical properties, and with weak interfaces between layers, on stress development and wellbore stability. We also investigated formation shear failure due to shear stress development along horizontal planes of weakness during hydraulic fracturing.

For this, three different layered rock models were simulated and compared using 3D finite-element simulations: laterally-homogeneous, laterally-heterogeneous, and strongly laterally-heterogeneous. For the latter, the heterogeneity was introduced by randomly varying the elastic rock properties of each layer.

Results show that localized shear stresses develop along interfaces between layers with contrasting properties and along the wellbore walls. This includes the generation of localized shear in planes that were principal in the homogeneous model. It was also seen that rock shear and slip, along interfaces between layers, may occur when the planes of weakness are pressurized during vertical hydraulic fracturing. The level of heterogeneity and pressure loading used in this study was not sufficient for shear failure. However, the simulations we conducted propose that strong heterogeneity and strong structural components may result in sufficient shear stress development for shear failure along the interfaces between rock layers.

In the second scenario, we used 2D finite-element simulations to investigate the impact of rock layering and interfaces on a connected opening vertical hydraulic fracture and its interaction with the interfaces between layers. For this, the newly-implemented pore pressure cohesive elements in ABAQUS 2016 were used as certain predefined hydraulic fracture and interface opening paths.

To validate the cohesive zone model and for comparison, we conducted simulations on elastically-homogeneous and elastically-layered rocks and, for the latter, we conducted parametric studies on tensile strength and fluid flow properties of the interfaces between layers, to understand their impact on vertical hydraulic fracture (height) growth. The impact of rock layering on hydraulic fracture geometry was also investigated in both cases.

The most obvious finding gained from this study is that the presence of thin layers with contrasting properties have a strong influence on the width and length of the vertical hydraulic fracture. Rock layers with low stiffness resulted in shorter and wider fractures, while high stiffness rock layers incurred longer and narrower fractures. We also observe that the interface hydraulic conductivity and interface strength have a direct effect on fracture height growth as well as fluid efficiency. Interfaces with higher hydraulic conductivity and/or lower strength cause higher fluid loss to the interfaces and consequently less fracture height growth and fluid efficiency. However, the influence of varying interface strength in highly vertically-heterogeneous layered reservoirs may be minimized or neglected by adjacent rock layers' stiffness. These findings are important for a proper assessment of fracture height growth, a better assessment of the created fracture surface area, and better predictions of well production.

In the third scenario, with the presence of weak interfaces between rock layers, the formation may experience shear slip resulting in casing shear. The induced casing shear stresses may result in serious economic loss causing casing shear failure, loss of well integrity, as well as loss of access to wells during completion operations. This study also discusses that the different thermal expansion rates of the caprock and reservoir rock during thermal recovery operations may cause localized slip along the bedding plane interface. This will occur where stress concentrations along the interface have developed due to volume changes which appears in the form of surface heave (at the both bedding interfaces and top surface).

3D Finite-element simulations were also conducted in a casing-cement-formation system to examine the casing impairment induced by formation shear movement arising with shear slip along the bedding plane interface between two distinct rock layers. The results show that when no temperature change is assumed and the formation slip distance approaches to a total 1.2 inch displacement, the casing experiences obvious plastic behaviors after yield and a wide range of the modeled cement sheath indicates tensile failure due to the relatively low tensile strength and the assumption that the material is linear elastic. Casing failure in terms of operation is also expected from the severe cross-sectional oval shape at the slip surface.

We also investigated the impact of thermally-induced stresses and diminished material properties at high temperatures, on casing plastic deformations due to shear. When the same formation slip displacement was applied during a high peak temperature condition for the casing, in a single thermal cycle, the casing shear incurred higher plastic deformations near the slip surface than the case of no temperature increase. These findings are important to avoid or mitigate casing shear in the region where formation slip movement occurs, accompanied by shear failure along the planes of weakness.

An ideal numerical model has to combine the above three scenarios in a model because they are all interrelated phenomena. Rock shear and slip, along interfaces between layers, may occur when the planes of weakness are pressurized during hydraulic fracturing operations. Both mechanical and fluid flow properties of rocks and interfaces can also have an important impact on hydraulic fracture geometry. The rock shear and slip can also be induced by non-uniform thermal expansion rates and subsequent surface heave of formation layers during thermal recovery processes and cause casing shear impairment when the planes of weakness intersect the well paths at depth.

5.2 Recommendations for Future Work

For an ideal numerical simulation, the first, second and third scenarios in this dissertation should be combined in a model to obtain a more realistic coupling behaviors of rocks, fluids and casings. To accomplish this, the following specific requirements have to be satisfied in future.

1) The ideal model should be a three dimensional model which is capable of modeling anisotropic reservoirs, simulating hydraulic fracture volume growth in all xyz directions of Cartesian coordinates, and simulating realistic casing deformation arising by formation slip. This model may require a very high amount of Computer CPU and memory.
2) Also, the poroelastic effect in reservoirs has to be considered to simulate the coupling between rock deformation and fluid flow in reservoirs because stress and displacement in rocks are strongly influenced by fluid pressure in both micro- and macro-scale flow channels within the rocks as well as external loads applied.
3) In the numerical hydraulic fracture simulation through multi-layered rocks, the surface elements are tied with the pore-pressure cohesive elements, and therefore shear stress and shear slip along the interfaces between them were neglected. However, hydraulic fracture termination through a weak interface is significantly dominated by the weak shear strength and the resulting shear slip which should be included in a realistic model.
4) Casing connections are more susceptible to failures (such as paring, thread rupture, and leakage) than the casing pipe body, and therefore should be considered in this study of casing impairment arising by formation slip

movement. It is expected to have thread rupture by large plastic deformation and connection parting even when a small slip displacement.

5) Multiple thermal cycles in CSS will also have to be considered to investigate low cycle fatigue behaviors of both casing pipe body and connection as well as to evaluate the cyclic degradation of casing strength and stiffness and the accumulated casing material damage after each cycle.

REFERENCES

Abaqus. 2016. *Abaqus 2016 Documentation*.

Adachi, J.I. 2001. Fluid-Driven Fracture in Permeable Rock. PhD thesis, University of Minnesota, Minneapolis.

Bar-Cohen, Y. and Zacny, K. 2009. *Drilling in Extreme Environments: Penetration and Sampling on Earth and Other Planets*. Weinheim, Germany: Wiley-VCH Verlag.

Barenblatt, G.I. 1959. The Formation of Equilibrium Cracks During Brittle Fracture: General Ideas and Hypothesis, Axially Symmetric Cracks. *J. Appl. Math. Mech.* **23** (3): 622–636.

Barenblatt, G.I. 1962. The Mathematical Theory of Equilibrium of Cracks in Brittle Fracture. *Adv. Appl. Mech.* **7**: 55–129.

Boone, T.J., and Ingraffea, A.R. 1990. A Numerical Procedure for Simulation of Hydraulically-Driven Fracture Propagation in Poroelastic Media. *Int. J. Numer. Anal. Meth. Geomech.* **14** (1): 27–47.

Bourne, S.J. 2003. Contrast of Elastic Properties Between Rock Layers as a Mechanism for the Initiation and Orientation of Tensile Failure under Uniform Remote Compression. *Journal of Geophysical Research* **108** (B8), 2395. doi: 10.1029/2001JB001725.

Bruno, M.S. 2002. Geomechanical and Decision Analyses for Mitigating Compaction-Related Casing Damage. *SPE Drilling & Completion* **17** (3): 179–188. doi: 10.2118/79519-PA.

Butler, R.M. 1991. *Thermal Recovery of Oil and Bitumen*. Englewood Cliffs, NJ: Prentice-Hall.

Capasso, G. and Musso, G. 2010. Evaluation of Stress and Strain Induced by the Rock Compaction on a Hydrocarbon Well Completion Using Contact Interfaces with Abaqus. SIMULIA Customer Conference, Providence, Rhode Island, USA, 24–27 May.

Carrier, B. and Granet, S. 2012. Numerical Modeling of Hydraulic Fracture Problem in Permeable Medium Using Cohesive Zone Model. *Eng. Frac. Mech.* **79**: 312-328.

Chen, Z., Bunger, A.P., Zhang, X., and Jeffrey, R.G. 2009. Cohesive Zone Finite Element-Based Modeling of Hydraulic Fractures. *Acta. Mech. Solida Sinica* **22** (5): 443–452.

Chen, Z., Jeffrey, R.G., Zhang, X., and Kear, J. 2017. Finite-Element Simulation of a Hydraulic Fracture Interacting with a Natural Fracture. *SPE J.* **22** (1): 219–234.

Chuprakov, D. and Prioul, R. 2015. Hydraulic Fracture Height Containment by Weak Horizontal Interfaces. Paper SPE-173337-MS presented at the SPE Hydraulic Fracturing Technology Conference, The Woodlands, Texas, USA, 3–5 February.

Clark, B. 2007. Working Document of the National Petroleum Council Global Oil & Gas Study. http://www.npc.org/Study_Topic_Papers/22-TTG-Heavy-Oil.pdf.

Collins, P.M. 2002. Injection Pressures for Geomechanical Enhancement of Recovery Processes in the Athabasca Oil Sands. Paper SPE/PS-CIM/CHOA 79028 presented at the SPE International Thermal Operations and Heavy Oil Symposium and International Horizontal Well Technology Conference, Calgary, Alberta, Canada, 4–7 November.

Collins, P.M. 2005. Geomechanical Effects on the SAGD Process. Paper SPE/PS-CIM/CHOA 97905 presented at the SPE International Thermal Operations and Heavy Oil Symposium, Calgary, Alberta, Canada, 1–3 November.

Cooke, M.L. and Underwood, C.A. 2001. Fracture Termination and Step-Over at Bedding Interfaces Due to Frictional Slip and Interface Opening. *Journal of Structural Geology* **23**: 223–238. doi: 10.1016/S0191-8141(00)00092-4.

Cook, R.D, Malkus, D.S., Pleasha, M.E., and Witt, R.J. 2002. *Concepts and Applications of Finite Element Analysis*. Fourth edition. New York, NY: John Wiley & Sons, Inc.

Cui, Y.M. 2015. Finite Element Simulation of Casing Shear Impairment in Different Cementing Method. *Advances in Petroleum Exploration and Development* **9** (1): 39–42.

Deutsch, C. 1989. Calculating Effective Absolute Permeability in Sandstone/Shale Sequences. *SPE Formation Evaluation* **4** (3): 343–348. doi: 10.2118/17264-PA.

Dugdale, D.S. 1960. Yielding of Steel Sheets Containing Slits. *J. Mech. Phys. Solids* **8** (2): 100–104.

Dusseault, M., Bruno, M, and Barrera, J. 2001. Casing Shear: Causes, Cases, Cures. *SPE Drilling & Completion* **16** (2): 98–107. doi: 10.2118/72060-PA.

Dusseault, M. 2011. Geomechanical Challenges in Petroleum Reservoir Exploitation. *KSCE Journal of Civil Engineering* **15**: 669–678. doi: 10.1007/s12205-011-0007-5.

Economides, M.J. and Nolte, K.G. 2000. *Reservoir Stimulation*. Third edition. Chichester, UK: John Wiley & Sons.

Elkateb, T., Chalaturnyk, R., and Robertson, P.K. 2003. An Overview of Soil Heterogeneity: Quantification and Implications on Geotechnical Field Problems. *Canadian Geotechnical Journal* **40**: 1-15. doi: 10.1139/t02-090.

Furui, K., Fuh, G., and Morita, N. 2012. Casing- and Screen-Failure Analysis in Highly Compacting Sandstone Fields. *SPE Drilling & Completion* **27** (2): 241–252. doi: 10.2118/146231-PA.

Garagash, D.I. 2006. Propagation of a Plane-Strain Hydraulic Fracture with a Fluid Lag: Early-Time Solution. *Int. J. Solids Struct.* **43**: 5811–5835.

Geertsma, J. and de Klerk, F. 1969. A Rapid Method of Predicting Width and Extent of Hydraulic Induced Fractures. *J. Pet. Tech.* **246**: 1571–1581.

Gil, I., Nagel, N., Sanchez-Nagel, M., and Damjanac, B. 2011. The Effect of Operational Parameters on Hydraulic Fracture Propagation in Naturally Fractured Reservoirs – Getting Control of the Fracture Optimization Process. Paper ARMA-11-391 presented at the 45th US Rock Mechanics/Geomechanics Symposium, San Francisco, CA, USA, 26–29 June.

Gonzalez, M., Taleghani, A.D., and Olson, J.E. 2015a. A Cohesive Model for Modeling Hydraulic Fractures in Naturally Fractured Formations. Paper SPE-173384-MS presented at the SPE Hydraulic Fracturing Technology Conference, The Woodlands, Texas, USA, 3–5 February.

Gonzalez-Chavez, M., Puyang, P., and Taleghani, A.D. 2015b. From Semi-Circular Bending Test to Microseismic Maps: An Integrated Modeling Approach to Incorporate Natural Fracture Effects on Hydraulic Fracturing. Paper SPE-178544-MS presented at the Unconventional Resources Technology Conference, San Antonio, Texas, USA, 20–22 July.

Gu, H., Siebrits, E., and Sabourov, A. 2008. Hydraulic-Fracturing Modeling with Bedding Plane Interfacial Slip. Paper SPE-117445-MS presented at the SPE Eastern Regional/AAPG Eastern Section Joint Meeting, Pittsburgh, Pennsylvania, USA, 11–15 October.

Haddad, M. and Sepehrnoori, K. 2015. Simulation of Hydraulic Fracturing in Quasi-Brittle Shale Formations Using Characterized Cohesive Layer: Stimulation Controlling Factors. *J. Unconv. Oil Gas Resour.* **9**: 65-83.

Haddad, M., Du, J., and Vidal-Gilbert, S. 2017. Integration of Dynamic Microseismic Data with a True 3D Modeling of Hydraulic-Fracture Propagation in the Vaca Muerta Shale. *SPE J.* **22** (6): 1714–1738.

Han, H., Dusseault, M, Xu, B., and Peng, B. 2006. Simulation of Tectonic Deformation and Large-Area Casing Shear Mechanisms – Part B: Geomechanics. Paper ARMA-06-1004 presented at Golden Rocks 2006, The 41st U.S. Symposium on Rock Mechanics (USRMS), Golden, Colorado, USA, 17–21 June.

Helwany, S. 2007. *Applied Soil Mechanics: with ABAQUS Applications*. New York, NY: John Wiley & Sons, Inc.

Hilbert, L.B., Fredrich, J.T., Bruno, M.S., Deitrick, G.L., and de Rouffignac, E.P. 1996. Two-Dimensional Nonlinear Finite Element Analysis of Well Damage Due to Reservoir Compaction, Well-to-Well Interactions, and Localization on Weak Layers. Paper ARMA-96-1863 presented at the 2nd North American Rock Mechanics Symposium, Quebec, Canada, 19–21 June.

Hilbert, L.B., Gwinn, R.L., Moroney, T.A., and Deitrick, G.L. 1999. Field-Scale and Wellbore Modeling of Compaction-Induced Casing Failures. *SPE Drilling & Completion* **14** (2): 92–101. doi: 10.2118/56863-PA.

Holditch, S.A. 2006. Tight gas sands. *J. Pet. Technol.* **58** (6): 86–93.

Hu, C., Ai, C., Tao, F., Wang, F., and Yan, M. 2016. Optimization of Well Completion Method and Casing Design Parameters to Delay Casing Impairment Caused by Formation Slippage. Paper SPE-178144-MS presented at the SPE/IADC Middle East Drilling Technology Conference and Exhibition, Abu Dhabi, UAE, 26–28 January.

Ikponmwosa, U., Nwankwo, E., Bello, K., and Olafuyi, A. 2015. Finite Element Analysis of Induced Stresses on Injection Wells using Plane Stress and Strain Elements. Paper SPE-178365-MS presented at the Nigeria Annual International Conference and Exhibition, Lagos, Nigeria, 4–6 August.

Jaeger, J.C. and Cook, N.G.W. 1979. *Fundamentals of Rock Mechanics*. Third Edition. London: Chapman & Hall.

Kaldal, G.S., Jonsson, M.Þ., Palsson, H., and Karlsdottir, S.N. 2013. Collapse Analysis of the Casing in High Temperature Geothermal Wells. Proceedings of the 38th Workshop on Geothermal Reservoir Engineering, Stanford University, Stanford, CA, USA, 11–13 February.

Kaldal, G.S., Jonsson, M.Þ., Palsson, H., and Karlsdottir, S.N. 2015. Structural Analysis of Casings in High Temperature Geothermal Wells in Iceland. Proceedings of the World Geothermal Congress 2015, Melbourne, Australia, 19–25 April.

Kang, B. 2014. Simulation of Casing Stress in Thermal Recovery Production Wells. *Advances in Petroleum Exploration and Development* **7** (1): 38–41.

Kanninen, M.F. and Popelar, C.H. 1985. *Advanced Fracture Mechanics*. New York, NY: Oxford University Press.

Khajeh, M.M., Chalaturnyk, R.J., and Boisvert, J.B. 2012. A Numerical Local Upscaling Approach for Elastic Rock Mechanical Properties: Dealing with Heterogeneity. Paper ARMA-12-654 presented at the 46th US Rock Mechanics.Geomechanics Symposium, Chicago, Illinois, USA, 24–27 June.

Khan, S., Han, H., Ansari, S., Vishteh, M., and Khosravi, N. 2011. Caprock Integrity Analysis in Thermal Operations: An Integrated Geomechanics Approach. Proceedings of the World Heavy Oil Congress, Edmonton, Alberta, Canada, 15–17 March.

King, P.R. 1989. The Use of Normalization for Calculating Effective Permeability. *Transport in Porous Media* **4**: 37–58. doi: 10.1007/BF00134741.

Kirsch, G. 1898. Die Theorie der Elastizität und die Bedürfnisse der Festigkeitslehre. *Zeitschrift des Vereines deutscher Ingenieure* **42**: 797–807.

Ladva, H.K.J., Craster, B., Jones, T.G.J., Goldsmith, G., and Scott, D. 2005. The Cement-to-Formation Interface in Zonal Isolation. *SPE Drilling & Completion* **20** (3): 186–197.

Langenbruch, C. and Shapiro, S.A. 2015. Quantitative Analysis of Rock Stress Heterogeneity: Implications for the Seismogenesis of Fluid-Injection-Induced Seismicity. *Geophysics* **80**: WC73–WC88. doi: 10.1190/geo2015-0061.1.

Lecampion, B. 2012. Hydraulic Fracture Initiation From an Open-Hole: Wellbore Size Pressurization Rate and Fluid-Solid Coupling Effects. Paper ARMA-12-601 presented at the 46th US Rock Mechanics/Geomechanics Symposium, Chicago, Illinois, USA, 24–27 June.

Maharaj, G. 1996. Thermal Well Casing Failure Analysis. Paper SPE-36143-MS presented at the Fourth Latin American and Caribbean Petroleum Engineering Conference, Port-of-Spain, Trinidad, 23–26 April.

Maruyama, K., Tsuru, E., Ogasawara, M., Yasusuke, I. and Peters, E.J. 1990. An Experimental Study of Casing Performance under Thermal Cycling Conditions. *SPE Drilling Engineering* **5** (2): 156–164.

Mokryakov, V. 2011. Analytical Solution for Propagation of Hydraulic Fracture with Barenblatt's Cohesive Tip Zone. *Int. J. Fract.* **169** (2): 159–168.

Nagaso, M., Mikada, H., and Takekawa, J. 2015. The Effects of Fluid Viscosity on the Propagation of Hydraulic Fractures at the Intersection of Pre-Existing Fracture. Paper presented at the 19th International Symposium on Recent Advances in Exploration Geophysics. doi: 10.3997/2352-8265.20140188.

Nikam, A., Awoleke, O.O., and Ahmadi, M. 2016. Modeling the Interaction Between Natural and Hydraulic Fractures Using Three Dimensional Finite Element Analysis. Paper SPE-180364-MS presented at the SPE Western Regional Meeting, Anchorage, Alaska, USA, 23–26 May.

Norris, R.J. and Lewis, J.M. 1991. The Geological Modeling of Effective Permeability in Complex Heterolithic Facies. Paper SPE-22692-MS presented at the 66th Annual Technical Conference and Exhibition, Dallas, Texas, USA, 6–9 October.

Peacock, M.J. 2010. Athabasca Oil Sands: Reservoir Characterization and Its Impact on Thermal and Mining Opportunities. Proceedings of the 7th Petroleum Geology Conference, London, England, 30 March–2 April.

Perkins, T.K. and Kern, L.R. 1961. Widths of Hydraulic Fractures. *J. Pet. Tech.* **13** (9): 937–949. doi: 10.2118/89-PA.

Rho, S., Noynaert, S., Bunger, A.P., Zolfaghari, N., Xing, P., Abell, B., and Suarez-Rivera, R. 2017. Finite-Element Simulations of Hydraulic Fracture Height Growth on Layered Mudstones with Weak Interfaces. Paper ARMA-17-727 presented at the 51st US Rock Mechanics/Geomechanics Symposium, San Francisco, California, USA, 25–28 June.

Rho, S., Suarez-Rivera, R., and Noynaert, S. 2018. Consequences of Rock Layers and Interfaces on Hydraulic Fracturing and Well Production of Unconventional Reservoirs. *Geophysics* (third revision submitted).

Rice, J.R. 1968. A Path Independent Integral and Approximate Analysis of Strain Concentration by Notches and Cracks. *ASME J. Appl. Mech.* **35**: 379–386.

Rice, J.R., and Rosengren, G.F. 1968. Plane Strain Deformation Near a Crack Tip in a Power-Law Hardening Material. *J. Mech. Phys. Solids* **16**: 1–12.

Rodríguez, E., Barrios, W., Sandoval, R., Santos, N., and Cortes, I. 2008. Numerical Simulation for Cyclic Steam Injection at Santa Clara Field. *CT&F-Ciencia, Tecnología y Futuro* **3** (4): 107–128.

Rutledge, J., Yu, X., and Leaney, S. 2015. Microseismic Shearing Driven by Hydraulic-Fracture Opening: An Interpretation of Source-Mechanism Trends. *The Leading Edge* **34** (8): 926–934.

Rutledge, J., Weng, X., Chapman, C., Yu, X., and Leaney, S. 2016, Bedding-Plane Slip as a Microseismic Source During Hydraulic Fracturing. *SEG Technical Program Expanded Abstracts*: 2555-2559. doi: 10.1190/segam2016-13966680.1.

Saripalli, H.K., Salari, H., Saeedi, M., and Hassanzadeh, H. 2018. Analytical Modelling of Cyclic Steam Stimulation (CSS) Process with a Horizontal Well Configuration. *The Canadian Journal of Chemical Engineering* **96** (2): 573–589.

Sarris, E. and Papanastasiou, P. 2011. The Influence of the Cohesive Process Zone in Hydraulic Fracturing Modelling. *Int. J. Fract.* **167**: 33–45.

Sarris, E., and Papanastasiou, P. 2012. Modeling of Hydraulic Fracturing in a Poroelastic Cohesive Formation. *Int. J. Geomech.* **12** (2): 160–167.

Scott, J.D. and Seto, A.C. 1986. Thermal Property Measurements on Oil Sands. *Journal of Canadian Petroleum Technology* **25** (6): 70–77.

Shafiei, A. and Dusseault, M. 2013. Geomechanics of Thermal Viscous Oil Production in Sandstones. *Journal of Petroleum Science and Engineering* **103**: 121–139. doi: 10.1016/j.petrol.2013.02.001.

Shet, C. and Chandra, N. 2002. Analysis of Energy Balance When Using Cohesive Zone Models to Simulate Fracture Processes. *J. Eng. Mater. Technol.* **124**: 440–450.

Sinclair, G.B. 1996. On the Influence of Cohesive Stress-Separation Laws on Elastic Stress Singularities. *J. Elast.* **44**: 203–221.

Snyder, R.E. 1979. Casing Failure Modes in Geothermal Wells. *Geothermal Resources Council Transactions* **3**: 667–670.

Suarez-Rivera, R., Deenadayalu, C., Chertov, M., Hartanto, R., Gathogo, P., and Kunjir, R. 2011. Improving Horizontal Completions on Heterogeneous Tight Shales.

Paper SPE-146998-MS presented at the Canadian Unconventional Resources Conference, Calgary, Alberta, Canada, 15–17 November.

Suarez-Rivera, R., Behrmann, L., Green, S., Burghardt, J., Stanchitz, S., Edelman, E., and Surdi, A. 2013. Defining Three Regions of Hydraulic Fracture Connectivity in Unconventional Reservoirs, Help Designing Completions with Improved Long-Term Productivity. Paper SPE-166505-MS presented at the SPE Annual Technical Conference and Exhibition, New Orleans, Louisiana, USA, 30 September–2 October.

Suarez-Rivera, R., Von Gonten, W.D., Graham, J., Ali, S., Degenhardt, J., and Jegadeesan, A. 2016. Optimizing lateral landing depth for improved well production. Paper URTEC-2460515-MS presented at the Unconventional Resources Technology Conference, San Antonio, Texas, USA, 1–3 August.

Tang, Z.J., Zhou, Y.J., and Jia, J.H. 2013. Technology for Improving Life of Thermal Recovery Well Casing. *Advances in Petroleum Exploration and Development* **5** (1): 71–76.

Torres, A. 2014. Challenges of Casing Design in Geothermal Wells. Paper IADC/SPE-170480-MS presented at the IADC/SPE Asia Pacific Drilling Technology Conference, Bangkok, Thailand, 25–27 August.

Warren, J.E. and Price, H.S. 1961, Flow in Heterogeneous Porous Media. *SPE J.* **2**: 153–169. doi: 10.2118/1579-G.

Wong, R.C.K. and Chau, K.T. 2006. Casing Impairment Induced by Shear Slip Along a Weak Layer in Shale Due to Fluid (Steam) Injection. *Journal of Canadian Petroleum Technology* **45** (12): 60–66.

Wu, J., Gonzalez, M.E., and Hosn, N. 2005. Steam Injection Casing Design. Paper SPE-93833-MS presented at the SPE Western Regional Meeting, Irvine, California, USA, 30 March–1 April.

Wu, J., Knauss, M.E., and Kritzler, T. 2008. Casing Failures in Cyclic Steam Injection Wells. Paper IADC/SPE-114231-MS presented at the IADC/SPE Asia Pacific Drilling Technology Conference and Exhibition, Jakarta, Indonesia, 25–27 August.

Xie, J. 2006. Casing Design and Analysis for Heavy Oil Wells. Paper 2006-415 presented at the World Heavy Oil Conference, Beijing, China, 12–15 November.

Xie, J. and Liu, Y. 2008. Analysis of Casing Deformations in Thermal Wells. Abaqus Users' Conference, Newport, Rhode Island, USA, 19–22 May.

Xie, J. and Tao, G. 2010. Analysis of Casing Connections Subjected to Thermal Cycle Loading. SIMULIA Customer Conference, Providence, Rhode Island, USA, 24–27 May.

Xie, J., Matthews, C., and Desein, T. 2016. Finite Element Analysis for Understanding Oil and Gas Well Deformation Mechanisms. Paper at 2016 Science in the Age of Experience. http://www.3ds.com/events/science-in-the-age-of-experience.

Yao, Y. 2012. Linear Elastic and Cohesive Fracture Analysis to Model Hydraulic Fracture in Brittle and Ductile Rocks. *Rock Mech. Rock Engr.* **45**: 375–387.

Yao, Y., Liu, L., and Keer, L.M. 2015. Pore Pressure Cohesive Zone Modeling of Hydraulic Fracture in Quasi-Brittle Rocks. *Mechanics of Materials* **83**: 17–29.

Yudovich, W., Chin, L.Y., and Morgan, D.R. 1989. Casing Deformation in Ekofisk. *SPE Journal of Petroleum Technology* **41**: 729–734. doi: 10.2118/17856-PA.

Zandi, S., Renard, G., Nauroy, J.F., Guy, N., and Tijani, M. 2010. Numerical Modelling of Geomechanical Effects During Steam Injection in SAGD Heavy Oil Recovery. Paper SPE-129250-MS presented at the SPE EOR Conference at Oil & Gas West Asia, Muscat, Omen, 11–13 April.

Zhang, J. 2013. Borehole Stability Analysis Accounting for Anisotropies in Drilling to Weak Bedding Planes. *International Journal of Rock Mechanics and Mining Sciences* **60**: 160–170. doi: 10.1016/j.ijrmms.2012.12.025.

Zhonglan, T., Lin, S., and Lei, Q. Problems in the Wellbore Integrity of a Shale Gas Horizontal Well and Corresponding Countermeasures. *Natural Gas Industry B* **2**: 522–529. doi: 10.1016/j.ngib.2015.12.006.

Zohdi, T.I. 2015. *A Finite Element Primer for Beginners: The Basics*. SpringerBriefs in Applied Sciences and Technology. New York, NY: Springer.

APPENDIX A

EXCEL-BASED INPUTS FOR MATLAB SCRIPTS SHOWN IN APPENDIX B

A.1 A schematic of the layered rock model

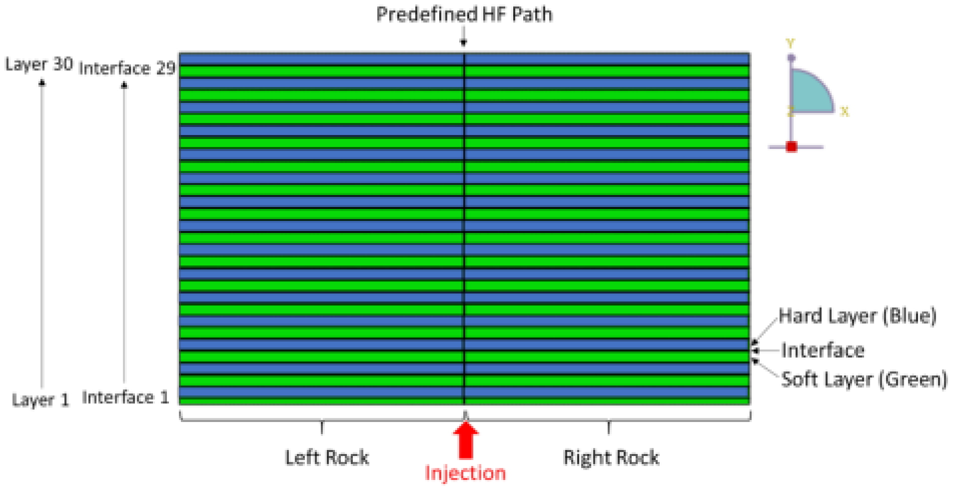

A.2 Inputs for the number of layers, model size, and hydraulic fracture (HF)

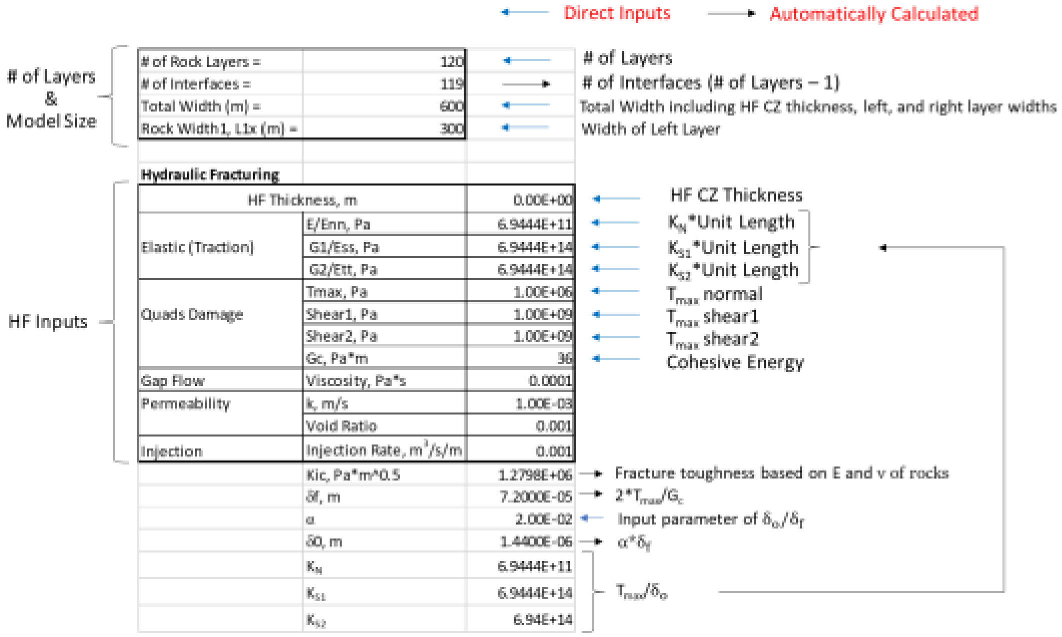

# of Rock Layers =		120	# of Layers
# of Interfaces =		119	# of Interfaces (# of Layers – 1)
Total Width (m) =		600	Total Width including HF CZ thickness, left, and right layer widths
Rock Width1, L1x (m) =		300	Width of Left Layer
Hydraulic Fracturing			
HF Thickness, m		0.00E+00	HF CZ Thickness
Elastic (Traction)	E/Enn, Pa	6.9444E+11	K_N*Unit Length
	G1/Ess, Pa	6.9444E+14	K_{S1}*Unit Length
	G2/Ett, Pa	6.9444E+14	K_{S2}*Unit Length
Quads Damage	Tmax, Pa	1.00E+06	T_{max} normal
	Shear1, Pa	1.00E+09	T_{max} shear1
	Shear2, Pa	1.00E+09	T_{max} shear2
	Gc, Pa*m	36	Cohesive Energy
Gap Flow	Viscosity, Pa*s	0.0001	
Permeability	k, m/s	1.00E-03	
	Void Ratio	0.001	
Injection	Injection Rate, $m^3/s/m$	0.001	
	Kic, Pa*m^0.5	1.2798E+06	Fracture toughness based on E and v of rocks
	δf, m	7.2000E-05	$2*T_{max}/G_c$
	α	2.00E-02	Input parameter of δ_o/δ_f
	δ0, m	1.4400E-06	$\alpha*\delta_f$
	K_N	6.9444E+11	T_{max}/δ_o
	K_{S1}	6.9444E+14	
	K_{S2}	6.94E+14	

A.3 Rock inputs

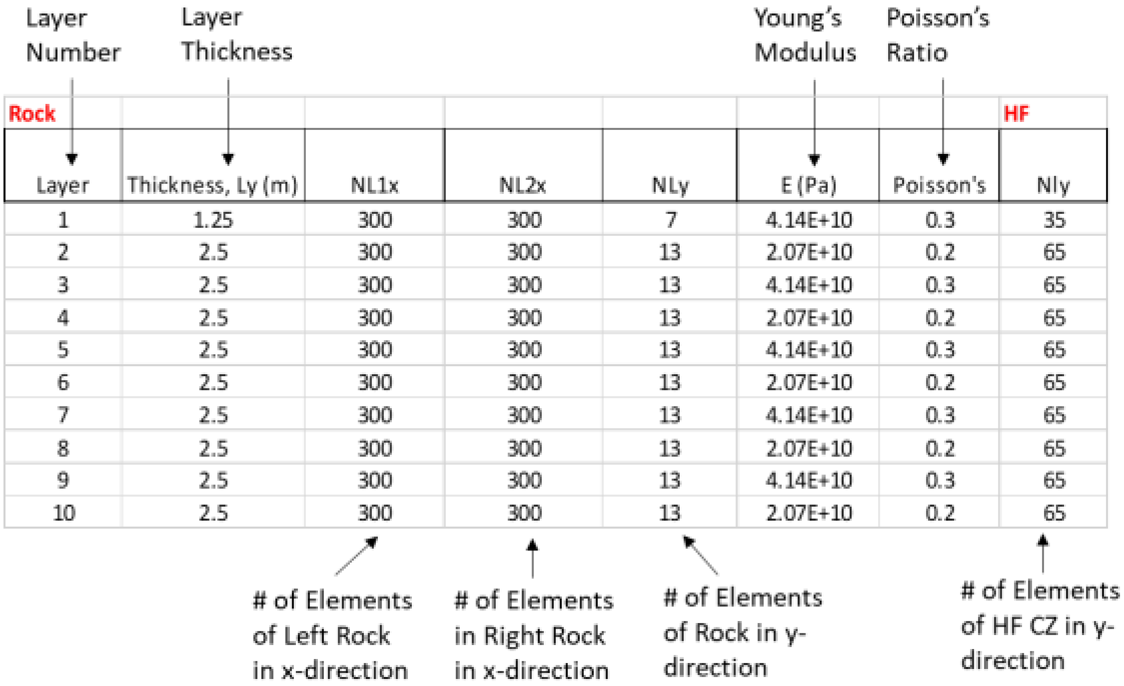

Layer Number

Layer Thickness

Young's Modulus

Poisson's Ratio

Rock							HF
Layer	Thickness, Ly (m)	NL1x	NL2x	NLy	E (Pa)	Poisson's	Nly
1	1.25	300	300	7	4.14E+10	0.3	35
2	2.5	300	300	13	2.07E+10	0.2	65
3	2.5	300	300	13	4.14E+10	0.3	65
4	2.5	300	300	13	2.07E+10	0.2	65
5	2.5	300	300	13	4.14E+10	0.3	65
6	2.5	300	300	13	2.07E+10	0.2	65
7	2.5	300	300	13	4.14E+10	0.3	65
8	2.5	300	300	13	2.07E+10	0.2	65
9	2.5	300	300	13	4.14E+10	0.3	65
10	2.5	300	300	13	2.07E+10	0.2	65

# of Elements of Left Rock in x-direction

# of Elements in Right Rock in x-direction

# of Elements of Rock in y-direction

# of Elements of HF CZ in y-direction

A.4 Interface inputs

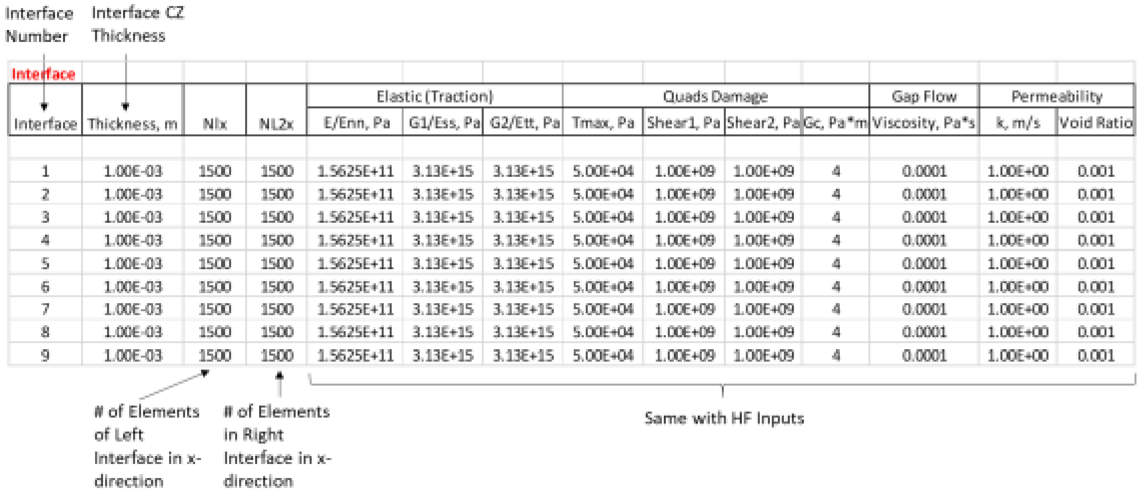

Interface Number

Interface CZ Thickness

Interface				Elastic (Traction)			Quads Damage				Gap Flow	Permeability	
Interface	Thickness, m	NIx	NL2x	E/Enn, Pa	G1/Ess, Pa	G2/Ett, Pa	Tmax, Pa	Shear1, Pa	Shear2, Pa	Gc, Pa*m	Viscosity, Pa*s	k, m/s	Void Ratio
1	1.00E-03	1500	1500	1.5625E+11	3.13E+15	3.13E+15	5.00E+04	1.00E+09	1.00E+09	4	0.0001	1.00E+00	0.001
2	1.00E-03	1500	1500	1.5625E+11	3.13E+15	3.13E+15	5.00E+04	1.00E+09	1.00E+09	4	0.0001	1.00E+00	0.001
3	1.00E-03	1500	1500	1.5625E+11	3.13E+15	3.13E+15	5.00E+04	1.00E+09	1.00E+09	4	0.0001	1.00E+00	0.001
4	1.00E-03	1500	1500	1.5625E+11	3.13E+15	3.13E+15	5.00E+04	1.00E+09	1.00E+09	4	0.0001	1.00E+00	0.001
5	1.00E-03	1500	1500	1.5625E+11	3.13E+15	3.13E+15	5.00E+04	1.00E+09	1.00E+09	4	0.0001	1.00E+00	0.001
6	1.00E-03	1500	1500	1.5625E+11	3.13E+15	3.13E+15	5.00E+04	1.00E+09	1.00E+09	4	0.0001	1.00E+00	0.001
7	1.00E-03	1500	1500	1.5625E+11	3.13E+15	3.13E+15	5.00E+04	1.00E+09	1.00E+09	4	0.0001	1.00E+00	0.001
8	1.00E-03	1500	1500	1.5625E+11	3.13E+15	3.13E+15	5.00E+04	1.00E+09	1.00E+09	4	0.0001	1.00E+00	0.001
9	1.00E-03	1500	1500	1.5625E+11	3.13E+15	3.13E+15	5.00E+04	1.00E+09	1.00E+09	4	0.0001	1.00E+00	0.001

# of Elements of Left Interface in x-direction

# of Elements in Right Interface in x-direction

Same with HF Inputs

APPENDIX B

MATLAB CODE TO PROVIDE AUTOMATIC MESHING FOR HYDARULIC FRACTURE SIMULATION THROUGH MULTI-LAYERED ROCKS, IN ABAQUS

Some functions were intentionally omitted because of the copyright on this code.

```
function main_rho
%% %%%%%%%%%%%%%%%%%%%%%%%  Inputs  %%%%%%%%%%%%%%%%%%%%%%%%%%%%%%%%%%%%%%%
N_layer=xlsread('ABAQUS_Inputs.xlsx','B1:B1');
total_width=xlsread('ABAQUS_Inputs.xlsx','B3:B3');
L1x=xlsread('ABAQUS_Inputs.xlsx','B4:B4');
data_HF=xlsread('ABAQUS_Inputs.xlsx','C7:C18');
layer=xlsread('ABAQUS_Inputs.xlsx',['E8:E',num2str(N_layer+7)]);
data_rock=xlsread('ABAQUS_Inputs.xlsx',['F8:K',num2str(N_layer+7)]);
data_HF_Nly=xlsread('ABAQUS_Inputs.xlsx',['L8:L',num2str(N_layer+7)]);
data_NF=xlsread('ABAQUS_Inputs.xlsx',['O9:AA',num2str(N_layer+7)]);

viscosity_regulization=0.0005;  % Numerical viscosity
Initial_gap_opening=0.0001;     % Initial gap opening in the first or first several
elements of HF CZ

% Far Filed Stresses
TRACTION_TOP=0;  % The value of traction on Boundary at top surface (like pressure, if it
is posetive, it is compression)
TRACTION_BOT=0;   % The value of traction on Boundary at bottom surface
TRACTION_LEFT=0;   % The value of traction on Boundary at left surface
TRACTION_RIGHT=0;   % The value of traction on Boundary at right surface

% Step-1: Geostatic condtions with far field stresses (If no far filed stress is applied,
there is no step-1)
% Step-2: Injection

% Main Boundary Conditions in Step-1 (these boundary conditions are used in Step-2, and
therefore no Step-2 boundary condtion is needed if no far field stress is applied)
top_BC=[0,1,1];      % fisrt:displacement in x-direction, second:displacement in y-
direction, third:moment
bottom_BC=[0,1,1];
left_BC=[1,0,1];
right_BC=[1,0,1];
BCs=[left_BC;right_BC;top_BC;bottom_BC];

% Modified Boundary Conditions in Step-2
New_top_BC=[0,1,1];
New_bottom_BC=[0,1,1];
New_left_BC=[1,0,1];
New_right_BC=[1,0,1];
New_BCs=[New_left_BC;New_right_BC;New_top_BC;New_bottom_BC];

% Total computation time and increment size
total_time=400;
max_pore_pressure_per_increment=10^(10);
initial_increment_size=10^(-5);
```

```
minimum_increment_size= 10^(-10);
maximum_increment_size=total_time/100;
number_attempt_per_increment=8;

%% %%%%%%%%%%%%%%%%%%%%%%%%%%   Rock  %%%%%%%%%%%%%%%%%%%%%%%%%%%%%%%%%%%%%%%
Node=cell(N_layer,2); % create a node cell with N_layer x 2 matrix
Element=cell(N_layer,2); % create a element cell with N_layer x 2 matrix
cumulutive_rock=[0;cumsum(data_rock(1:(end-1),1))];
cumulutive_NF=[0;cumsum(data_NF(1:(end),1))];
o_first_rock=[zeros(N_layer,1),cumulutive_rock+cumulutive_NF]; % coordinates of the first
rock origin
o_second_rock=[(L1x+data_HF(1))*ones(N_layer,1),o_first_rock(:,2)]; % coordinates of the
second rock origin

FN=1; % first node number
FE=1; % first element number
middle_node=zeros(N_layer-1,3);
middle_node(:,1)=FN:(FN+N_layer-2);
FN=FN+N_layer-1;

% create rock nodes and elements
for i=1:N_layer
[node,element,bottom_element,top_element,right_element,left_element,bottom_node,top_node,
right_node,left_node]=rock_rho(o_first_rock(i,:),L1x,data_rock(i,1),data_rock(i,2),data_r
ock(i,4),FN,FE);
    % first total nodes and elements
    Node(i,1)={node};  % create a node cell for the first rock_nodes
    FN=max(node(:,1))+1; % updates of the first node number
    Element(i,1)={element}; % create a element cell for the first rock_elements
    FE=max(element(:,1))+1; % updates of the first element number

    % Node cells for bottom, top, right, and left nodes
    Bottom_node(i,1)={bottom_node};
    Top_node(i,1)={top_node};
    Right_node(i,1)={right_node};
    Left_node(i,1)={left_node};

    % element cells for bottom, top, right, and left elements
    Bottom_element(i,1)={bottom_element};
    Top_element(i,1)={top_element};
    Right_element(i,1)={right_element};
    Left_element(i,1)={left_element};

[node,element,bottom_element,top_element,right_element,left_element,bottom_node,top_node,
right_node,left_node]=rock_rho(o_second_rock(i,:),total_width-L1x-
data_HF(1),data_rock(i,1),data_rock(i,3),data_rock(i,4),FN,FE);
    % second total nodes and elements
    Node(i,2)={node};
    FN=max(node(:,1))+1;
    Element(i,2)={element};
    FE=max(element(:,1))+1;

    Bottom_node(i,2)={bottom_node};
    Top_node(i,2)={top_node};
    Right_node(i,2)={right_node};
    Left_node(i,2)={left_node};

    Bottom_element(i,2)={bottom_element};
    Top_element(i,2)={top_element};
    Right_element(i,2)={right_element};
    Left_element(i,2)={left_element};
end
```

```
%% %%%%%%%%%%%%%%%%%% Natural Fracture %%%%%%%%%%%%%%%%%%%%%%%%%%%%%%%%
cum_rock_for_NFo=cumsum(data_rock(1:(end-1),1));
cum_NF_for_NFo=[0;cumsum(data_NF(1:(end-1),1))];
o_first_NF=[zeros(N_layer-1,1),cum_rock_for_NFo+cum_NF_for_NFo];
o_second_NF=[(L1x+data_HF(1))*ones(N_layer-1,1),o_first_NF(:,2)];


NF_node=cell(N_layer-1,2);
NF_element=cell(N_layer-1,2);
for i=1:(N_layer-1)

[node,element,pore_nodes,top_nodes,bottom_nodes,conecting_pore]=cohesive_rho(o_first_NF(i
,:),data_NF(i,1),L1x,data_NF(i,2),FN,FE,[2;middle_node(i,1)],1);
    NF_node(i,1)={node};
    FN=max(node(:,1))+1;
    NF_element(i,1)={element};
    FE=max(element(:,1))+1;


    NF_Pore_node(i,1)={pore_nodes};
    NF_Bottom_node(i,1)={bottom_nodes};
    NF_Top_node(i,1)={top_nodes};

[node,element,pore_nodes,top_nodes,bottom_nodes,conecting_pore]=cohesive_rho(o_second_NF(
i,:),data_NF(i,1),total_width-L1x-data_HF(1),data_NF(i,3),FN,FE,[1;middle_node(i,1)],1);
    NF_node(i,2)={node};
    FN=max(node(:,1))+1;
    NF_element(i,2)={element};
    FE=max(element(:,1))+1;


    NF_Pore_node(i,2)={pore_nodes};
    NF_Bottom_node(i,2)={bottom_nodes};
    NF_Top_node(i,2)={top_nodes};
end


%% %%%%%%%%%%%%%%%%%%%%%%% Hydraulic Fracture %%%%%%%%%%%%%%%%%%%%%%%%%%%%
HF_node=cell(N_layer,1);
HF_element=cell(N_layer,1);
[node,element,pore_nodes,top_nodes,bottom_nodes,conecting_pore]=cohesive_rho([L1x+data_HF
(1),0],data_HF(1),data_rock(1,1),data_HF_Nly(1,1),FN,FE,[2;middle_node(1,1)],2);
HF_node(1,1)={node};
FN=max(node(:,1))+1;
HF_element(1,1)={element};
FE=max(element(:,1))+1;
injecting_node=pore_nodes(1);


HF_Pore_node(1,1)={pore_nodes'};
HF_Bottom_node(1,1)={bottom_nodes'};
HF_Top_node(1,1)={top_nodes'};


for i=1:(N_layer-2)

[node,element,pore_nodes,top_nodes,bottom_nodes,conecting_pore]=cohesive_rho(o_second_roc
k(i+1,:),data_HF(1),data_rock(i+1,1),data_HF_Nly(i+1,1),FN,FE,[1,
2;middle_node(i,1),middle_node(i+1,1)],2);
    HF_node(i+1,1)={node};
    FN=max(node(:,1))+1;
    HF_element(i+1,1)={element};
    FE=max(element(:,1))+1;


    HF_Pore_node(i+1,1)={pore_nodes'};
    HF_Bottom_node(i+1,1)={bottom_nodes'};
    HF_Top_node(i+1,1)={top_nodes'};
end
```

```
[node,element,pore_nodes,top_nodes,bottom_nodes,conecting_pore]=cohesive_rho([L1x+data_HF
(1),o_second_rock(N_layer,2)],data_HF(1),data_rock(N_layer,1),data_HF_Nly(N_layer,1),FN,F
E,[1;middle_node(N_layer-1,1)],2);
HF_node(N_layer,1)={node};
FN=max(node(:,1))+1;
HF_element(N_layer,1)={element};
FE=max(element(:,1))+1;

HF_Pore_node(N_layer,1)={pore_nodes'};
HF_Bottom_node(N_layer,1)={bottom_nodes'};
HF_Top_node(N_layer,1)={top_nodes'};

middle_node(:,2)=(L1x+data_HF(1)/2)*ones((N_layer-1),1);
middle_node(:,3)=o_first_NF(:,2)+data_NF(:,1)/2;

%% convert cells to a matrix
% total nodes and elements
all_node=[cell2mat(Node(:,1));cell2mat(Node(:,2));cell2mat(NF_node(:,1));cell2mat(NF_node
(:,2));cell2mat(HF_node);middle_node];
rock_element=[cell2mat(Element(:,1));cell2mat(Element(:,2))];

% all rock nodes and elements
rock_bottom_node=[cell2mat(Bottom_node(:,1));cell2mat(Bottom_node(:,2))];
rock_top_node=[cell2mat(Top_node(:,1));cell2mat(Top_node(:,2))];
rock_right_node=[cell2mat(Right_node(:,1));cell2mat(Right_node(:,2))];
rock_left_node=[cell2mat(Left_node(:,1));cell2mat(Left_node(:,2))];

rock_bottom_element=[cell2mat(Bottom_element(:,1));cell2mat(Bottom_element(:,2))];
rock_top_element=[cell2mat(Top_element(:,1));cell2mat(Top_element(:,2))];
rock_right_element=[cell2mat(Right_element(:,1));cell2mat(Right_element(:,2))];
rock_left_element=[cell2mat(Left_element(:,1));cell2mat(Left_element(:,2))];

% all NF_cohesive nodes and elements
NF_pore_node=[cell2mat(NF_Pore_node(:,1));cell2mat(NF_Pore_node(:,2))];
NF_bottom_node=[cell2mat(NF_Bottom_node(:,1));cell2mat(NF_Bottom_node(:,2))];
NF_top_node=[cell2mat(NF_Top_node(:,1));cell2mat(NF_Top_node(:,2))];

NF_elem=[cell2mat(NF_element(:,1));cell2mat(NF_element(:,2))];

% all HF_cohesive nodes and elements
HF_pore_node=cell2mat(HF_Pore_node(:));
HF_bottom_node=cell2mat(HF_Bottom_node(:));
HF_top_node=cell2mat(HF_Top_node(:));

HF_elem=cell2mat(HF_element(:));

%% write 'inp' file %%%%%%%%%%%%%%%%%%%%%%%%%%%%%%%%%%%%%%%%%%%%%%%%%%
tclock=clock;
ff=fopen(['Rho_HF_Non_Welded_',num2str(tclock(1)),'_',num2str(tclock(2)),'_',num2str(tclo
ck(3)),'_',num2str(tclock(4)),'_',num2str(tclock(5)),'.inp'],'w');
fprintf(ff,'*Heading\r\n');
fprintf(ff,'** Job name: abaqus Model name: Model-1\r\n');
fprintf(ff,'*Part, name=Part-1\r\n');
fprintf(ff,'*Node, Nset=all_nodes\r\n');
fprintf(ff,'%7.0f,%13.9g,%13.9g\r\n',all_node');

% rock element
fprintf(ff,'*Element, type=CPE4R, elset=rock_element\r\n');
fprintf(ff,'%7.0f,%13.9g,%13.9g,%13.9g,%13.9g\r\n',rock_element');

% NF cohesive element
```

```
fprintf(ff,'*Element, type=COD2D4P, elset=NF_element\r\n');
fprintf(ff,'%7.0f,%13.9g,%13.9g,%13.9g,%13.9g,%13.9g,%13.9g\r\n',NF_elem');

% HF cohesive element
fprintf(ff,'*Element, type=COD2D4P, elset=HF_element\r\n');
fprintf(ff,'%7.0f,%13.9g,%13.9g,%13.9g,%13.9g,%13.9g,%13.9g\r\n',HF_elem');

% set cohesive element
fprintf(ff,'*Elset, elset=cohesive_element\r\n');
fprintf(ff,'NF_element,HF_element\r\n');

% set specific rock elements
for i=1:N_layer
    rock_bottom_first_node=cell2mat(Bottom_node(i,1));
    rock_bottom_second_node=cell2mat(Bottom_node(i,2));
    rock_top_first_node=cell2mat(Top_node(i,1));
    rock_top_second_node=cell2mat(Top_node(i,2));
    rock_right_first_node=cell2mat(Right_node(i,1));
    rock_right_second_node=cell2mat(Right_node(i,2));
    rock_left_first_node=cell2mat(Left_node(i,1));
    rock_left_second_node=cell2mat(Left_node(i,2));

    rock_first_element=cell2mat(Element(i,1));
    rock_second_element=cell2mat(Element(i,2));
    rock_bottom_first_element=cell2mat(Bottom_element(i,1));
    rock_bottom_second_element=cell2mat(Bottom_element(i,2));
    rock_top_first_element=cell2mat(Top_element(i,1));
    rock_top_second_element=cell2mat(Top_element(i,2));
    rock_right_first_element=cell2mat(Right_element(i,1));
    rock_right_second_element=cell2mat(Right_element(i,2));
    rock_left_first_element=cell2mat(Left_element(i,1));
    rock_left_second_element=cell2mat(Left_element(i,2));

    fprintf(ff,['*Elset, elset=layer_' num2str(layer(i)) '_first_rock_element\r\n']);
    print_node_element_set(ff,rock_first_element(:,1));
    fprintf(ff,['*Elset, elset=layer_' num2str(layer(i)) '_second_rock_element\r\n']);
    print_node_element_set(ff,rock_second_element(:,1));
    fprintf(ff,['*Elset, elset=layer_' num2str(layer(i))
'_first_rock_bottom_element\r\n']);
    print_node_element_set(ff,rock_bottom_first_element);
    fprintf(ff,['*Elset, elset=layer_' num2str(layer(i))
'_second_rock_bottom_element\r\n']);
    print_node_element_set(ff,rock_bottom_second_element);
    fprintf(ff,['*Elset, elset=layer_' num2str(layer(i)) '_first_rock_top_element\r\n']);
    print_node_element_set(ff,rock_top_first_element);
    fprintf(ff,['*Elset, elset=layer_' num2str(layer(i))
'_second_rock_top_element\r\n']);
    print_node_element_set(ff,rock_top_second_element);
    fprintf(ff,['*Elset, elset=layer_' num2str(layer(i))
'_first_rock_right_element\r\n']);
    print_node_element_set(ff,rock_right_first_element);
    fprintf(ff,['*Elset, elset=layer_' num2str(layer(i))
'_second_rock_right_element\r\n']);
    print_node_element_set(ff,rock_right_second_element);
    fprintf(ff,['*Elset, elset=layer_' num2str(layer(i))
'_first_rock_left_element\r\n']);
    print_node_element_set(ff,rock_left_first_element);
    fprintf(ff,['*Elset, elset=layer_' num2str(layer(i))
'_second_rock_left_element\r\n']);
    print_node_element_set(ff,rock_left_second_element);
end

fprintf(ff,'*Elset, elset=rock_bottom_element\r\n');
```

```
fprintf(ff,['layer_' num2str(layer(1)) '_first_rock_bottom_element, layer_'
num2str(layer(1)) '_second_rock_bottom_element\r\n']);
fprintf(ff,'*Elset, elset=rock_top_element\r\n');
fprintf(ff,['layer_' num2str(layer(N_layer)) '_first_rock_top_element, layer_'
num2str(layer(N_layer)) '_second_rock_top_element\r\n']);
fprintf(ff,'*Elset, elset=rock_left_element\r\n');
for i=1:(N_layer-1)
    if rem(i,6)~=0
        fprintf(ff,['layer_' num2str(layer(i)) '_first_rock_left_element, ']);
    else
        fprintf(ff,['layer_' num2str(layer(i)) '_first_rock_left_element\r\n']);
    end
end
fprintf(ff,['layer_' num2str(layer(N_layer)) '_first_rock_left_element\r\n']);
fprintf(ff,'*Elset, elset=rock_right_element\r\n');
for i=1:(N_layer-1)
    if rem(i,6)~=0
        fprintf(ff,['layer_' num2str(layer(i)) '_second_rock_right_element, ']);
    else
        fprintf(ff,['layer_' num2str(layer(i)) '_second_rock_right_element\r\n']);
    end
end
fprintf(ff,['layer_' num2str(layer(N_layer)) '_second_rock_right_element\r\n']);


fprintf(ff,'*Elset, elset=rock_second_left_element\r\n');
for i=1:(N_layer-1)
    if rem(i,6)~=0
        fprintf(ff,['layer_' num2str(layer(i)) '_second_rock_left_element, ']);
    else
        fprintf(ff,['layer_' num2str(layer(i)) '_second_rock_left_element\r\n']);
    end
end
fprintf(ff,['layer_' num2str(layer(N_layer)) '_second_rock_left_element\r\n']);
fprintf(ff,'*Elset, elset=rock_first_right_element\r\n');
for i=1:(N_layer-1)
    if rem(i,6)~=0
        fprintf(ff,['layer_' num2str(layer(i)) '_first_rock_right_element, ']);
    else
        fprintf(ff,['layer_' num2str(layer(i)) '_first_rock_right_element\r\n']);
    end
end
fprintf(ff,['layer_' num2str(layer(N_layer)) '_first_rock_right_element\r\n']);


%left,right,top,bottom
% Define sets for BC's:
if max(BCs(1,:))~=0
    fprintf(ff,'*Nset, nset=rock_left_nodes\r\n');
    print_node_element_set(ff,cell2mat(Left_node(:,1)));
end
if max(BCs(2,:))~=0
    fprintf(ff,'*Nset, nset=rock_right_nodes\r\n');
    print_node_element_set(ff,cell2mat(Right_node(:,2)));
end
if max(BCs(3,:))~=0
    fprintf(ff,'*Nset, nset=rock_top_nodes\r\n');
    print_node_element_set(ff,[cell2mat(Top_node(end,1));cell2mat(Top_node(end,2))]);
end
if max(BCs(4,:))~=0
    fprintf(ff,'*Nset, nset=rock_bottom_nodes\r\n');
    print_node_element_set(ff,[cell2mat(Bottom_node(1,1));cell2mat(Bottom_node(1,2))]);
end


% Define Rock surfaces
for i=1:N_layer
    fprintf(ff,['*Surface, type=element, name=layer_' num2str(layer(i))
'_first_rock_bottom_surface\r\n']);
```

```
    fprintf(ff,['layer_' num2str(layer(i)) '_first_rock_bottom_element,S1\r\n']);
    fprintf(ff,['*Surface, type=element, name=layer_' num2str(layer(i))
'_second_rock_bottom_surface\r\n']);
    fprintf(ff,['layer_' num2str(layer(i)) '_second_rock_bottom_element,S1\r\n']);
    fprintf(ff,['*Surface, type=element, name=layer_' num2str(layer(i))
'_first_rock_top_surface\r\n']);
    fprintf(ff,['layer_' num2str(layer(i)) '_first_rock_top_element,S3\r\n']);
    fprintf(ff,['*Surface, type=element, name=layer_' num2str(layer(i))
'_second_rock_top_surface\r\n']);
    fprintf(ff,['layer_' num2str(layer(i)) '_second_rock_top_element,S3\r\n']);
    fprintf(ff,['*Surface, type=element, name=layer_' num2str(layer(i))
'_first_rock_right_surface\r\n']);
    fprintf(ff,['layer_' num2str(layer(i)) '_first_rock_right_element,S2\r\n']);
    fprintf(ff,['*Surface, type=element, name=layer_' num2str(layer(i))
'_second_rock_right_surface\r\n']);
    fprintf(ff,['layer_' num2str(layer(i)) '_second_rock_right_element,S2\r\n']);
    fprintf(ff,['*Surface, type=element, name=layer_' num2str(layer(i))
'_first_rock_left_surface\r\n']);
    fprintf(ff,['layer_' num2str(layer(i)) '_first_rock_left_element,S4\r\n']);
    fprintf(ff,['*Surface, type=element, name=layer_' num2str(layer(i))
'_second_rock_left_surface\r\n']);
    fprintf(ff,['layer_' num2str(layer(i)) '_second_rock_left_element,S4\r\n']);
end


fprintf(ff,'*Surface, type=element, name=rock_bottom_surface\r\n');
fprintf(ff,'rock_bottom_element, S1\r\n');
fprintf(ff,'*Surface, type=element, name=rock_top_surface\r\n');
fprintf(ff,'rock_top_element, S3\r\n');
fprintf(ff,'*Surface, type=element, name=rock_left_surface\r\n');
fprintf(ff,'rock_left_element, S4\r\n');
fprintf(ff,'*Surface, type=element, name=rock_right_surface\r\n');
fprintf(ff,'rock_right_element, S2\r\n');


% set NF_cohesive nodes and elements
for i=1:N_layer-1
    NF_pore_first_node=cell2mat(NF_Pore_node(i,1));
    NF_pore_second_node=cell2mat(NF_Pore_node(i,2));
    NF_bottom_first_node=cell2mat(NF_Bottom_node(i,1));
    NF_bottom_second_node=cell2mat(NF_Bottom_node(i,2));
    NF_top_first_node=cell2mat(NF_Top_node(i,1));
    NF_top_second_node=cell2mat(NF_Top_node(i,2));


    NF_first_element=cell2mat(NF_element(i,1));
    NF_second_element=cell2mat(NF_element(i,2));


    fprintf(ff,['*Nset, nset=layer_' num2str(layer(i)) '_first_NF_pore_node\r\n']);
    print_node_element_set(ff,NF_pore_first_node);
    fprintf(ff,['*Nset, nset=layer_' num2str(layer(i)) '_second_NF_pore_node\r\n']);
    print_node_element_set(ff,NF_pore_second_node);
    fprintf(ff,['*Elset, elset=layer_' num2str(layer(i)) '_first_NF_element\r\n']);
    print_node_element_set(ff,NF_first_element(:,1));
    fprintf(ff,['*Elset, elset=layer_' num2str(layer(i)) '_second_NF_element\r\n']);
    print_node_element_set(ff,NF_second_element(:,1));
end


% Set NF elements at each layer
for i=1:(N_layer-1)
fprintf(ff,['*Elset, elset=layer_' num2str(layer(i)) '_NF_element\r\n']);
fprintf(ff,['layer_' num2str(layer(i)) '_first_NF_element, layer_'  num2str(layer(i))
'_second_NF_element\r\n']);
end


% Define NF surfaces
for i=1:N_layer-1
```

```
    fprintf(ff,['*Surface, type=element, name=layer_' num2str(layer(i))
'_first_NF_bottom_surface\r\n']);
    fprintf(ff,['layer_' num2str(layer(i)) '_first_NF_element,S1\r\n']);
    fprintf(ff,['*Surface, type=element, name=layer_' num2str(layer(i))
'_second_NF_bottom_surface\r\n']);
    fprintf(ff,['layer_' num2str(layer(i)) '_second_NF_element,S1\r\n']);
    fprintf(ff,['*Surface, type=element, name=layer_' num2str(layer(i))
'_first_NF_top_surface\r\n']);
    fprintf(ff,['layer_' num2str(layer(i)) '_first_NF_element,S3\r\n']);
    fprintf(ff,['*Surface, type=element, name=layer_' num2str(layer(i))
'_second_NF_top_surface\r\n']);
    fprintf(ff,['layer_' num2str(layer(i)) '_second_NF_element,S3\r\n']);
end

% set HF_cohesive nodes and elements
for i=1:N_layer
    HF_pore_node=cell2mat(HF_Pore_node(i));
    HF_bottom_node=cell2mat(HF_Bottom_node(i));
    HF_top_node=cell2mat(HF_Top_node(i));

    HF_elem=cell2mat(HF_element(i));

    fprintf(ff,['*Nset, nset=layer_' num2str(layer(i)) '_HF_pore_node\r\n']);
    print_node_element_set(ff,HF_pore_node);
    fprintf(ff,['*Elset, elset=layer_' num2str(layer(i)) '_HF_element\r\n']);
    print_node_element_set(ff,HF_elem(:,1));
end

% HF pore nodes
fprintf(ff,'*Nset, nset=HF_pore_node\r\n');
for i=1:(N_layer-1)
    if rem(i,6)~=0
        fprintf(ff,['layer_' num2str(layer(i)) '_HF_pore_node, ']);
    else
        fprintf(ff,['layer_' num2str(layer(i)) '_HF_pore_node\r\n ']);
    end
end
fprintf(ff,['layer_' num2str(layer(N_layer)) '_HF_pore_node\r\n']);

% all pore nodes
fprintf(ff,'*Nset, nset=pore_node\r\n');
for i=1:(N_layer-1)
    if rem(i,4)~=0
        fprintf(ff,['layer_' num2str(layer(i)) '_first_NF_pore_node, ']);
        fprintf(ff,['layer_' num2str(layer(i)) '_second_NF_pore_node, ']);
    else
        fprintf(ff,['layer_' num2str(layer(i)) '_first_NF_pore_node, ']);
        fprintf(ff,['layer_' num2str(layer(i)) '_second_NF_pore_node\r\n ']);
    end
end
tii=i+1;
for i=1:(N_layer-1)
    if rem(tii,7)~=0
        fprintf(ff,['layer_' num2str(layer(i)) '_HF_pore_node, ']);
    else
        fprintf(ff,['layer_' num2str(layer(i)) '_HF_pore_node\r\n ']);
    end
    tii=tii+1;
end
fprintf(ff,['layer_' num2str(layer(N_layer)) '_HF_pore_node\r\n']);

% injection node
fprintf(ff,'*Nset, nset=injection_node\r\n');
fprintf(ff,'%7.0f\r\n',injecting_node);
```

```
HF_opening=HF_element{1,1};
% elements for initial opening
fprintf(ff,'*Elset, elset=open_element\r\n');
fprintf(ff,'%7.0f\r\n',HF_opening(1,1));

% Define HF surfaces
for i=1:N_layer
    fprintf(ff,['*Surface, type=element, name=layer_' num2str(layer(i))
'_HF_bottom_surface\r\n']);
    fprintf(ff,['layer_' num2str(layer(i)) '_HF_element,S1\r\n']);
    fprintf(ff,['*Surface, type=element, name=layer_' num2str(layer(i))
'_HF_top_surface\r\n']);
    fprintf(ff,['layer_' num2str(layer(i)) '_HF_element,S3\r\n']);
end

% section: HF_cohesive
fprintf(ff,'** Section: HF_cohesive\r\n');
fprintf(ff,'*Cohesive Section, elset=HF_element, controls=EC-1, material=HF_cohesive,
response=TRACTION SEPARATION\r\n');
fprintf(ff,',\r\n');

% section: NF_cohesive
for i=1:(N_layer-1)
    fprintf(ff,['** Section: NF_cohesive_layer_' num2str(layer(i)) '\r\n']);
    fprintf(ff,['*Cohesive Section, elset=layer_' num2str(layer(i)) '_first_NF_element,
controls=EC-1, material=NF_cohesive_' num2str(layer(i)) ', response=TRACTION
SEPARATION\r\n']);
    fprintf(ff,',\r\n');

    fprintf(ff,['*Cohesive Section, elset=layer_' num2str(layer(i)) '_second_NF_element,
controls=EC-1, material=NF_cohesive_' num2str(layer(i)) ', response=TRACTION
SEPARATION\r\n']);
    fprintf(ff,',\r\n');
end

% section: rock
for i=1:N_layer
    fprintf(ff,['** Section: rock_layer_' num2str(layer(i)) '\r\n']);
    fprintf(ff,['*Solid Section, elset=layer_' num2str(layer(i)) '_first_rock_element,
material=Rock_' num2str(layer(i)) '\r\n']);
    fprintf(ff,'1.,\r\n');
    fprintf(ff,['*Solid Section, elset=layer_' num2str(layer(i)) '_second_rock_element,
material=Rock_' num2str(layer(i)) '\r\n']);
    fprintf(ff,'1.,\r\n');
end
fprintf(ff,'*End Part\r\n');

%% Assembly
fprintf(ff,'**\r\n');
fprintf(ff,'** Assembly\r\n');
fprintf(ff,'**\r\n');
fprintf(ff,'*Assembly, name=Assembly\r\n');
fprintf(ff,'*Instance, name=Part-1-1, part=Part-1\r\n');
fprintf(ff,'*End Instance\r\n');

% Constraints
for i=1:(N_layer-1)
    fprintf(ff,'** Constraint:\r\n');
    fprintf(ff,['*Tie, name=Constraint-first_BT_' num2str(layer(i)) ', adjust=yes\r\n']);
    fprintf(ff,['PART-1-1.layer_' num2str(layer(i)) '_first_NF_bottom_surface, PART-1-
1.layer_' num2str(layer(i)) '_first_rock_top_surface\r\n']);
```

```
    fprintf(ff,['*Tie, name=Constraint-second_BT_' num2str(layer(i)) ',
adjust=yes\r\n']);
    fprintf(ff,['PART-1-1.layer_' num2str(layer(i)) '_second_NF_bottom_surface,PART-1-
1.layer_' num2str(layer(i)) '_second_rock_top_surface\r\n']);

    fprintf(ff,['*Tie, name=Constraint-first_TB_' num2str(layer(i)) ', adjust=yes\r\n']);
    fprintf(ff,['PART-1-1.layer_' num2str(layer(i)) '_first_NF_top_surface, PART-1-
1.layer_' num2str(layer(i+1)) '_first_rock_bottom_surface\r\n']);
    fprintf(ff,['*Tie, name=Constraint-second_TB_' num2str(layer(i)) ',
adjust=yes\r\n']);
    fprintf(ff,['PART-1-1.layer_' num2str(layer(i)) '_second_NF_top_surface, PART-1-
1.layer_' num2str(layer(i+1)) '_second_rock_bottom_surface\r\n']);
end

for i=1:N_layer
    fprintf(ff,['*Tie, name=Constraint-first_LR_' num2str(layer(i)) ', adjust=yes\r\n']);
    fprintf(ff,['PART-1-1.layer_' num2str(layer(i)) '_HF_top_surface, PART-1-1.layer_'
num2str(layer(i)) '_first_rock_right_surface\r\n']);
    fprintf(ff,['*Tie, name=Constraint-first_RL_' num2str(layer(i)) ', adjust=yes\r\n']);
    fprintf(ff,['PART-1-1.layer_' num2str(layer(i)) '_HF_bottom_surface, PART-1-1.layer_'
num2str(layer(i)) '_second_rock_left_surface\r\n']);
end
fprintf(ff,'*End Assembly\r\n');

%% Controls
fprintf(ff,'**\r\n');
fprintf(ff,'** ELEMENT CONTROLS\r\n');
fprintf(ff,'**\r\n');
fprintf(ff,['*Section Controls, name=EC-1, ELEMENT DELETION=NO, VISCOSITY='
num2str(viscosity_regulization),',INITIAL GAP
OPENING=',num2str(Initial_gap_opening),'\r\n']);
fprintf(ff,'1., 1., 1.\r\n');

%% Materials
% HF_cohesive material
fprintf(ff,'**\r\n');
fprintf(ff,'** MATERIALS\r\n');
fprintf(ff,'**\r\n');
fprintf(ff,'*Material, name=HF_cohesive\r\n');
fprintf(ff,'*Damage Initiation, criterion=QUADS\r\n');
fprintf(ff,[num2str(data_HF(5)) ',' num2str(data_HF(6)) ',' num2str(data_HF(7)) '\r\n']);
fprintf(ff,'*Damage Evolution, type=ENERGY, SOFTENING=LINEAR\r\n');
fprintf(ff,[num2str(data_HF(8)) '\r\n']);
fprintf(ff,'*Elastic, type=TRACTION\r\n');
fprintf(ff, [num2str(data_HF(2)) ',' num2str(data_HF(3)) ',' num2str(data_HF(4))
'\r\n']);
fprintf(ff,'*Gap Flow\r\n');
fprintf(ff, [num2str(data_HF(9)) '\r\n']);
fprintf(ff,'*Permeability, specific=9800.\r\n');
fprintf(ff,[num2str(data_HF(10)) ',' num2str(data_HF(11)) '\r\n']);

% NF_cohesive materials
for i=1:(N_layer-1)
    fprintf(ff,['*Material, name=NF_cohesive_' num2str(layer(i)) '\r\n']);
    fprintf(ff,'*Damage Initiation, criterion=QUADS\r\n');
    fprintf(ff,[num2str(data_NF(i,7)) ',' num2str(data_NF(i,8)) ',' num2str(data_NF(i,9))
'\r\n']);
    fprintf(ff,'*Damage Evolution, type=ENERGY, SOFTENING=LINEAR\r\n');
    fprintf(ff,[num2str(data_NF(i,10)) '\r\n']);
    fprintf(ff,'*Elastic, type=TRACTION\r\n');
    fprintf(ff, [num2str(data_NF(i,4)) ',' num2str(data_NF(i,5)) ','
num2str(data_NF(i,6)) '\r\n']);
    fprintf(ff,'*Gap Flow\r\n');
    fprintf(ff, [num2str(data_NF(i,11)) '\r\n']);
    fprintf(ff,'*Permeability, specific=9800.\r\n');
```

```
    fprintf(ff,[num2str(data_NF(i,12)) ',' num2str(data_NF(i,13)) '\r\n']);
end

% rock materials
for i=1:N_layer
fprintf(ff,['*Material, name=Rock_' num2str(layer(i)) '\r\n']);
fprintf(ff,'*Elastic\r\n');
fprintf(ff, [num2str(data_rock(i,5)) ',' num2str(data_rock(i,6)) '\r\n']);
end

fprintf(ff,'*Initial Conditions, Type=Initial Gap\r\n');
fprintf(ff,'PART-1-1.open_element\r\n');

%% STep-1
fprintf(ff,'**\r\n');
fprintf(ff,'** STEP: Step-1\r\n');
fprintf(ff,'*Step, name=Step-1, nlgeom=YES, unsymm=YES\r\n');
fprintf(ff,'*Geostatic\r\n');

% Load
if TRACTION_TOP~=0 || TRACTION_BOT~=0 || TRACTION_RIGHT~=0 || TRACTION_LEFT~=0
    fprintf(ff,'**\r\n');
    fprintf(ff,'** LOADS\r\n');
    name_load=0;
end
if TRACTION_TOP~=0
    name_load=name_load+1;
    fprintf(ff,'**\r\n');
    fprintf(ff,['** Name: Load-',num2str(name_load),'   Type: Pressure  Top B.C.\r\n']);
    fprintf(ff,'*Dsload\r\n');
    fprintf(ff,['PART-1-1.rock_top_surface, P, ',num2str(TRACTION_TOP), '\r\n']);
end
if TRACTION_BOT~=0
    name_load=name_load+1;
    fprintf(ff,'** ');
    fprintf(ff,['** Name: Load-',num2str(name_load),'   Type: Pressure  Bottom
B.C.\r\n']);
    fprintf(ff,'*Dsload\r\n');
    fprintf(ff,['PART-1-1.rock_bottom_surface, P, ',num2str(TRACTION_BOT), '\r\n']);
end
if TRACTION_RIGHT~=0
    name_load=name_load+1;
    fprintf(ff,'**\r\n');
    fprintf(ff,['** Name: Load-',num2str(name_load),'   Type: Pressure  Right
B.C.\r\n']);
    fprintf(ff,'*Dsload\r\n');
    fprintf(ff,['PART-1-1.rock_right_surface, P, ',num2str(TRACTION_RIGHT), '\r\n']);
end
if TRACTION_LEFT~=0
    name_load=name_load+1;
    fprintf(ff,'** ');
    fprintf(ff,['** Name: Load-',num2str(name_load),'   Type: Pressure  Left B.C.\r\n']);
    fprintf(ff,'*Dsload\r\n');
    fprintf(ff,['PART-1-1.rock_left_surface, P,',num2str(TRACTION_LEFT), '\r\n']);
end

% Boundary Condition
fprintf(ff,'**\r\n');
if TRACTION_TOP~=0 || TRACTION_BOT~=0 || TRACTION_RIGHT~=0 || TRACTION_LEFT~=0
fprintf(ff,'** BOUNDARY CONDITIONS\r\n');
fprintf(ff,'**\r\n');
fprintf(ff,'*Boundary\r\n');
if max(BCs(1,:))~=0
    if BCs(1,1)==1
        fprintf(ff,'PART-1-1.rock_left_nodes, 1,1\r\n');
```

```
    end
    if BCs(1,2)==1
        fprintf(ff,'PART-1-1.rock_left_nodes, 2,2\r\n');
    end
    if BCs(1,3)==1
        fprintf(ff,'PART-1-1.rock_left_nodes, 6,6\r\n');
    end
end
if max(BCs(2,:))~=0
    if BCs(2,1)==1
        fprintf(ff,'PART-1-1.rock_right_nodes, 1,1\r\n');
    end
    if BCs(2,2)==1
        fprintf(ff,'PART-1-1.rock_right_nodes, 2,2\r\n');
    end
    if BCs(2,3)==1
        fprintf(ff,'PART-1-1.rock_right_nodes, 6,6\r\n');
    end
end
if max(BCs(3,:))~=0
    if BCs(3,1)==1
        fprintf(ff,'PART-1-1.rock_top_nodes, 1,1\r\n');
    end
    if BCs(3,2)==1
        fprintf(ff,'PART-1-1.rock_top_nodes, 2,2\r\n');
    end
    if BCs(3,3)==1
        fprintf(ff,'PART-1-1.rock_top_nodes, 6,6\r\n');
    end
end
if max(BCs(4,:))~=0
    if BCs(4,1)==1
        fprintf(ff,'PART-1-1.rock_bottom_nodes, 1,1\r\n');
    end
    if BCs(4,2)==1
        fprintf(ff,'PART-1-1.rock_bottom_nodes, 2,2\r\n');
    end
    if BCs(4,3)==1
        fprintf(ff,'PART-1-1.rock_bottom_nodes, 6,6\r\n');
    end
end
end

% Outputs
fprintf(ff,'**\r\n');
fprintf(ff,'** OUTPUT REQUESTS\r\n');
fprintf(ff,'**\r\n');
fprintf(ff,'*Restart, write, frequency=1, overlay\r\n');
fprintf(ff,'**\r\n');
fprintf(ff,'** FIELD OUTPUT: F-Output-1\r\n');
fprintf(ff,'**\r\n');
fprintf(ff,'*Output, field\r\n');
fprintf(ff,'*Node Output\r\n');
fprintf(ff,'POR,U\r\n');
fprintf(ff,'*element Output, ELSET=PART-1-1.rock_element\r\n');
fprintf(ff,'S,LE,PE\r\n');
fprintf(ff,'*element Output, ELSET=PART-1-1.cohesive_element\r\n');
fprintf(ff,'LE, GFVR, SDEG, DMICRT, PFOPEN\r\n');


fprintf(ff,'**\r\n');
fprintf(ff,'** HISTORY OUTPUT: H-Output-1\r\n');
fprintf(ff,'**\r\n');
fprintf(ff,'*Output, history, variable=PRESELECT\r\n');
fprintf(ff,'*End Step\r\n');
```

```
%% Step-2
fprintf(ff,'**\r\n');
fprintf(ff,'** STEP: Step-2\r\n');
fprintf(ff,'*Step, name=Step-2, nlgeom=YES, inc=100000000, unsymm=YES\r\n');
fprintf(ff,['*Soils, consolidation, end=PERIOD, utol='
num2str(max_pore_pressure_per_increment) ', STABILIZE\r\n']);
fprintf(ff,[num2str(initial_increment_size) ' , ' num2str(total_time) ' , '
num2str(minimum_increment_size) ' , ' num2str(maximum_increment_size) ',\r\n']);
fprintf(ff,'*CONTROLS, PARAMETERS=TIME INCREMENTATION\r\n');
fprintf(ff,['8,10,,,,,,' num2str(number_attempt_per_increment) ',,,,,\r\n']);
fprintf(ff,'0.25,,,,0.1,0.125,,\r\n');


if TRACTION_TOP~=0 || TRACTION_BOT~=0 || TRACTION_RIGHT~=0 || TRACTION_LEFT~=0
       fprintf(ff,'**\r\n');
       fprintf(ff,'** BOUNDARY CONDITIONS\r\n');
       fprintf(ff,'**\r\n');
       fprintf(ff,'*Boundary, op=New\r\n');
    if max(New_BCs(1,:))~=0
      if New_BCs(1,1)==1
        fprintf(ff,'PART-1-1.rock_left_nodes, 1,1\r\n');
      end
      if New_BCs(1,2)==1
        fprintf(ff,'PART-1-1.rock_left_nodes, 2,2\r\n');
      end
      if New_BCs(1,3)==1
        fprintf(ff,'PART-1-1.rock_left_nodes, 6,6\r\n');
      end
    end
    if max(New_BCs(2,:))~=0
      if New_BCs(2,1)==1
        fprintf(ff,'PART-1-1.rock_right_nodes, 1,1\r\n');
      end
      if New_BCs(2,2)==1
        fprintf(ff,'PART-1-1.rock_right_nodes, 2,2\r\n');
      end
      if New_BCs(2,3)==1
        fprintf(ff,'PART-1-1.rock_right_nodes, 6,6\r\n');
      end
    end
    if max(New_BCs(3,:))~=0
      if New_BCs(3,1)==1
        fprintf(ff,'PART-1-1.rock_top_nodes, 1,1\r\n');
      end
      if New_BCs(3,2)==1
        fprintf(ff,'PART-1-1.rock_top_nodes, 2,2\r\n');
      end
      if New_BCs(3,3)==1
        fprintf(ff,'PART-1-1.rock_top_nodes, 6,6\r\n');
      end
    end
    if max(New_BCs(4,:))~=0
      if New_BCs(4,1)==1
        fprintf(ff,'PART-1-1.rock_bottom_nodes, 1,1\r\n');
      end
      if New_BCs(4,2)==1
        fprintf(ff,'PART-1-1.rock_bottom_nodes, 2,2\r\n');
      end
      if New_BCs(4,3)==1
        fprintf(ff,'PART-1-1.rock_bottom_nodes, 6,6\r\n');
      end
    end
else
fprintf(ff,'**\r\n');
fprintf(ff,'** BOUNDARY CONDITIONS\r\n');
fprintf(ff,'**\r\n');
fprintf(ff,'*Boundary\r\n');
if max(BCs(1,:))~=0
```

```
    if BCs(1,1)==1
        fprintf(ff,'PART-1-1.rock_left_nodes, 1,1\r\n');
    end
    if BCs(1,2)==1
        fprintf(ff,'PART-1-1.rock_left_nodes, 2,2\r\n');
    end
    if BCs(1,3)==1
        fprintf(ff,'PART-1-1.rock_left_nodes, 6,6\r\n');
    end
end
if max(BCs(2,:))~=0
    if BCs(2,1)==1
        fprintf(ff,'PART-1-1.rock_right_nodes, 1,1\r\n');
    end
    if BCs(2,2)==1
        fprintf(ff,'PART-1-1.rock_right_nodes, 2,2\r\n');
    end
    if BCs(2,3)==1
        fprintf(ff,'PART-1-1.rock_right_nodes, 6,6\r\n');
    end
end
if max(BCs(3,:))~=0
    if BCs(3,1)==1
        fprintf(ff,'PART-1-1.rock_top_nodes, 1,1\r\n');
    end
    if BCs(3,2)==1
        fprintf(ff,'PART-1-1.rock_top_nodes, 2,2\r\n');
    end
    if BCs(3,3)==1
        fprintf(ff,'PART-1-1.rock_top_nodes, 6,6\r\n');
    end
end
if max(BCs(4,:))~=0
    if BCs(4,1)==1
        fprintf(ff,'PART-1-1.rock_bottom_nodes, 1,1\r\n');
    end
    if BCs(4,2)==1
        fprintf(ff,'PART-1-1.rock_bottom_nodes, 2,2\r\n');
    end
    if BCs(4,3)==1
        fprintf(ff,'PART-1-1.rock_bottom_nodes, 6,6\r\n');
    end
end
end


% Loads
fprintf(ff,'**\r\n');
fprintf(ff,'** LOADS\r\n');
fprintf(ff,'**\r\n');
fprintf(ff,'** Name: Load-1   Type: Concentrated pore fluid\r\n');
fprintf(ff,'*Cflow\r\n');
fprintf(ff, ['Part-1-1.injection_node, ,-' num2str(data_HF(12)) '\r\n']);

% Outputs
fprintf(ff,'**\r\n');
fprintf(ff,'** OUTPUT REQUESTS\r\n');
fprintf(ff,'**\r\n');
fprintf(ff,'*Restart, write, frequency=1, overlay\r\n');
fprintf(ff,'**\r\n');
fprintf(ff,'** FIELD OUTPUT: F-Output-1\r\n');
fprintf(ff,'**\r\n');
fprintf(ff,'*Output, field\r\n');
fprintf(ff,'*Node Output\r\n');
fprintf(ff,'POR,U\r\n');
fprintf(ff,'*element Output, ELSET=PART-1-1.rock_element\r\n');
fprintf(ff,'S,LE,PE\r\n');
```

```
fprintf(ff,'*element Output, ELSET=PART-1-1.cohesive_element\r\n');
fprintf(ff,'LE, GFVR, SDEG, DMICRT, PFOPEN\r\n');

fprintf(ff,'**\r\n');
fprintf(ff,'** HISTORY OUTPUT: H-Output-1\r\n');
fprintf(ff,'**\r\n');
fprintf(ff,'*Output, history, variable=PRESELECT\r\n');
fprintf(ff,'*node output,nset=PART-1-1.injection_node\r\n');
fprintf(ff,'por\r\n');

fprintf(ff,'*EL PRINT, ELSET=PART-1-1.cohesive_element\r\n');
fprintf(ff,'GFVR, DMICRT , SDEG, PFOPEN\r\n');
fprintf(ff,'*End Step\r\n');
```